Supporting Information

A Peierls transition in long polymethine molecular wires: evolution of molecular geometry and single-molecule conductance

Wenjun Xu,[1,7] Edmund Leary,[2,7]* Sara Sangtarash,[3] Michael Jirasek,[1] M. Teresa González,[2] Kirsten E. Christensen,[1] Lydia Abellán Vicente,[2] Nicolás Agraït,[2,4] Simon J. Higgins,[5] Richard J. Nichols,[5] Colin J. Lambert[6] and Harry L. Anderson[1]*

1. University of Oxford, Department of Chemistry, Chemistry Research Laboratory, Oxford OX1 3TA, UK
2. Fundación IMDEA Nanociencia, Calle Faraday 9, Campus Universitario de Cantoblanco, 28049 Madrid, Spain.
3. School of Engineering, University of Warwick, Coventry CV4 7AL, UK.
4. Departamento de Física de la Materia Condensada, IFIMAC and Instituto "Nicolás Cabrera", Universidad Autónoma de Madrid, 28049 Madrid, Spain.
5. Department of Chemistry, Donnan and Robert Robinson Laboratories, University of Liverpool, Liverpool L69 7ZD, UK.
6. Department of Physics, Lancaster University, Lancaster LA1 4YW, UK.
7. These authors contributed equally: Wenjun Xu, Edmund Leary.

*Correspondence to: edmund.leary@imdea.org or harry.anderson@chem.ox.ac.uk.

Table of Contents

Section 1.1. General Synthetic Experimental Methods

All manipulations of air- or water-sensitive compounds were performed using standard high-vacuum techniques. Commercially available reagents were used without further purification. Dry DMF for reactions was purified by the solvent drying system MBraun MB-SPS-5-BenchTop under nitrogen atmosphere (H_2O content < 20 ppm as determined by Karl-Fischer titration). Unless specified otherwise, all other solvents were used as commercially supplied. Column chromatography was carried out using SiO_2 60 Å or activated neutral aluminum oxide 60 Å (Brockmann activity grade I) as stationary phase. Petroleum ether (PE) 40−60 °C was used unless specified otherwise. (2*E*,4*E*,6*E*)-2,4,6-Octatrienal (compound **S5**) was prepared as reported previously.[1]

$^{1}H/^{13}C$ NMR spectra were recorded at 298 K using a Bruker AVIIIHD 400 nanobay or Bruker AVII 500 with ^{13}C cryoprobe. NMR spectra are reported in ppm; coupling constants (*J*) are reported in Hertz, to the nearest 0.1 Hz. Chemical shifts δ are calibrated by the residual solvent signals ($CDCl_3$: δ_H = 7.26 ppm, δ_C = 77.0 ppm; CD_3CN: δ_H = 1.94 ppm, δ_C = 1.3 and 118.3 ppm; d_6-DMSO: δ_H = 2.50 ppm, δ_C = 39.5 ppm). UV-vis-NIR absorption spectra were recorded in solution at 298 K using a Perkin-Elmer Lambda 20 spectrophotometer and a Jasco V-770 UV-visible/NIR spectrophotometer in fused silica cuvettes with a 1 cm pathlength. Molar absorption coefficients are reported in L mol^{-1} cm^{-1}. Fluorescence spectra were acquired at 298 K using an Edinburgh Instruments FS5 spectrofluorometer operating Fluoracle® software, and equipped with a xenon arc lamp (providing 230–1000 nm excitation range), a thermostatic sample holder (SC-20) and both an R13456 PMT detector (200–950 nm spectral range, Hamamatsu) and an InGaAs analogue NIR detector (850–1650 nm spectral range). The absolute quantum yields were measured using an integrating sphere (SC-30).

Section 1.2. Synthetic Schemes

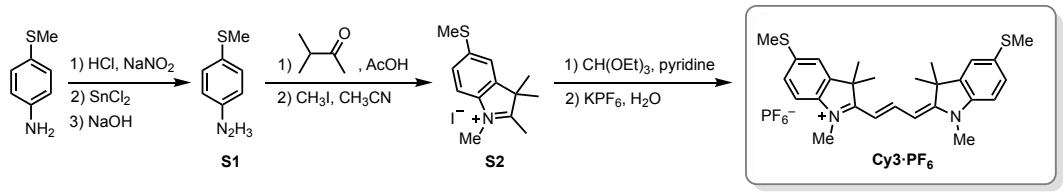

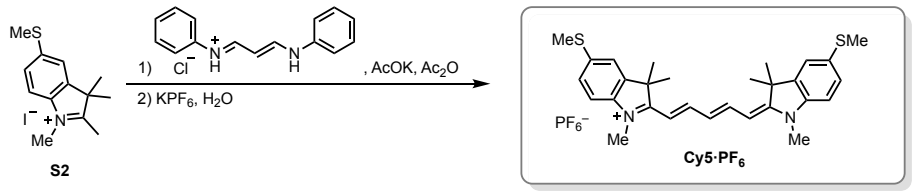

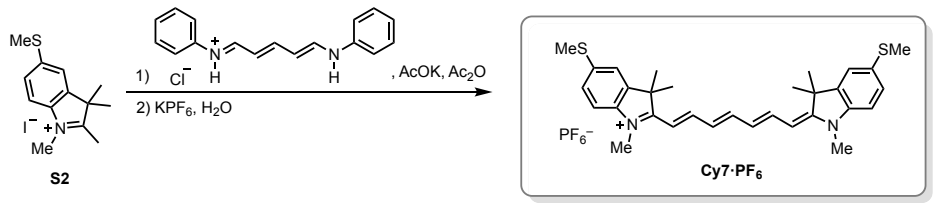

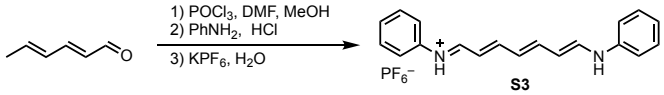

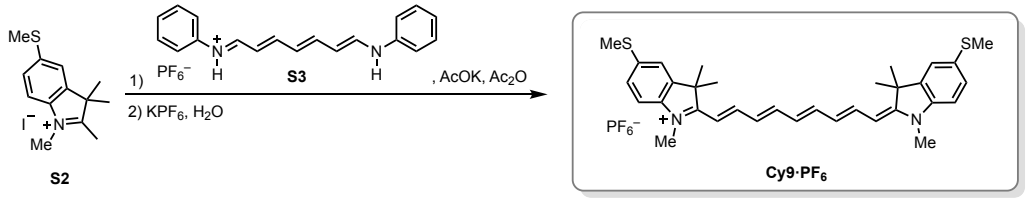

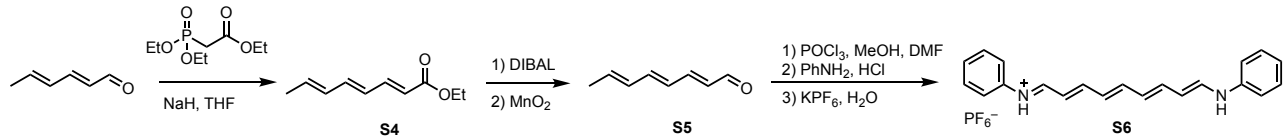

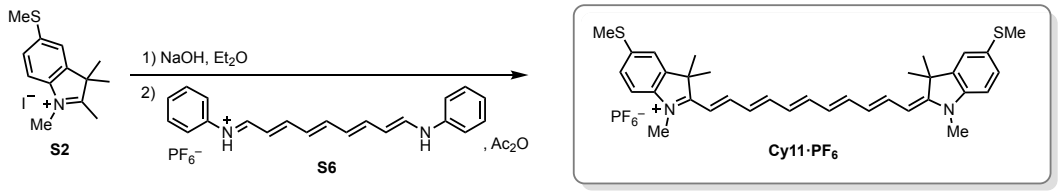

Section 1.3. Synthetic Methods

Synthesis of **4-methylthio-phenyl hydrazine (S1).** This compound was prepared using a modification of the procedure reported by Ahlström et al.[2] 4-Methylthio-aniline (3.48 g, 25.0 mmol) were added to aqueous HCl (37%, 12 M, 32.0 mL). The slurry was cooled to 0 °C. A chilled solution of $NaNO_2$ (1.37 g, 19.8 mmol) in H_2O (16.0 mL) was added dropwise at the same temperature. After stirring for 30 min, a solution of $SnCl_2 \cdot 2H_2O$ (12.8 g, 56.6 mmol) in aqueous HCl (37%, 13.0 mL) was added. After stirring for 3 h, the precipitate was collected by filtration. The solid was then added to aqueous sodium hydroxide (1.0 M, 20 mL) and stirred for 1 h. Extracting with CH_2Cl_2 then removing the solvent under vacuum gave compound **S1** (2.69 g, 70%) as a brown oil.

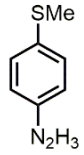

^{1}H NMR (400 MHz, $CDCl_3$, 298 K): δ_H 7.32–7.24 (m, 2H), 6.85–6.76 (m, 2H), 5.19 (bs, 1H), 3.59 (bs, 2H), 2.45 (s, 3H).

Synthesis of **5-methylthio-2,3,3-tetramethylindolenine (S2).** This compound was prepared using a similar procedure to that reported by Fung et al.[3] Compound **S1** (2.69 g, 17.4 mmol) was dissolved in acetic acid (15 mL), then *iso*-propylmethyl ketone (5.00 mL, 46.6 mmol) and conc. H_2SO_4 (0.2 mL, 3.7 mmol) were added to the solution. The solution was heated to reflux for 18 h. After cooling to room temperature, the solution was neutralized by saturated aqueous sodium bicarbonate. Extracting with diethyl ether and removing the solvent under vacuum gave a dark red oil, which was used for methylation without further purification. The oil was dissolved in CH_3CN (7 mL) and iodomethane (10 mL), and stirred at room temperature for 7 h. Filtration and washing with CH_2Cl_2 gave compound **S2** as a yellow solid (3.71 g, 61%).

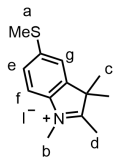

^{1}H NMR (400 MHz, d_6-DMSO, 298 K): δ_H 7.82 (d, J = 8.5 Hz, 1H, H_f), 7.75 (d, J = 1.8 Hz, 1H, H_g), 7.46 (dd, J = 8.5, 1.8 Hz, 1H, H_e), 3.94 (s, 3H, H_b), 2.73 (s, 3H, H_d), 2.58 (s, 3H, H_a), 1.52 (s, 6H, H_c).

^{13}C NMR (100 MHz, d_6-DMSO, 298 K): δ_C 194.2, 142.5, 140.1, 139.3, 125.5, 120.4, 115.4, 53.8, 34.7, 21.7, 14.9, 14.0.

HR MS (ESI+): *m/z* 220.1156 (M^+ 100%, $C_{13}H_{18}NS^+$ requires 220.1154).

Synthesis of **Cy3·PF$_6$.** This compound was prepared using a similar procedure to that reported by Gunasekaran et al.[4] Compound **S2** (0.15 g, 0.43 mmol) and triethyl orthoformate (0.19 g, 1.3 mmol) were added to pyridine (1 mL), and the solution was heated to reflux for 4 h under argon, then cooled to room temperature and filtered. The solid was washed with ether and dried, then dissolved in methanol (10 mL). The solution was added to saturated aqueous potassium hexafluorophosphate (100 mL). After stirring at room temperature for 2 h, the resulting precipitate was filtered and washed with water to yield **Cy3·PF$_6$** (80 mg, 62%) as a grey solid. Elemental analysis (%) calcd for $C_{27}H_{33}F_6N_2PS_2$: C 54.53, H5.59, N 4.71; found: C 54.36, H 5.71, N 4.65.

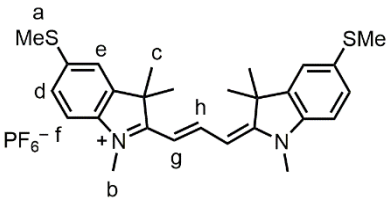

^{1}H NMR (500 MHz, d_6-DMSO, 298 K): δ_H 8.27 (t, J = 13.5 Hz, 1H, H_h), 7.59 (d, J = 1.8 Hz, 2H, H_e), 7.40 (d, J = 8.4 Hz, 2H, H_f), 7.33 (dd, J = 8.4, 1.8 Hz, 2H, H_d), 6.38 (d, J = 13.5 Hz, 2H, H_g), 3.61 (s, 6H, H_b), 2.54 (s, 6H, H_a), 1.68 (s, 12H, H_c).

^{13}C NMR (125 MHz, d_6-DMSO, 298 K): δ_C 173.3, 148.6, 141.5, 140.5, 135.2, 126.4, 120.9, 111.9, 102.6, 48.8, 31.4, 27.2, 15.7.

HR MS (ESI+): *m/z* 449.2079 ($[M]^+$ 100%, $C_{27}H_{33}N_2S_2^+$ requires 449.2080).

UV-vis ($CHCl_3$): λ / nm (ε / M^{-1} cm^{-1}): 589 (1.40×10^5).

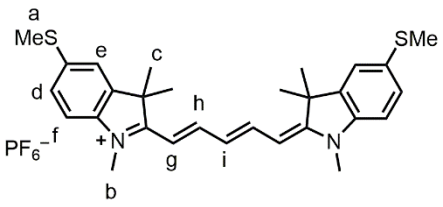

Synthesis of **Cy5·PF$_6$.** This compound was prepared using a similar procedure to that reported by Gunasekaran et al.[4] Compound **S2** (0.30 g, 0.86 mmol), malonaldehyde bisphenylimine monohydrochloride (0.15 g, 0.58 mmol) and potassium acetate (0.51 g, 5.2 mmol) were added to acetic anhydride (3.9 mL), then the slurry was heated to reflux for 1 h. The mixture was cooled to room temperature and filtered. The solid was washed with ether and water, then dissolved in methanol (10 mL). The solution was added to saturated aqueous potassium hexafluorophosphate (100 mL). After stirring at room temperature for 2 h, the resulting precipitate was filtered and washed with water to yield **Cy5·PF$_6$** (0.060 g, 22 %) as a blue solid.

^{1}H NMR (500 MHz, d_6-DMSO, 298K): δ_H 8.28 (dd, J = 13.8, 12.4 Hz, 2H, H_h), 7.59 (d, J = 1.8 Hz, 2H, H_e), 7.33 (d, J = 8.4 Hz, 2H, H_f), 7.29 (dd, J = 8.4, 1.8 Hz, 2H, H_d), 6.51 (t, J = 12.4 Hz, 1H, H_i), 6.23 (d, J = 13.8 Hz, 2H, H_g), 3.57 (s, 6H, H_b), 2.53 (s, 6H, H_a), 1.68 (s, 12H, H_c) ppm.

^{13}C NMR (125 MHz, d_6-DMSO, 298K) δ_C 172.2, 153.3, 142.0, 140.6, 134.5, 126.4, 125.2, 120.9, 111.4, 103.2, 48.8, 31.2, 26.9, 15.8 ppm.

HR MS (ESI+): *m/z* 475.2234 ($[M]^+$ 100%, $C_{29}H_{35}N_2S_2^+$ requires 475.2236).

UV-vis ($CHCl_3$): λ / nm (ε / M^{-1} cm^{-1}): 690 (2.14×10^5).

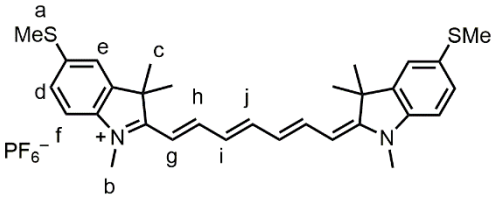

Synthesis of **Cy7·PF$_6$.** This compound was prepared using a similar procedure to that reported by Gunasekaran et al.[4] Compound **S2** (73 mg, 0.21 mmol), N-[5-(phenylamino)-2,4-pentadienylidine] aniline monohydrochloride (30 mg, 0.10 mmol) and potassium acetate (128 mg, 1.30 mmol) were added to acetic anhydride (2 mL), then heated to 70 °C for 1 h under nitrogen. The reaction mixture was cooled to room temperature and then diethyl ether (70 mL) was added. The precipitate was collected by filtration, and then dissolved in methanol (12 mL). The solution was added to saturated aqueous potassium hexafluorophosphate (200 mL). The solid was collected by filtration, and recrystallized from dichloromethane and petrol ether. The solid was dissolved in dichloromethane again, filtered through a syringe filter. Removing the dichloromethane of the filtrate under vacuum gave **Cy7·PF$_6$** (42 mg, 62%) as a dark solid. Elemental analysis (%) calcd for $C_{31}H_{37}F_6N_2PS_2$: C 57.57, H5.77, N 4.33; found: C 57.42, H 5.88, N 4.28.

^{1}H NMR (500 MHz, d_6-DMSO, 298 K): δ_H 7.82 (t, J = 13.1 Hz, 2H, H_h), 7.70 (t, J = 13.1 Hz, 1H, H_j), 7.54 (d, J = 1.6 Hz, 2H, H_e), 7.35–7.25 (m, 4H, H_d and H_f), 6.50 (t, J = 13.1 Hz, 2H, H_i), 6.27 (d, J = 13.1 Hz, 2H, H_g), 3.55 (s, 6H, H_b), 2.52 (s, 6H, H_a), 1.63 (s, 12H, H_c) ppm.

^{13}C NMR (125 MHz, d_6-DMSO, 298 K): δ_C 170.8, 155.3, 150.0, 141.9, 140.8, 134.3, 126.5, 125.2, 120.8, 111.3, 103.9, 48.6, 31.2, 27.0, 15.7 ppm.

HR MS (ESI+): *m/z* 501.2392 ([M]$^+$ 100%, $C_{31}H_{37}N_2S_2^+$ requires 501.2393).

UV-vis-NIR ($CHCl_3$): λ / nm (ε / M^{-1} cm^{-1}): 784 (1.80×10^5).

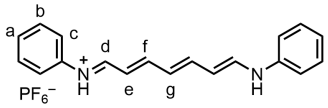

Synthesis of **N-((1*E*,2*E*,4*E*,6*E*)-7-(phenylamino)hepta-2,4,6-trien-1-ylidene)benzenaminium hexaflorophosphate (S3).** (The synthesis of this compound has previously been reported as a chloride salt.[5]) $POCl_3$ (3.6 mL, 38 mmol) was added dropwise to a solution of dry DMF (8.0 mL, 104 mmol) and MeOH (1.7 mL, 42 mmol) at 0 °C. After 10 min the temperature was raised to room temperature, and (2*E*, 4*E*)-2,4-hexadienal (2.2 mL, 20 mmol) was added dropwise to give a dark brown solution. The solution was then heated to 80 °C for 3 h. The reaction mixture was poured onto ice (80 g), then aqueous aniline hydrochloride (13.0 g, 100 mmol, in 120 mL H_2O) was added. 10% aqueous KOH (80 mL) was then added to basify the mixture. A saturated aqueous solution of KPF_6 (240 mL) was added to the reaction mixture and was allowed to sit overnight. The solution was filtered to obtain black precipitate. The precipitates were dissolved in dichloromethane and then filtered through a plug of silica. Recrystallization by dissolving in CH_2Cl_2 and layered addition of petrol ether gave compound **S3** (2.40 g, 29%) as a purple solid.

^{1}H NMR (400 MHz, d_6-acetone, 298 K): δ_H 8.48 (d, J = 12.2 Hz, 2H, H_d), 7.73 (t, J = 12.2 Hz, 2H, H_f), 7.50–7.43 (m, 4H, H_b), 7.42–7.36 (m, 4H, H_c), 7.32–7.18 (m, 2H, H_a), 6.56 (t, J = 12.2 Hz, 1H, H_g), 6.38 (t, J = 12.2 Hz, 2H, H_e).

^{13}C NMR (125 MHz, d_6-acetone, 298 K): δ_C 161.8, 154.7, 140.0, 130.9, 126.7, 123.5, 118.4, 111.8 ppm.

HR MS (ESI+): *m/z* 275.1544 (M^+ 100%, $C_{19}H_{19}N_2^+$ requires 275.1543).

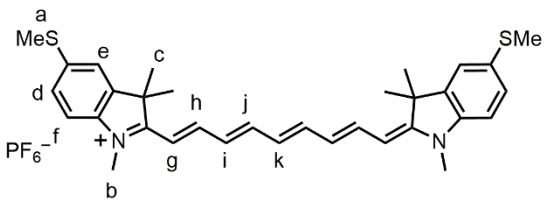

Synthesis of **Cy9·PF$_6$.** Compound **S2** (0.24 g, 0.69 mmol), bisphenylaminoheptamethine **S3** (0.10 g, 0.24 mmol), potassium acetate (0.37 g, 3.8 mmol) were added to acetic anhydride (4.5 mL) and stirred at room temperature for 4 h. Diethyl ether (200 mL) was added to the solution and the precipitate was filtered. The solid was dissolved in MeOH (25 mL), and added to saturated aqueous KPF_6 solution (1.0 L). The precipitate was collected by filtration, then dissolved in CH_2Cl_2, and passed through a PTFE syringe filter. Column chromatography (washed by CH_2Cl_2 then CH_2Cl_2/ MeOH 9:1) gave **Cy9·PF$_6$** (67 mg, 42%) as a dark solid.

^{1}H NMR (500 MHz, DMSO, 298 K): δ_H 7.78 (t, J = 12.9 Hz, 2H, H_h), 7.52 (d, J = 1.3 Hz, 2H, H_e), 7.35 (t, J = 12.9 Hz, 2H, H_j), 7.28 (m, 4H, H_d and H_f), 6.50 (t, J = 12.9 Hz, 2H, H_i), 6.46 (t, J = 12.9 Hz, 1H, H_k), 6.23 (d, J = 12.9 Hz, 2H, H_g), 3.53 (s, 6H, H_b), 2.51 (s, 6H, H_a), 1.62 (s, 12H, H_c) ppm.

^{13}C NMR (125 MHz, d_6-DMSO, 298 K): δ_C 169.7, 150.8, 147.4, 141.5, 140.3, 134.0, 127.1, 126.8, 126.2, 120.5, 111.2, 104.6, 48.0, 31.2, 26.9, 15.9 ppm.

HR MS (ESI+): *m/z* 527.2550 (M^+ 100%, $C_{33}H_{39}N_2S_2^+$ requires 527.2549).

UV-vis-NIR ($CHCl_3$): λ / nm (ε / M^{-1} cm^{-1}): 894 (1.31×10^5).

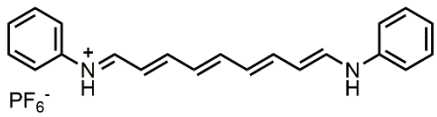

Synthesis of **N-((1*E*,2*E*,4*E*,6*E*,8*E*)-9-(phenylamino)nona-2,4,6,8-tetraen-1-ylidene)benzenaminium hexafluorophosphate (S6).** (The synthesis of this compound has previously been reported as a chloride salt.[5]) $POCl_3$ (0.46 mL, 4.9 mmol) was added dropwise to a solution of dry DMF (1.0 mL, 13.0 mmol) and MeOH (0.22 mL, 5.3 mmol) at 0 °C with nitrogen atmosphere. After 10 minutes the temperature was raised to room temperature, and a solution of compound **S5** (0.24 g, 2.0 mmol) in dry DMF (1.0 mL, 13.0 mmol) was added dropwise. The solution was then heated to 50 °C for 2.5 h. After cooling, the reaction mixture was poured onto ice (20 g), then aqueous aniline hydrochloride (1.79 g, 13.9 mmol, in 30 mL H_2O) was added. Aqueous KOH (10%) was then added dropwise to neutralize the solution to pH 7. Saturated aqueous KPF_6 (30 mL) was added and the reaction mixture was stirred at room temperature for 2 h. The solid was collected by filtration, and recrystallized by CH_2Cl_2/PE. The solid was dissolved in CH_2Cl_2, and the insoluble impurities were removed by filtration. The filtrate was collected and the solvent was removed under vacuum. Solid was dissolved in CH_2Cl_2 (35 mL) and aniline (3 mL) was added and stirred for 1 h at room temperature. The product was precipitated by adding the solution to PE (200 mL) and purified by recrystallized with CH_2Cl_2/PE and to yield **S6** as a black solid (0.11 g, 12%, crude). This material was used for next step as a crude product without further purification.

HR MS (ESI+): *m/z* 301.1701 ($[M]^+$ 100%, $C_{21}H_{21}N_2^+$ requires 301.1699).

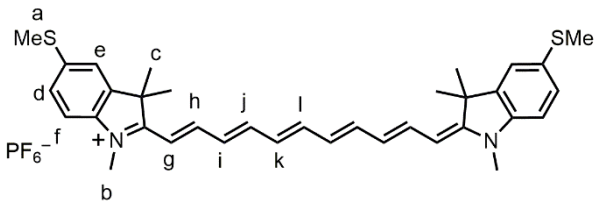

Synthesis of **Cy11·PF$_6$.** Compound **S2** (117 mg, 0.34 mmol) was added to aqueous sodium hydroxide (1.0 M, 20 mL, 20 mmol) and diethyl ether (10 mL). The mixture was stirred at room temperature for 15 min, then the organic layer was separated, and the aqueous layer was extracted with diethyl ether. The organic phase was combined, then the solvent was removed under vacuo to give a yellow liquid. The liquid was dissolved in acetic anhydride (3 mL) and added to compound **S6** (32 mg, 0.07 mmol). After stirring at room temperature for 1.5 h, diethyl ether (75 mL) was added to the solution and the precipitate was filtered. The solid was dissolved in CH_2Cl_2 and filtered through a PTFE syringe filter. The solvent of filtrate was removed under vacuum to give a black solid, which contained compound **Cy11·PF$_6$** as the main product together with **Cy3**, **Cy5**, **Cy7** and **Cy9** impurities. The product was purified by column chromatography on neutral alumina (washed by CH_2Cl_2 then acetone). Compound **Cy3**, **Cy5**, **Cy7** and **Cy9** eluted first when flushing column with acetone, and the fractions were monitored by UV-vis-NIR spectrometry and mass spectrometry. The fractions with pure **Cy11** were collected and the solvent was removed under vacuum. Washing with petroleum ether gave **Cy11·PF$_6$** (2 mg, 4%) as a black solid.

^{1}H NMR (500 MHz, CD_3CN, 298 K): δ_H 7.58 (t, J = 13.2 Hz, 2H, H_h), 7.37 (d, J = 1.8 Hz, 2H, H_e), 7.29 (dd, J = 8.4, 1.8 Hz, 2H, H_d), 7.14 (t, J = 13.2 Hz, 2H, H_j), 7.09 (d, J = 8.4 Hz, 2H, H_f), 6.97 (t, J = 13.2 Hz, 1H, H_l), 6.45 (t, J = 13.2 Hz, 4H, H_i and H_k), 6.12 (d, J = 13.2 Hz, 2H, H_g), 3.46 (s, 6H, H_b), 2.51 (s, 6H, H_a), 1.62 (s, 12H, H_c) ppm.

^{13}C NMR (125 MHz, CD_3CN, 298 K): δ_C 170.3, 149.1, 148.0, 146.6, 143.1, 142.5, 135.6, 129.1, 128.3, 128.1, 122.1, 111.7, 105.6, 49.6, 32.1, 27.5, 16.9 ppm.

HR MS (ESI+): *m/z* 553.2703 (M^+ 100%, $C_{33}H_{39}N_2S_2^+$ requires 553.2706).

UV-vis-NIR (CH_2Cl_2): λ / nm (ε / M^{-1} cm^{-1}): 1018 (2.27×10^5).

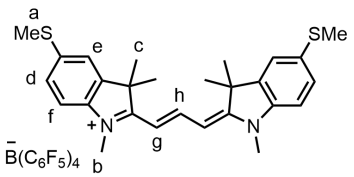

Synthesis of **Cy3·B(C_6F_5)$_4$.** **Cy3·PF_6** (15 mg, 25 μmol) and potassium tetrakis(pentafluorophenyl)borate (20 mg, 28 μmol) was dissolved in CH_2Cl_2 (10 mL) at room temperature for 10 min. After removing the precipitate (KPF_6) by filtration, the filtrate was passed through a plug of silica eluting with CH_2Cl_2, evaporated and dried under vacuum gave **Cy3·B(C_6F_5)$_4$** as a purple solid (27 mg, 95%).

^{1}H NMR (500 MHz, d_3-CH_3CN, 298 K): δ_H 8.38 (t, J = 13.5 Hz, 1H, H_h), 7.43 (d, J = 1.8 Hz, 2H, H_e), 7.32 (dd, J = 8.4, 1.8 Hz, 2H, H_d), 7.19 (d, J = 8.4, 2H, H_f), 6.23 (d, J = 13.5 Hz, 2H, H_g), 3.53 (s, 6H, H_b), 2.53 (s, 6H, H_a), 1.70 (s, 12H, H_c).

^{13}C NMR (125 MHz, d_3-CH_3CN, 298 K): δ_C 175.2, 150.5, 150.0, 148.1, 142.81, 141.76, 140.2, 138.3, 137.0, 136.3, 127.7, 121.7, 112.5, 103.3, 50.3, 32.2, 28.0, 16.5 ppm.

HR MS (ESI+): *m/z* 449.2079 ($[M]^+$ 100%, $C_{27}H_{33}N_2S_2^+$ requires 449.2080).

UV-vis ($CHCl_3$): λ / nm (ε / M^{-1} cm^{-1}): 592 (5.64×10^4).

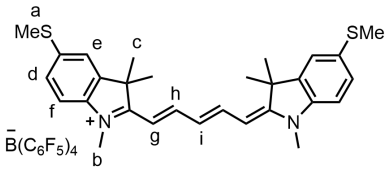

Synthesis of **Cy5·B(C_6F_5)$_4$.** **Cy5·PF_6** (8.0 mg, 13 μmol) and potassium tetrakis(pentafluorophenyl)borate (17 mg, 24 μmol) was dissolved in CH_2Cl_2 (10 mL) at room temperature for 10 min. After removing the precipitate (KPF_6) by filtration, the filtrate was passed through a plug of silica eluting with CH_2Cl_2, evaporated and dried under vacuum to give **Cy5·B(C_6F_5)$_4$** as a blue solid (13 mg, 87 %).

^{1}H NMR (400 MHz, d_6-acetone, 298 K): δ_H 8.36 (dd, J = 13.8, 12.4 Hz, 2H, H_h), 7.52 (d, J = 1.8 Hz, 2H, H_e), 7.35 (dd, J = 8.4, 1.8 Hz, 2H, H_d), 7.32 (d, J = 8.4, 2H, H_f), 6.65 (t, J = 12.4 Hz, 1H, H_i), 6.34 (d, J = 13.8 Hz, 2H, H_g), 3.69 (s, 6H, H_b), 2.54 (s, 6H, H_a), 1.73 (s, 12H, H_c) ppm.

^{13}C NMR (125 MHz, d_6-acetone, 298 K): δ_C 173.8, 154.3, 150.0, 148.1, 143.1, 141.9, 140.0, 138.1, 136.5, 136.1, 127.8, 126.2, 121.9, 112.2, 104.1, 50.1, 31.7, 27.6, 16.4 ppm.

HR MS (ESI+): *m/z* 475.2235 ($[M]^+$ 100%, $C_{29}H_{35}N_2S_2^+$ requires 475.2236).

UV-vis-NIR ($CHCl_3$): λ / nm (ε / M^{-1} cm^{-1}): 695 (1.41×10^5).

Synthesis of **Cy7·B(C$_6$F$_5$)$_4$.** **Cy7·PF$_6$** (5.0 mg, 7.7 μmol) and potassium tetrakis(pentafluorophenyl)borate (16 mg, 22 μmol) were dissolved in CH_2Cl_2 (10 mL) at room temperature for 10 min. After removing the precipitate (KPF_6) by filtration, the filtrate was passed through a plug of silica eluting with CH_2Cl_2, evaporated and dried under vacuum to give **Cy7·B(C$_6$F$_5$)$_4$** as a green solid (8.0 mg, 88%).

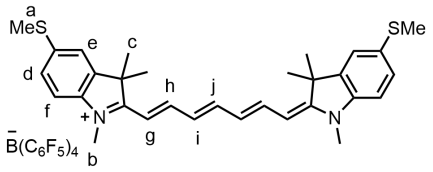

^{1}H NMR (500 MHz, d_3-CH_3CN, 298 K): δ_H 7.76 (t, J = 13.2 Hz, 2H, H_h), 7.51 (t, J = 13.2 Hz, 1H, H_j), 7.39 (d, J = 1.8 Hz, 2H, H_e), 7.29 (dd, J = 8.4, 1.8 Hz, 2H, H_d), 7.13 (d, J = 8.4 Hz, 2H, H_f), 6.48 (t, J = 13.2 Hz, 2H, H_i), 6.15 (d, J = 13.2 Hz, 2H, H_g), 3.48 (s, 6H, H_b), 2.52 (s, 6H, H_a), 1.64 (s, 12H, H_c) ppm.

^{13}C NMR (125 MHz, d_3-CH_3CN, 298 K): δ_C 172.5, 151.3, 150.0, 148.1, 143.1, 142.1, 140.2, 138.3, 136.2, 127.8, 126.3, 121.9, 118.3, 112.0, 104.6, 49.9, 32.0, 27.6, 16.7 ppm.

HR MS (ESI+): *m/z* 501.2391 ($[M]^+$ 100%, $C_{31}H_{37}N_2S_2^+$ requires 501.2393).

UV-vis ($CHCl_3$): λ / nm (ε / M^{-1} cm^{-1}): 798 (1.93 × 10^5).

Synthesis of **Cy9·B(C$_6$F$_5$)$_4$.** **Cy9·PF$_6$** (3.0 mg, 4.4 μmol) and lithium tetrakis(pentafluorophenyl)borate ethyl etherate (6.0 mg, 6.9 μmol) were dissolved in CH_2Cl_2 (1 mL) at room temperature for 10 min. After removing the precipitate ($LiPF_6$) by filtration, the filtrate was passed through a plug of silica eluting with CH_2Cl_2, evaporated and dried under vacuum to give **Cy9·B(C$_6$F$_5$)$_4$** as a dark solid (2.0 mg, 37%).

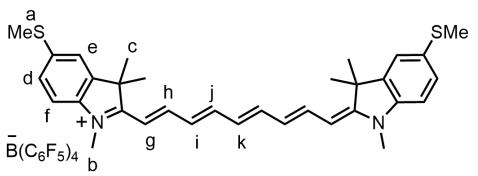

^{1}H NMR (500 MHz, d_6-acetone, 298 K): δ_H 7.87 (t, J = 13.1 Hz, 2H, H_h), 7.50 (d, J = 1.8 Hz, 2H, H_e), 7.37 (t, J = 13.1 Hz, 2H, H_j), 7.34 (dd, J = 8.4, 1.8 Hz, 2H, H_d), 7.27 (d, J = 8.4 Hz, 2H, H_f), 6.55 (t, J = 13.1 Hz, 2H, H_i), 6.50 (t, J = 13.1 Hz, 1H, H_k), 6.31 (d, J = 13.1 Hz, 2H, H_g), 3.66 (s, 6H, H_b), 2.53 (s, 6H, H_a), 1.71 (s, 12H, H_c) ppm.

^{13}C NMR (125 MHz, d_6-acetone, 298K): δ_C 172.4, 156.5, 151.5, 150.0, 148.1, 143.0, 142.0, 140.0, 138.1, 136.3, 127.9, 126.4, 121.9, 112.0, 104.7, 49.9, 31.7, 27.7, 16.5 ppm.

HR MS (ESI+): *m/z* 527.2550 (M^+ 100%, $C_{33}H_{39}N_2S_2^+$ requires 527.2549).

UV-vis-NIR ($CHCl_3$): λ / nm (ε / M^{-1} cm^{-1}): 912 (1.91 × 10^5).

Synthesis of **Cy11·B(C$_6$F$_5$)$_4$.** **Cy11·PF$_6$** (3.0 mg, 4.3 μmol) and potassium tetrakis(pentafluorophenyl)borate (10 mg, 14 μmol) were dissolved in CH_2Cl_2 (1 mL) at room temperature for 10 min. After removing the precipitate (KPF_6) by filtration, the filtrate was passed through a plug of alumina eluting with CH_2Cl_2, evaporated and dried under vacuum to give **Cy11·B(C$_6$F$_5$)$_4$** as a black solid (3.0 mg, 57%).

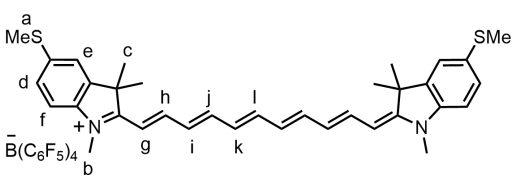

^{1}H NMR (500 MHz, d_6-acetone, 298 K): δ_H 7.78 (t, J = 13.1 Hz, 2H, H_h), 7.50 (d, J = 1.8 Hz, 2H, H_e), 7.33 (dd, J = 8.4, 1.8 Hz, 2H, H_d), 7.29–7.14 (m, 4H, H_f and H_j), 6.98 (t, J = 13.1 Hz, 1H, H_l), 6.52 (t, J = 13.1 Hz, 2H, H_k), 6.49 (t, J = 13.1 Hz, 2H, H_i), 6.31 (d, J = 13.1 Hz, 2H, H_g), 3.65 (s, 6H, H_b), 2.53 (s, 6H, H_a), 1.71 (s, 12H, H_c) ppm.

^{13}C NMR (125 MHz, d_6-acetone, 298 K): δ_C 170.2, 150.0, 149.3, 148.0, 146.7, 143.0, 142.4, 140.0, 138.1, 135.8, 129.1, 128.5, 128.2, 122.2, 111.7, 105.8, 49.6, 31.8, 27.5, 16.7 ppm.

HR MS (ESI+): *m/z* 553.2704 (M^+ 100%, $C_{33}H_{39}N_2S_2^+$ requires 553.2706).

UV-vis-NIR ($CHCl_3$): λ / nm (ε / M^{-1} cm^{-1}): 1025 (2.01×10^5).

Note on the stability of ***Cy11·PF$_6$*** *and* ***Cy11·B(C$_6$F$_5$)$_4$***: These compounds are stable at room temperature under air in the dark, with no detectable decomposition after several months, but they have poor stability when exposed to light, acid (e.g. 1% trifluoroacetic acid), base (e.g. pyridine) or heat (e.g. above 50 °C).

Section 2. UV-Visible-NearIR Absorption and Fluorescence Spectroscopy

Table 1. Absorption maxima of cyanine dye molecular wires in different solvents (molar absorption coefficient in the brackets, ε / M^{-1} cm^{-1}).

cyanine \ solvent	toluene	THF	$CHCl_3$	CH_2Cl_2	acetone	CH_3CN	DMSO	MeOH	CS_2	dioxane
Cy3·PF$_6$	595 nm (5.71×10^4)	586 nm (5.85×10^4)	590 nm (6.40×10^4)	590 nm (5.97×10^4)	576 nm (6.16×10^4)	575 nm (5.54×10^4)	582 nm (5.69×10^4)	574 nm (6.15×10^4)	606 nm (7.62×10^4)	584 nm (4.75×10^4)
Cy3B·(C$_6$F$_5$)$_4$	594 nm (5.59×10^4)	586 nm (5.15×10^4)	592 nm (5.64×10^4)	590 nm (5.30×10^4)	578 nm (6.10×10^4)	576 nm (5.91×10^4)	584 nm (6.08×10^4)	577 nm (6.02×10^4)	607 nm (4.92×10^4)	587 nm (5.28×10^4)
Cy5·PF$_6$	684 nm (1.03×10^5)	679 nm (1.00×10^5)	688 nm (8.90×10^4)	689 nm (1.08×10^5)	670 nm (1.02×10^5)	669 nm (1.10×10^5)	676 nm (9.13×10^4)	669 nm (9.98×10^4)	697 nm (1.01×10^5)	679 nm (1.07×10^5)
Cy5·B(C$_6$F$_5$)$_4$	701 nm (1.42×10^5)	683 nm (1.34×10^5)	695 nm (1.41×10^5)	691 nm (1.57×10^5)	672 nm (1.33×10^5)	670 nm (1.34×10^5)	678 nm (1.37×10^5)	670 nm (1.46×10^5)	714 nm (1.53×10^5)	688 nm (1.66×10^5)
Cy7·PF$_6$	763 nm (1.12×10^5)	777 nm (1.07×10^5)	778 nm (1.02×10^5)	792 nm (1.35×10^5)	774 nm (9.89×10^4)	773 nm (9.74×10^4)	782 nm (8.65×10^4)	771 nm (1.02×10^5)	777 nm (9.70×10^4)	760 nm (1.02×10^5)
Cy7·B(C$_6$F$_5$)$_4$	806 nm (1.92×10^5)	786 nm (1.57×10^5)	798 nm (1.93×10^5)	795 nm (1.80×10^5)	775 nm (1.42×10^5)	774 nm (1.42×10^5)	779 nm (1.36×10^5)	772 nm (1.49×10^5)	818 nm (1.67×10^5)	790 nm (1.97×10^5)
Cy9·PF$_6$	899 nm (8.22×10^4)	900 nm (1.51×10^5)	907 nm (1.84×10^5)	905 nm (2.27×10^5)	883 nm (1.19×10^5)	878 nm (1.20×10^5)	894 nm (1.03×10^5)	877 nm (1.27×10^5)	930 nm (1.12×10^5)	873 nm (8.50×10^4)
Cy9·B(C$_6$F$_5$)$_4$	909 nm (1.82×10^5)	900 nm (1.28×10^5)	912 nm (1.91×10^5)	908 nm (1.78×10^5)	884 nm (9.56×10^4)	880 nm (9.25×10^4)	896 nm (8.68×10^4)	878 nm (1.10×10^5)	923 nm (1.87×10^5)	898 nm (1.71×10^5)
Cy11·PF$_6$	942 nm (8.31×10^4)	1002 nm (1.13×10^5)	1019 nm (1.65×10^5)	1018 nm (2.27×10^5)	864 nm (6.84×10^4)	846 nm (6.74×10^4)	1001 nm (7.01×10^4)	983 nm (4.71×10^4)	975 nm (1.00×10^5)	813 nm (8.02×10^4)
Cy11·B(C$_6$F$_5$)$_4$	1014 nm (1.52×10^4)	1008 nm (8.92×10^4)	1025 nm (2.01×10^5)	1017 nm (1.75×10^5)	989 nm (5.11×10^4)	985 nm (3.94×10^4)	1002 nm (4.11×10^4)	984 nm (5.48×10^4)	1027 nm (1.91×10^5)	998 nm (1.32×10^5)

Table 2. Fluorescence quantum yields (all measured for PF_6 salts in dichloromethane).

cyanine	quantum yield	excitation wavelength	peak emission wavelength	measurement technique
Cy3·PF$_6$	9.1 ± 1.3 %	562 nm	626 nm	integrating sphere
Cy5·PF$_6$	10.4 ± 1.0 %	650 nm	725 nm	integrating sphere
Cy7·PF$_6$	9.9 ± 0.5%	733 nm	831 nm	reference: indocyanine green in ethanol[a]
Cy9·PF$_6$	15.5 ± 4.6%	900 nm	942 nm	reference: IR-1061 in CH_2Cl_2[b]
Cy11·PF$_6$	2.8 ± 1.4%	960 nm	1068 nm	reference: IR-1061 in CH_2Cl_2[b]

a: ϕ_F = 0.283 ± 0.017 (ref. 6). *b*: ϕ_F = 0.012 ± 0.004 (ref. 7).

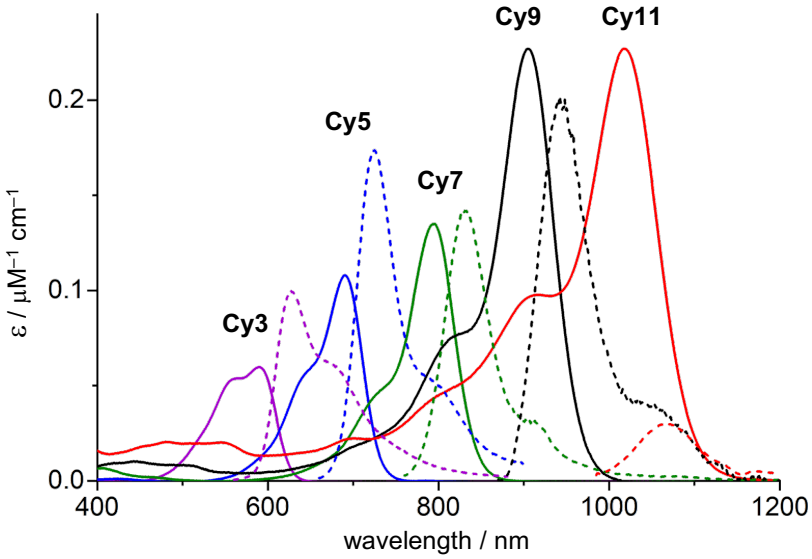

Figure S1. UV-vis-NIR absorption and fluorescence spectra of compounds **Cy3·PF$_6$**, **Cy5·PF$_6$**, **Cy7·PF$_6$**, **Cy9·PF$_6$** and **Cy11·PF$_6$** recorded in CH_2Cl_2. The intensities for the fluorescence spectra are scales so that the areas of the peaks are proportional to the quantum yields.

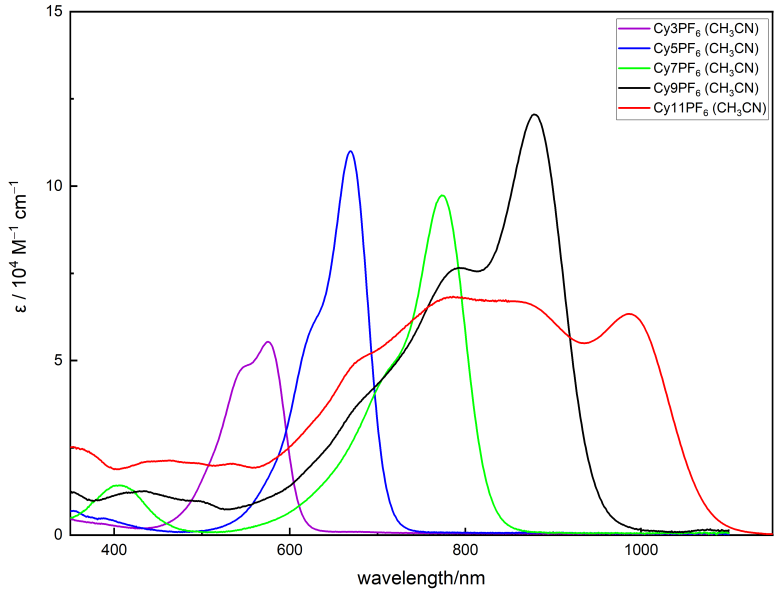

Figure S2. UV-vis absorption spectra of compounds **Cy3·PF$_6$**, **Cy5·PF$_6$**, **Cy7·PF$_6$**, **Cy9·PF$_6$** and **Cy11·PF$_6$** recorded in CH_3CN.

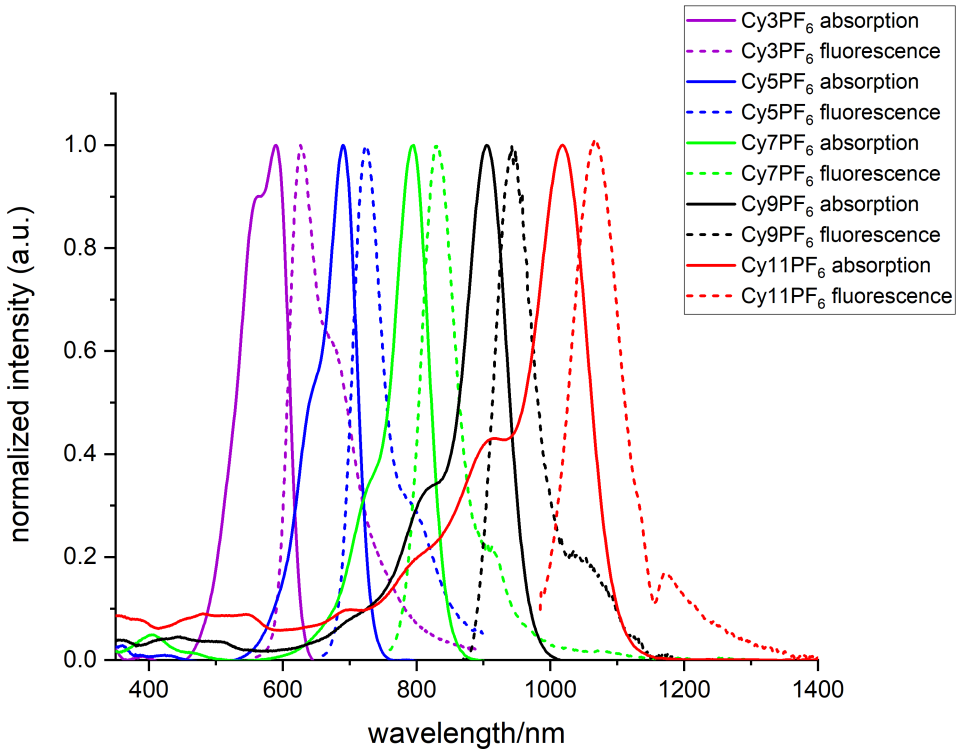

Figure S3. Normalized fluorescence and UV-vis-NIR absorption spectra of compounds **Cy3·PF$_6$**, **Cy5·PF$_6$**, **Cy7·PF$_6$**, **Cy9·PF$_6$** and **Cy11·PF$_6$** recorded in CH_2Cl_2. Excitation wavelengths: **Cy3·PF$_6$**: 550 nm, **Cy5·PF$_6$**: 654 nm, **Cy7·PF$_6$**: 754 nm, **Cy9·PF$_6$**: 834 nm and **Cy11·PF$_6$**: 973 nm.

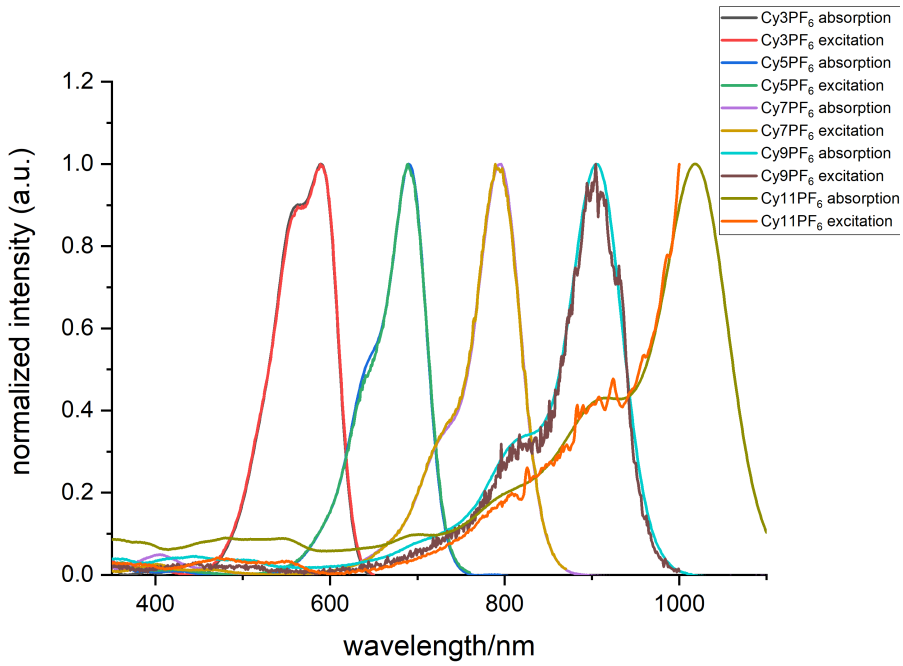

Figure S4. Normalized UV-vis-NIR absorption and excitation spectra of **Cy3·PF$_6$**, **Cy5·PF$_6$**, **Cy7·PF$_6$**, **Cy9·PF$_6$** and **Cy11·PF$_6$** recorded in CH_2Cl_2. Detection wavelengths: **Cy3·PF$_6$**: 660 nm, **Cy5·PF$_6$**: 775 nm, **Cy7·PF$_6$**: 880 nm, **Cy9·PF$_6$**: 980 nm and **Cy11·PF$_6$**: 1068 nm.

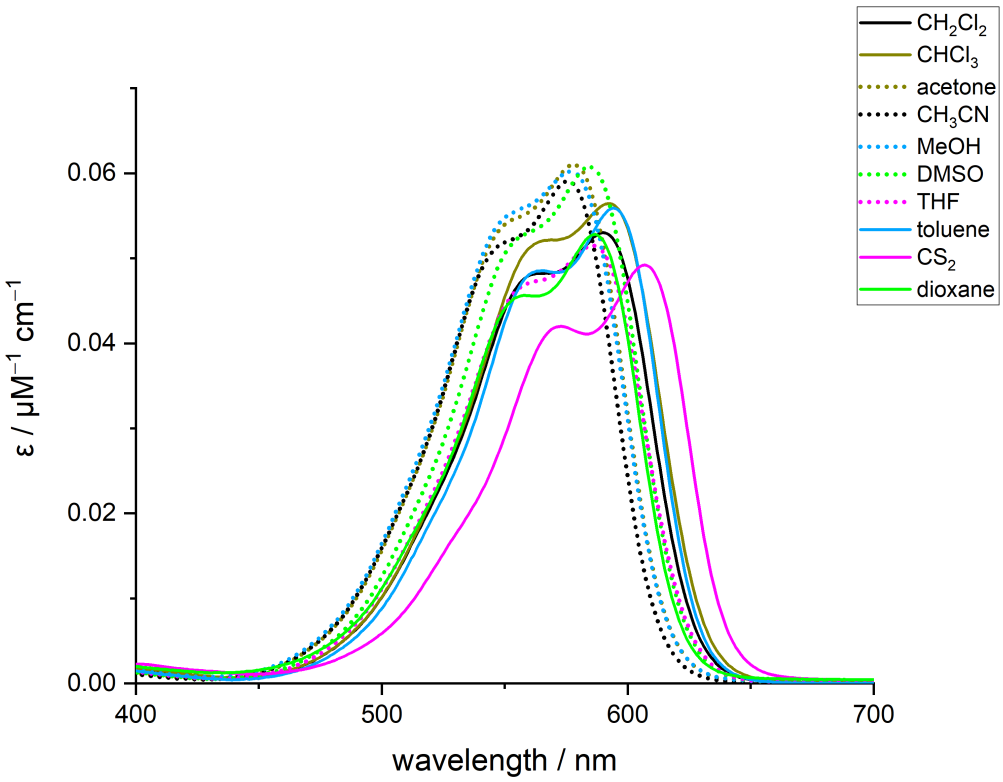

Figure S5. UV-vis-NIR absorption spectra of compounds **Cy3·B(C$_6$F$_5$)$_4$** recorded in a range of solvents: dichloromethane, chloroform, acetone, acetonitrile, methanol, DMSO, THF and toluene.

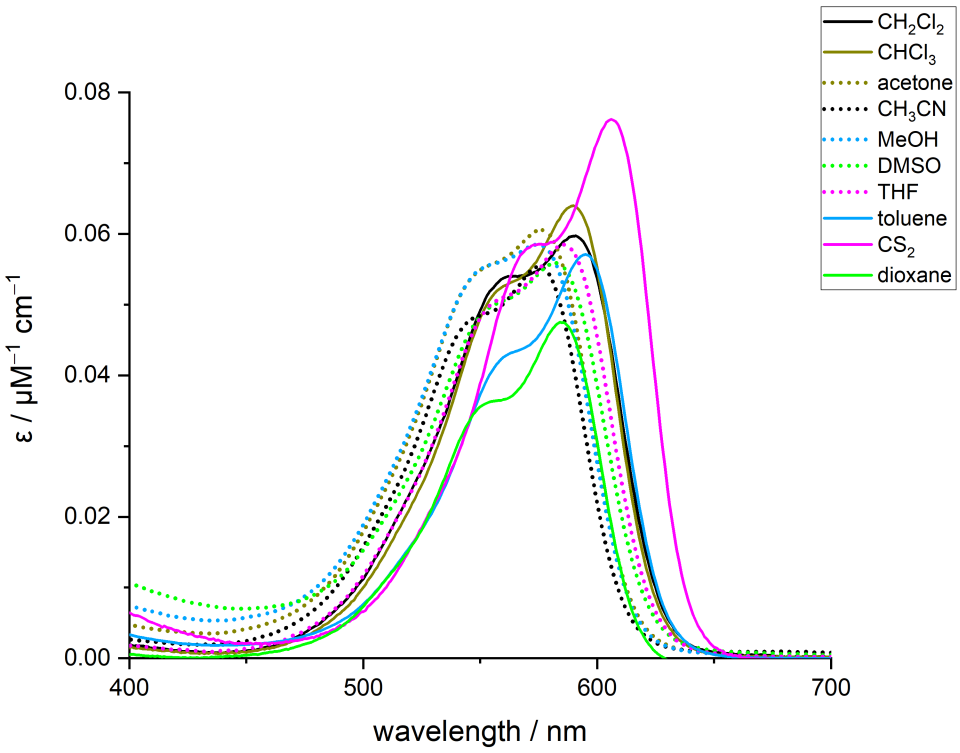

Figure S6. UV-vis-NIR absorption spectra of compounds **Cy3·PF$_6$** recorded in a range of solvents: dichloromethane, chloroform, acetone, acetonitrile, methanol, DMSO, THF and toluene.

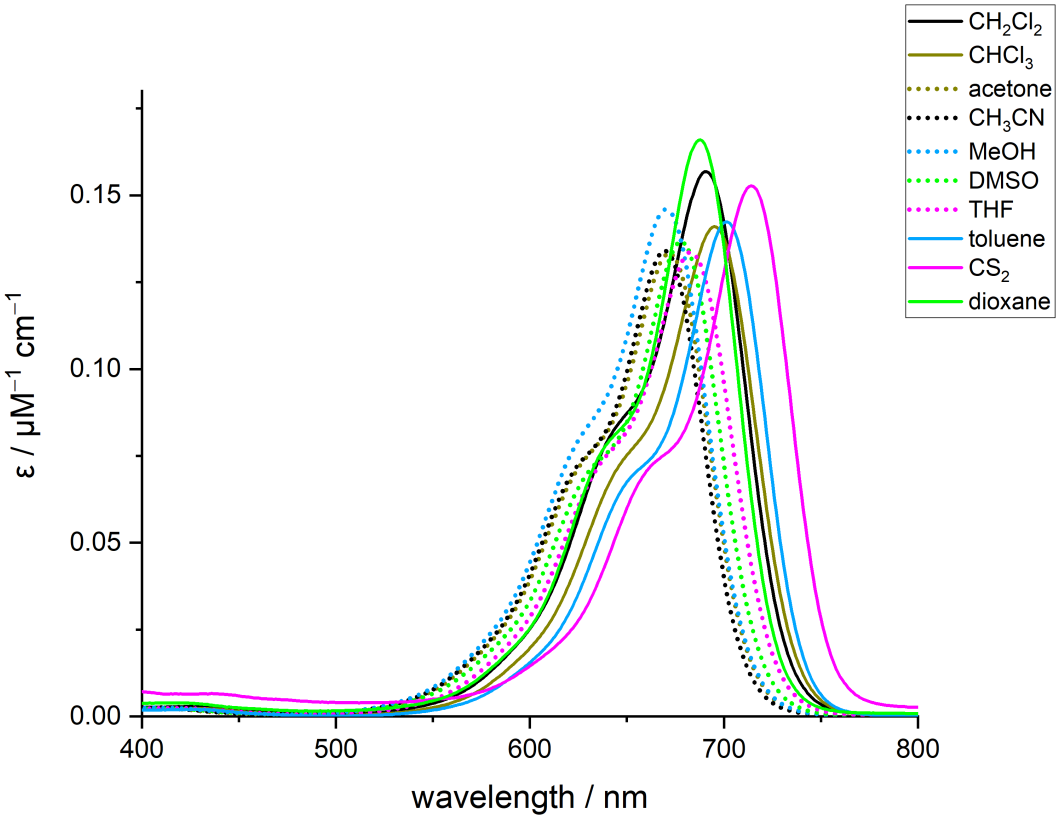

Figure S7. UV-vis-NIR absorption spectra of compounds **Cy5·B(C$_6$F$_5$)$_4$** recorded in a range of solvents: dichloromethane, chloroform, acetone, acetonitrile, methanol, DMSO, THF and toluene.

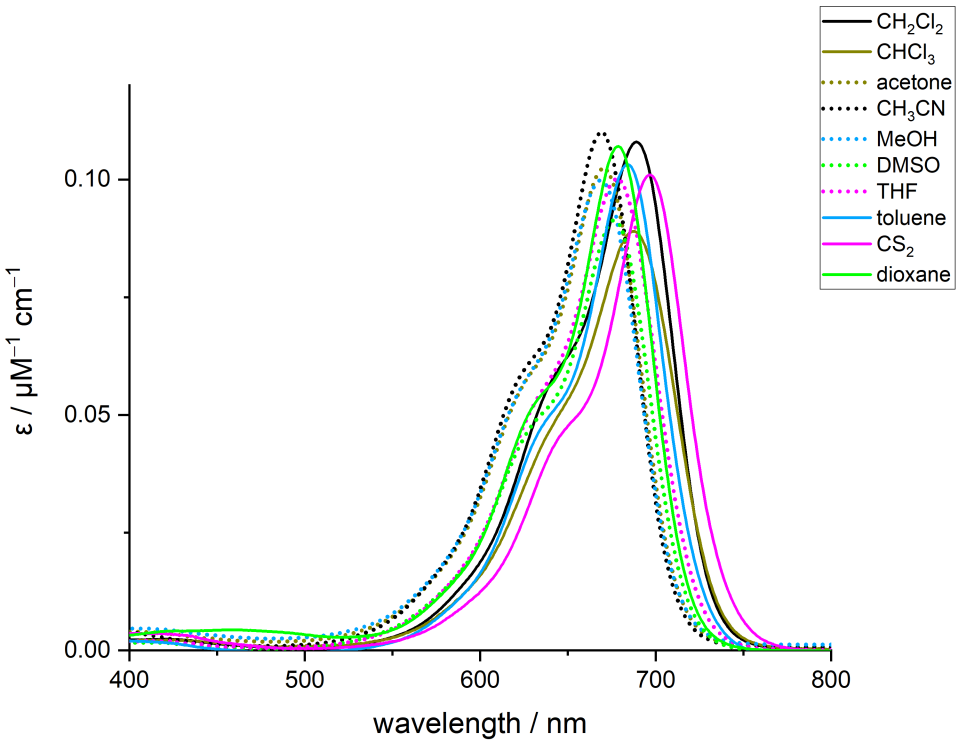

Figure S8. UV-vis-NIR absorption spectra of compounds **Cy5·PF$_6$** recorded in a range of solvents: dichloromethane, chloroform, acetone, acetonitrile, methanol, DMSO, THF and toluene.

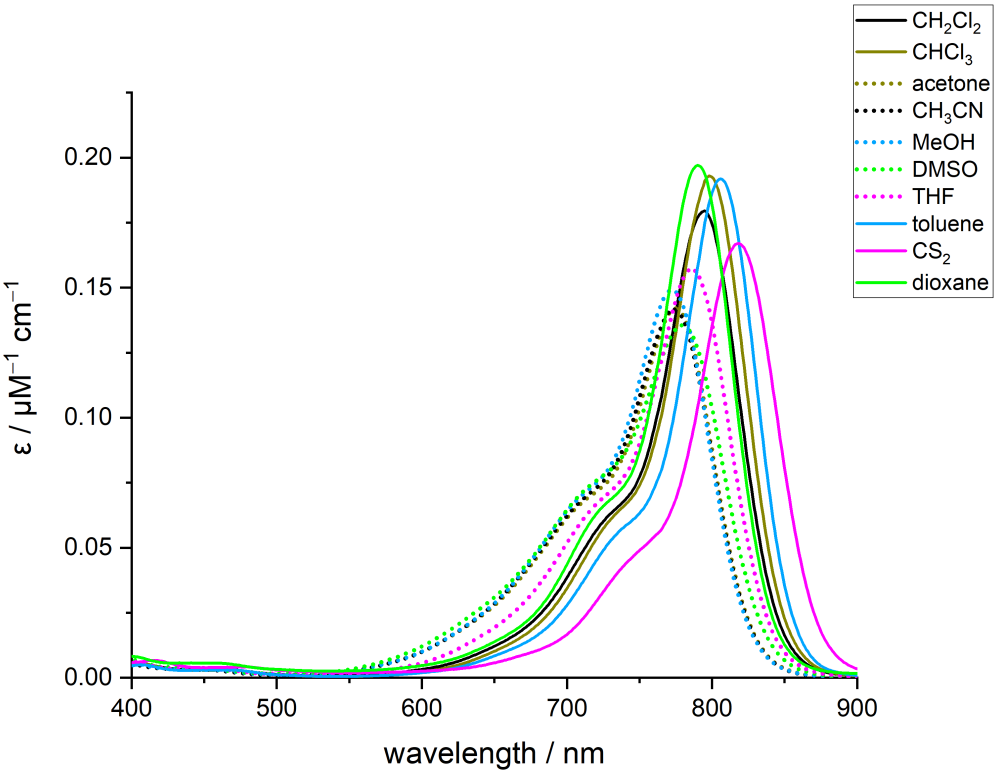

Figure S9. UV-vis-NIR absorption spectra of compounds **Cy7·B(C$_6$F$_5$)$_4$** recorded in a range of solvents: dichloromethane, chloroform, acetone, acetonitrile, methanol, DMSO, THF and toluene.

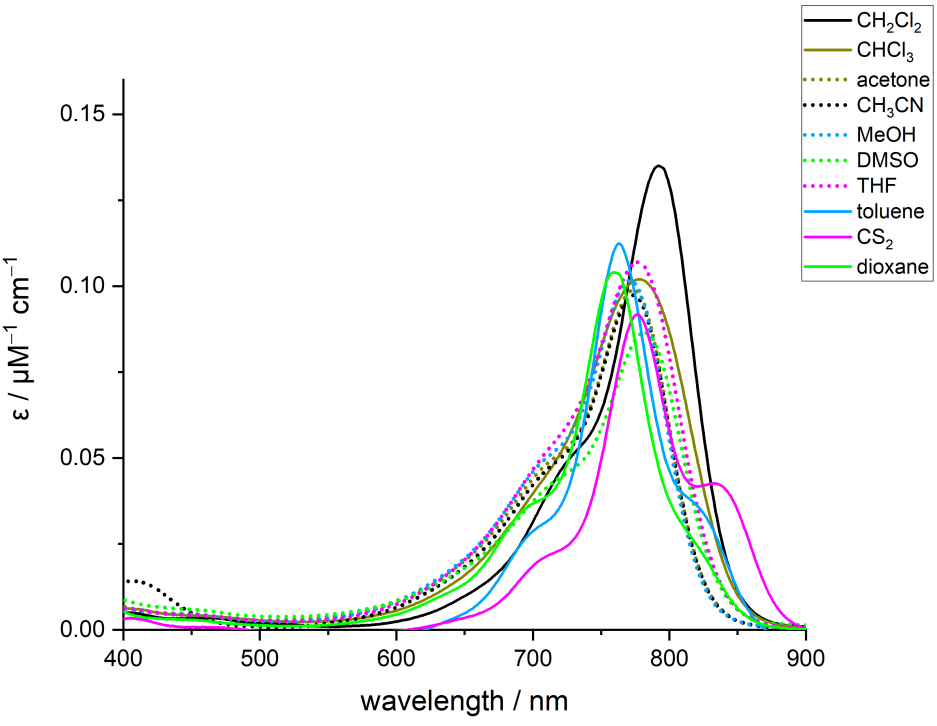

Figure S10. UV-vis-NIR absorption spectra of compounds **Cy7·PF$_6$** recorded in a range of solvents: dichloromethane, chloroform, acetone, acetonitrile, methanol, DMSO, THF and toluene.

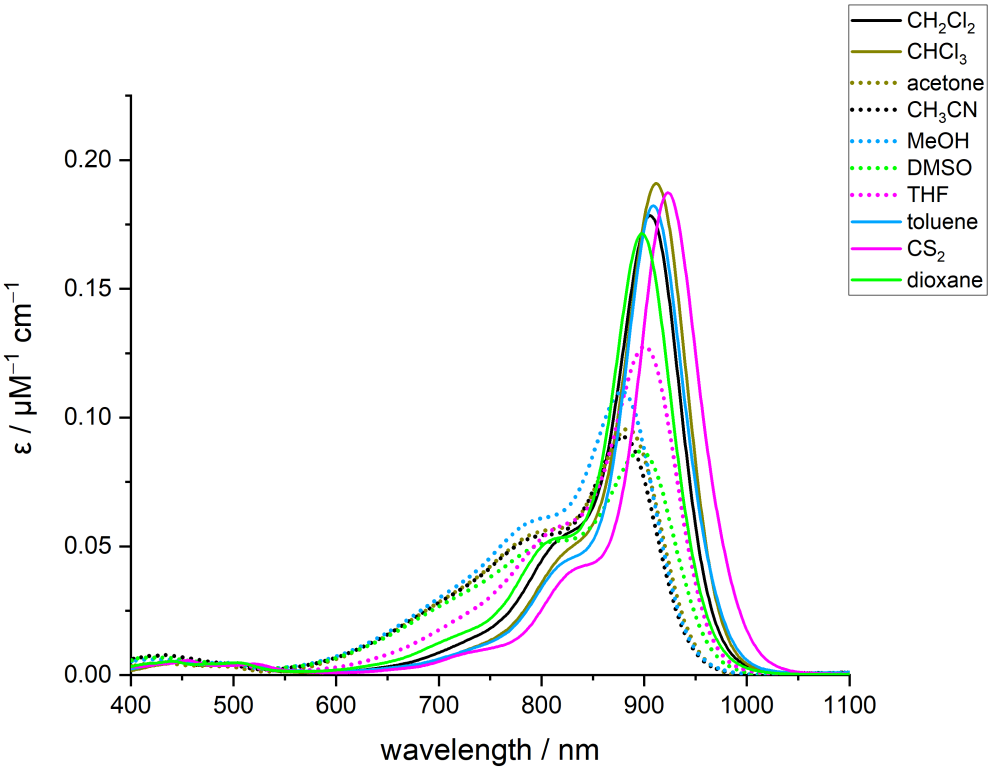

Figure S11. UV-vis-NIR absorption spectra of compounds **Cy9·B(C$_6$F$_5$)$_4$** recorded in a range of solvents: dichloromethane, chloroform, acetone, acetonitrile, methanol, DMSO, THF and toluene.

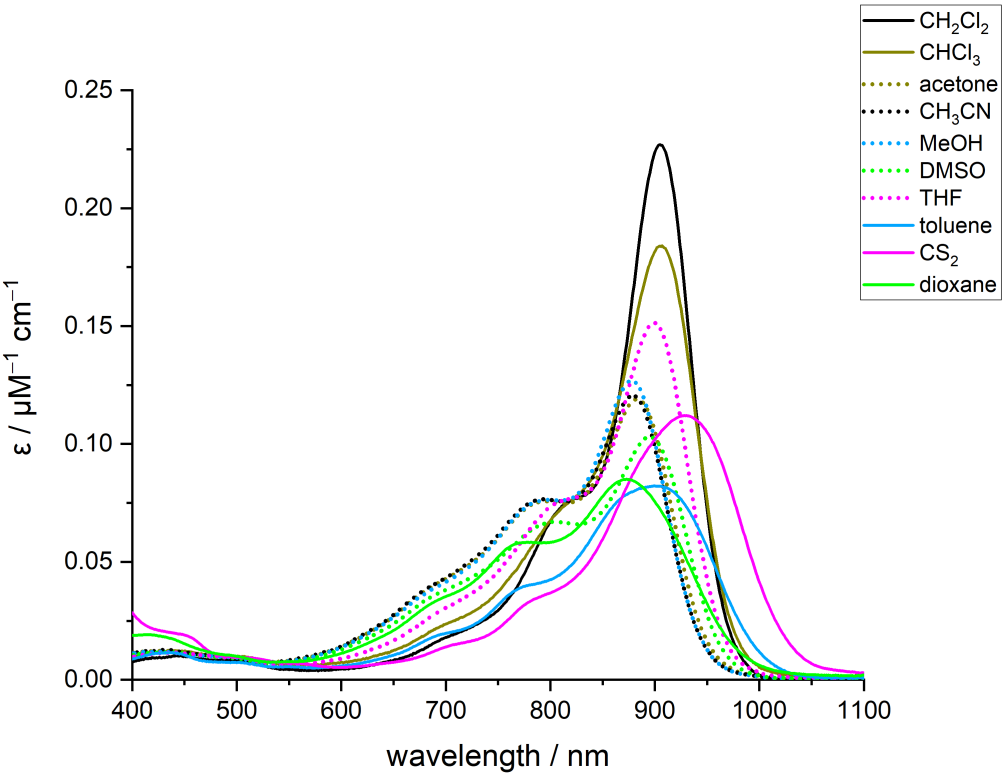

Figure S12. UV-vis-NIR absorption spectra of compounds **Cy9·PF$_6$** recorded in a range of solvents: dichloromethane, chloroform, acetone, acetonitrile, methanol, DMSO, THF and toluene.

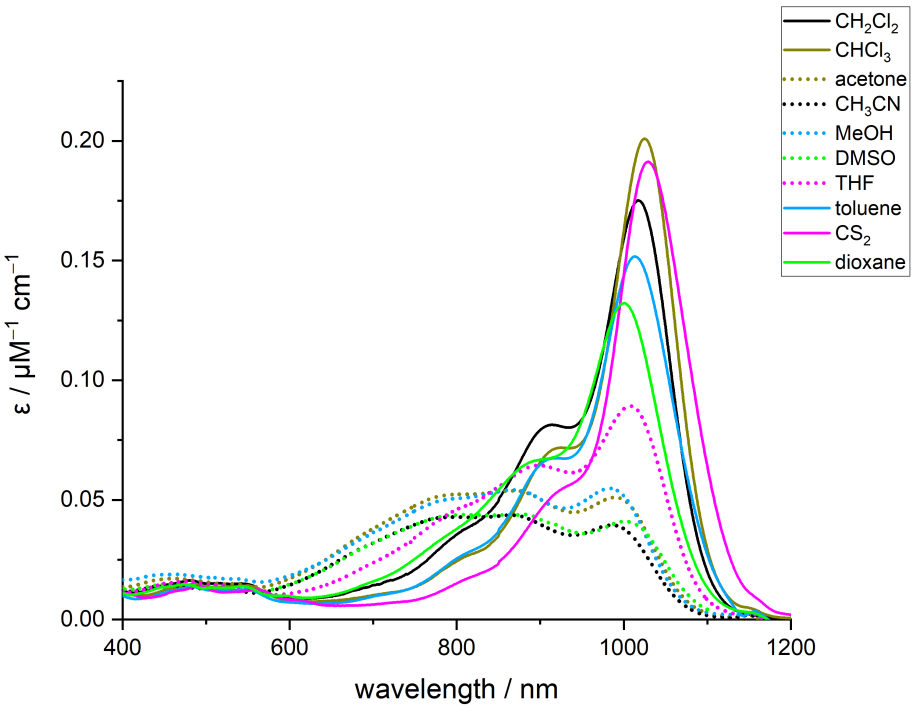

Figure S13. UV-vis-NIR absorption spectra of compounds **Cy11·B(C_6F_5)$_4$** recorded in a range of solvents: dichloromethane, chloroform, acetone, acetonitrile, methanol, DMSO, THF and toluene.

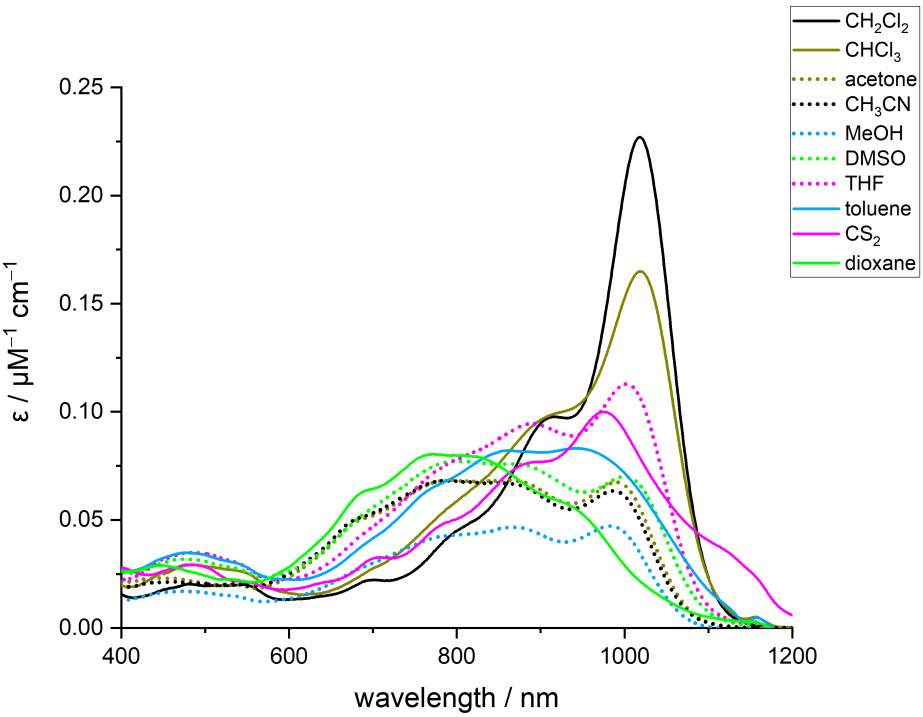

Figure S14. UV-vis-NIR absorption spectra of compounds **Cy11·PF_6** recorded in a range of solvents: dichloromethane, chloroform, acetone, acetonitrile, methanol, DMSO, THF and toluene.

Section 3. X-Ray Crystallography

Methods: Single crystal X-ray diffraction were collected on a Rigaku Oxford Diffraction SuperNova diffractometer or at beamline I19, Diamond Light Source.[8] The CrysAlisPro software was used for data collection and integration. Crystallographic data have been deposited with the Cambridge Crystallographic Data Centre (CCDC 2074549-59) and can be obtained via www.ccdc.cam.ac.uk/data_request/cif.

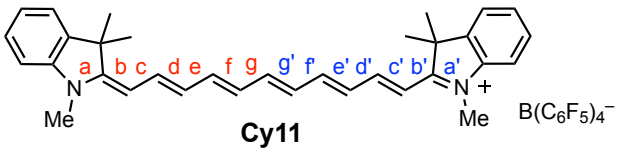

Cy11

Table 3. Bond lengths and bond length alternation from this work for **Cy3** and **Cy5**.

cyanine	**Cy3** (a)	**Cy3** (b)			**Cy5**	**Cy5** (c)	**Cy5** (c)
X^-	$B(C_6F_5)_4^-$	PF_6^-			$B(C_6F_5)_4^-$	PF_6^-	I^-
R factor	4.89%	4.92%			4.44%	4.69%	3.50%
mean sd in bond lengths	±0.004	±0.005			±0.005	±0.003	±0.002
a / Å	1.353	1.347	1.348	1.361	1.352	1.351	1.350
a′ / Å	1.308	1.345	1.347	1.344	1.342	1.351	1.350
a – *a′* / Å	0.045	0.002	0.001	0.017	0.010	0.000	0.000
b / Å	1.381	1.394	1.394	1.390	1.383	1.385	1.390
b′ / Å	1.352	1.383	1.395	1.390	1.390	1.385	1.390
b – *b′* / Å	0.029	0.11	–0.001	0.000	–0.007	0.000	0.000
c / Å	1.383	1.379	1.386	1.395	1.388	1.393	1.389
c′ / Å	1.379	1.394	1.385	1.393	1.378	1.393	1.389
c – *c′* / Å	0.004	–0.05	0.001	0.002	0.010	0.000	0.000
d / Å					1.383	1.389	1.391
d′ / Å					1.382	1.389	1.391
d – *d′* / Å					0.001	0.000	0.000
mean BLA / Å	0.007	0.005	0.001	0.006	0.007	0.00	0.00
BLA sd / Å	±0.037	±0.007	±0.000	±0.009	±0.005	–	–

(a) structure has substantial disorder, leading to uncertainty in the bond lengths. (b) three molecules in the asymmetric unit. (c) molecule has crystallographic symmetry.

Table 4. Bond lengths and bond length alternation from this work for **Cy7**, **Cy9** and **Cy11**.

cyanine	**Cy7**	**Cy7**	**Cy7**	**Cy9**	**Cy9**	**Cy11**
X^-	$B(C_6F_5)_4^-$	PF_6^-	Br^-	$B(C_6F_5)_4^-$	PF_6^-	$B(C_6F_5)_4^-$
R factor	4.29%	6.88%	7.42%	6.52%	9.02%	6.80%
mean sd in bond lengths	±0.003	±0.011	±0.002	±0.006	±0.004	±0.009
a / Å	1.348(2)	1.363	1.3683(15)	1.351(5)	1.354(3)	1.364(8)
a′ / Å	1.349(2)	1.354	1.3428(16)	1.345(4)	1.343(3)	1.346(7)
a – *a′* / Å	–0.001	0.009	0.0255	0.006	0.011	0.018
b / Å	1.388(3)	1.396	1.3701(17)	1.382(5)	1.366(4)	1.373(9)
b′ / Å	1.383(3)	1.394	1.3978(16)	1.387(5)	1.385(3)	1.386(9)
b – *b′* / Å	0.005	0.002	–0.0277	–0.005	–0.019	–0.013
c / Å	1.391(3)	1.394	1.4076(17)	1.392(5)	1.399(3)	1.400(9)
c′ / Å	1.392(3)	1.379	1.3843(18)	1.388(5)	1.368(3)	1.377(9)
c – *c′* / Å	–0.001	0.015	0.0233	–0.004	0.031	0.023
d / Å	1.391(3)	1.375	1.3777(18)	1.386(6)	1.356(4)	1.371(9)
d′ / Å	1.386(3)	1.424	1.3922(18)	1.383(5)	1.392(3)	1.378(9)
d – *d′* / Å	0.005	–0.049	–0.0145	0.003	–0.036	–0.007
e / Å	1.388(3)	1.391	1.4033(17)	1.386(5)	1.395(3)	1.407(9)
e′ / Å	1.387(3)	1.368	1.3810(18)	1.394(5)	1.371(4)	1.378(9)
e – *e′* / Å	0.001	0.023	0.0223	–0.008	0.024	0.029
f / Å				1.382(6)	1.360(4)	1.378(9)
f′ / Å				1.383(5)	1.391(3)	1.393(9)
f – *f′* / Å				–0.001	–0.031	–0.015
g / Å						1.397(9)
g′ / Å						1.376(9)
g – *g′* / Å						0.021
mean BLA / Å	0.002	0.019	0.023	0.001	0.025	0.018
BLA sd / Å	±0.003	±0.019	±0.005	±0.005	±0.009	±0.007

Table 5. Bond lengths and bond length alternation in cyanine structures from CCDC.[9-19]

CCDC no.	619814	619809	619813	1139377	2003730			661299			
X^-	BPh_4^-	BPh_4^-	ClO_4^-	I^-	$Bi_2I_9^{3-}$			PF_6^-			
Reference	9	10	11	12	13			14			
R (%)	5.21%	5.56%	5.78%	8.40%	6.70%			17.52%			
a / Å	1.327	1.335	1.322	1.352	1.371	1.411	1.369	1.333	1.410	1.416	1.380
a′ / Å	1.319	1.308	1.321	1.339	1.341	1.383	1.368	1.269	1.301	1.338	1.324
a – *a′* / Å	0.008	0.027	0.001	0.013	0.030	0.028	0.001	0.064	0.109	0.078	0.056
b / Å	1.361	1.339	1.368	1.375	1.372	1.366	1.298	1.390	1.376	1.415	1.388
b′ / Å	1.337	1.363	1.385	1.409	1.410	1.359	1.341	1.424	1.430	1.382	1.455
b – *b′* / Å	0.024	–0.024	–0.017	–0.034	–0.038	0.007	–0.043	–0.034	–0.054	0.033	–0.067
c / Å	1.374	1.375	1.387	1.431	1.349	1.406	1.340	1.293	1.415	1.307	1.433
c′ / Å	1.393	1.355	1.382	1.353	1.319	1.330	1.357	1.349	1.394	1.381	1.394
c – *c′* / Å	–0.019	0.020	0.005	0.078	0.030	0.076	–0.017	–0.056	0.021	–0.074	0.039
d / Å	1.363	1.349	1.376	1.413	1.361	1.325	1.405	1.455	1.428	1.344	1.414
d′ / Å	1.361	1.342	1.386	1.426	1.387	1.419	1.391	1.396	1.321	1.401	1.338
d – *d′* / Å	0.002	0.007	–0.010	–0.013	–0.026	–0.094	0.014	0.059	0.107	–0.057	0.076
e / Å	1.354	1.348	1.388	1.405	1.355	1.395	1.400	1.334	1.436	1.457	1.318
e′ / Å	1.376	1.351	1.373	1.348	1.376	1.440	1.402	1.415	1.461	1.404	1.356
e – *e′* / Å	–0.022	–0.003	0.015	0.057	–0.021	–0.045	–0.002	–0.081	–0.025	0.053	–0.038
mean BLA	0.012	0.012	0.010	0.039	0.021	0.029	0.002	0.020	0.010	0.016	0.010
BLA sd / Å	±0.014	±0.016	±0.007	±0.028	±0.024	±0.057	±0.024	±0.064	±0.082	±0.066	±0.063

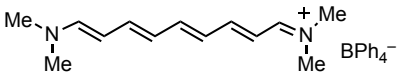

CCDC 619809 and 619814

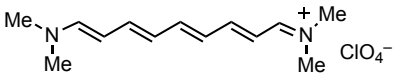

CCDC 619813

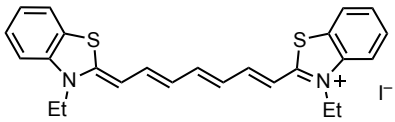

CCDC 1139377

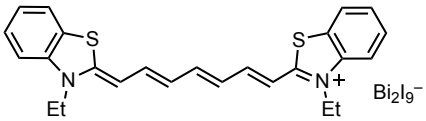

CCDC 2003730

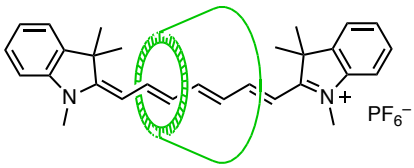

CCDC 661299

Table 5 (continued). Bond lengths and bond length alternation in cyanine structures from CCDC.

CCDC no.	600891	600892	610543	226535	717753	620268	647547	634859	668666	681120
X^-	BF_4^-	BF_4^-	BF_4^-	BF_4^-	TRISPHAT	Br	I	PF_6^-	SbF_6^-	$B(C_6F_5)_4^-$
Reference	15	15	16	16	17	18	18	18	18	18
R factor	4.61%	5.20%	3.82%	4.62%	5.00%	7.32%	6.11%	4.99%	5.80%	6.38%
a / Å	1.338	1.340	1.346	1.351	1.363	1.409	1.384	1.358	1.371	1.394
a′ / Å	1.330	1.330	1.338	1.339	1.346	1.336	1.341	1.347	1.349	1.355
a – *a′* / Å	0.008	0.010	0.008	0.012	0.017	0.073	0.043	0.011	0.022	0.039
b / Å	1.395	1.404	1.398	1.397	1.375	1.347	1.367	1.368	1.385	1.393
b′ / Å	1.411	1.412	1.409	1.407	1.390	1.413	1.394	1.381	1.403	1.384
b – *b′* / Å	–0.016	–0.008	–0.011	–0.010	–0.015	–0.066	–0.027	–0.013	–0.018	0.009
c / Å	1.398	1.389	1.397	1.397	1.398	1.424	1.408	1.397	1.397	1.364
c′ / Å	1.371	1.386	1.383	1.379	1.391	1.360	1.394	1.374	1.378	1.387
c – *c′* / Å	0.027	0.003	0.014	0.018	0.007	0.064	0.014	0.023	0.019	–0.023
d / Å	1.388	1.392	1.387	1.393	1.386	1.359	1.372	1.387	1.395	1.403
d′ / Å	1.412	1.404	1.411	1.403	1.390	1.406	1.399	1.394	1.406	1.392
d – *d′* / Å	–0.024	–0.012	–0.024	–0.010	–0.004	–0.047	–0.027	–0.007	–0.011	0.011
e / Å	1.415	1.408	1.410	1.410	1.407	1.424	1.439	1.410	1.423	1.394
e′ / Å	1.391	1.396	1.399	1.399	1.403	1.371	1.395	1.381	1.385	1.400
e – *e′* / Å	0.024	0.012	0.011	0.011	0.004	0.053	0.044	0.029	0.038	–0.006
mean BLA	0.020	0.009	0.014	0.012	0.009	0.061	0.031	0.017	0.022	0.002
BLA sd / Å	±0.008	±0.004	±0.006	±0.003	±0.006	±0.010	±0.013	±0.009	±0.010	±0.024

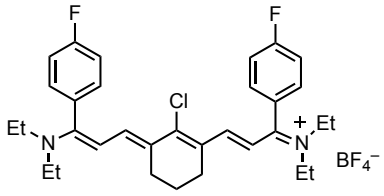

CCDC 600891

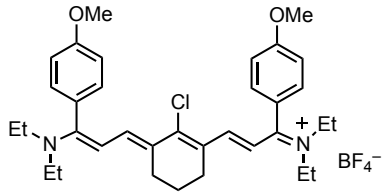

CCDC 610543

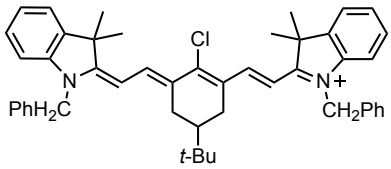

CCDC 717753, 620268, 647547, 634859, 668666, 681120

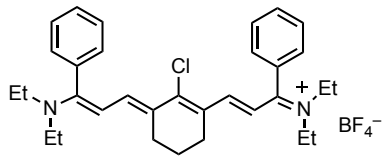

CCDC 600892

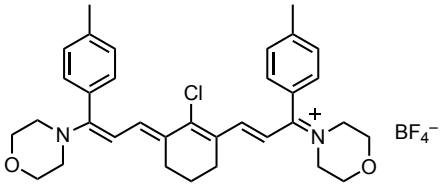

CCDC 226535

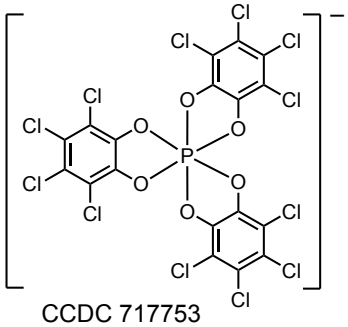

CCDC 717753

Table 5 (continued). Bond lengths and bond length alternation in cyanine structures from CCDC.

CCDC no.	989957				989956
X^-	PF_6^-				TRISPHAT
Reference	19				19
R factor	5.59				6.43
a / Å	1.369	1.371	1.372	1.370	1.356
a′ / Å	1.343	1.344	1.334	1.344	1.344
a – *a′* / Å	0.026	0.027	0.038	0.026	0.012
b / Å	1.378	1.362	1.391	1.364	1.388
b′ / Å	1.414	1.404	1.408	1.420	1.391
b – *b′* / Å	–0.036	–0.042	–0.017	–0.056	–0.003
c / Å	1.412	1.395	1.421	1.411	1.389
c′ / Å	1.378	1.375	1.366	1.372	1.389
c – *c′* / Å	0.034	0.020	0.055	0.039	0.000
d / Å	1.381	1.371	1.362	1.365	1.400
d′ / Å	1.395	1.406	1.398	1.432	1.394
d – *d′* / Å	–0.014	–0.035	–0.036	–0.067	0.006
e / Å	1.393	1.427	1.408	1.444	1.401
e′ / Å	1.425	1.382	1.395	1.366	1.406
e – *e′* / Å	–0.032	0.045	0.013	0.078	–0.005
mean BLA	0.015	0.034	0.032	0.053	0.001
BLA sd / Å	0.028	0.010	0.017	0.021	0.007

Section 4. DFT Simulations and Transport Calculations

4.1. Computational Methodology. DFT geometry optimizations of cyanine dyes were first performed using Gaussian 16/A.03 with the BHandHLYP/6-311G* functional/basis set.[20-22] The minimized structures were subjected to frequency calculations, revealing no imaginary frequencies. TD-DFT calculations were conducted for the first 20 excited states employing Gaussian16/A.03 with the BHandHLYP/6-311G* functional/basis set.[20,21] The transition states for moving the positive charge between the ends of the low-symmetry cyanine dyes were found by optimizing the structures with imposed C_2 symmetry. In most cases, this procedure gave the transition state directly, as shown by the presence of one imaginary frequency corresponding to the interconversion of long and short bonds in the cyanine chain. But in some cases, this approach yielded a structure with two imaginary frequencies. In these cases, we used intrinsic reaction coordinate (IRC) calculations, with the local quadratic approximation (LQA) method, and a stepsize of 0.05 Bohr, as implemented in the Gaussian, to locate the transition state geometry. Frequency calculations were then performed on the refined geometries to confirm they were transition states with one imaginary frequency.

4.2. Calculated Bond Length Alternation

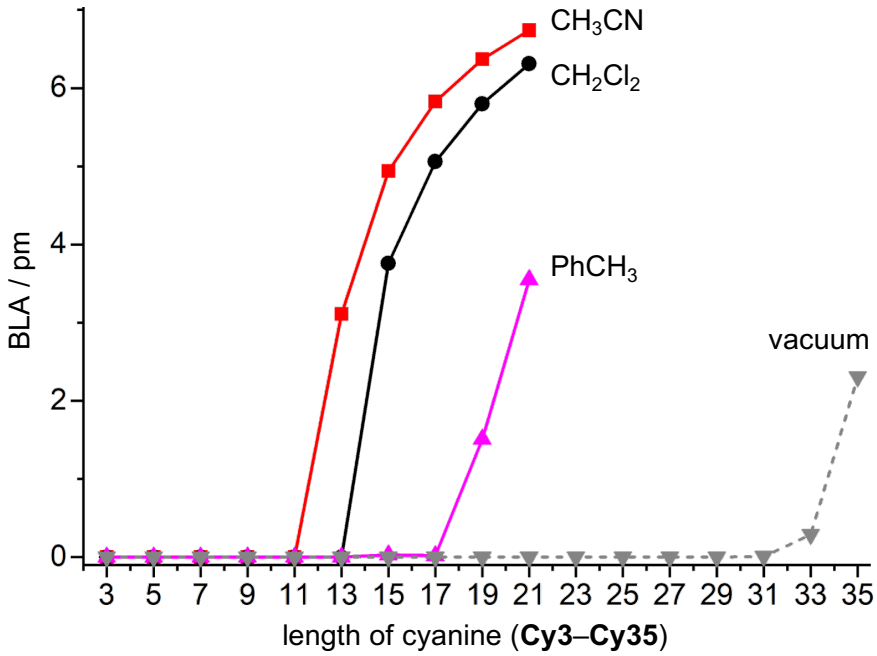

Figure S15. Calculated bond length alternation of **Cy3**$^+$ to **Cy35**$^+$ in MeCN, CH_2Cl_2, PhMe and vacuum.

Table 6. Calculated bond lengths and bond-length alternation of cyanine dyes in CH_3CN.

cyanine	$Cy3^+$	$Cy5^+$	$Cy7^+$	$Cy9^+$	$Cy11^+$	$Cy13^+$	$Cy15^+$	$Cy17^+$	$Cy19^+$	$Cy21^+$
a / Å	1.338	1.341	1.344	1.347	1.349	1.364	1.372	1.376	1.378	1.379
a′ / Å	1.338	1.341	1.344	1.347	1.349	1.338	1.332	1.329	1.328	1.327
a – *a′* / Å	0.000	0.000	0.000	0.000	0.000	0.026	0.040	0.047	0.050	0.052
b / Å	1.386	1.382	1.380	1.377	1.375	1.362	1.356	1.353	1.352	1.351
b′ / Å	1.386	1.382	1.380	1.377	1.375	1.387	1.394	1.397	1.398	1.399
b – *b′* / Å	0.000	0.000	0.000	0.000	0.000	–0.025	–0.038	–0.044	–0.046	–0.048
c / Å	1.386	1.388	1.391	1.394	1.397	1.415	1.424	1.428	1.431	1.432
c′ / Å	1.386	1.388	1.391	1.394	1.397	1.384	1.376	1.373	1.371	1.370
c – *c′* / Å	0.000	0.000	0.000	0.000	0.000	0.031	0.048	0.055	0.060	0.062
d / Å		1.383	1.381	1.378	1.375	1.360	1.353	1.350	1.349	1.348
d′ / Å		1.383	1.381	1.378	1.375	1.389	1.397	1.401	1.403	1.404
d – *d′* / Å		0.000	0.000	0.000	0.000	–0.029	–0.044	–0.051	–0.054	–0.056
e / Å			1.386	1.389	1.392	1.412	1.422	1.427	1.430	1.431
e′ / Å			1.386	1.389	1.392	1.378	1.370	1.367	1.364	1.363
e – *e′* / Å			0.000	0.000	0.000	0.034	0.052	0.060	0.066	0.068
f / Å				1.383	1.380	1.362	1.354	1.350	1.348	1.347
f′ / Å				1.383	1.380	1.396	1.405	1.409	1.411	1.412
f – *f′* / Å				0.000	0.000	–0.034	–0.051	–0.059	–0.063	–0.065
g / Å					1.386	1.408	1.420	1.426	1.429	1.431
g′ / Å					1.386	1.372	1.363	1.360	1.358	1.357
g – *g′* / Å					0.000	0.036	0.057	0.066	0.071	0.074
h / Å						1.366	1.356	1.351	1.348	1.347
h′ / Å						1.402	1.412	1.416	1.418	1.419
h – *h′* / Å						–0.036	–0.056	–0.065	–0.070	–0.072
i / Å							1.417	1.424	1.428	1.430
i′ / Å							1.359	1.356	1.354	1.353
i – *i′* / Å							0.058	0.068	0.074	0.077
j / Å								1.353	1.349	1.348
j′ / Å								1.421	1.423	1.424
j – *j′* / Å								–0.068	–0.074	–0.076
k / Å									1.426	1.429
k′ / Å									1.351	1.350
k – *k′* / Å									0.075	0.079
l / Å										1.348
l′ / Å										1.427
l – *l′* / Å										–0.079
mean BLA / Å	0.000	0.000	0.000	0.000	0.000	0.031	0.049	0.058	0.064	0.067
BLA sd / Å	–	–	–	–	–	±0.004	±0.007	±0.009	±0.010	±0.011

Table 7. Calculated bond lengths and bond-length alternation of **Cy15**$^{+}$ in CH_3CN, CH_2Cl_2, toluene and vacuum.

environment	CH_3CN	CH_2Cl_2	toluene	vacuum
a / Å	1.372	1.368	1.353	1.352
a′ / Å	1.332	1.337	1.353	1.352
a – *a′* / Å	0.040	0.031	0.000	0.000
b / Å	1.356	1.359	1.371	1.372
b′ / Å	1.394	1.388	1.372	1.372
b – *b′* / Å	–0.038	–0.029	–0.001	0.000
c / Å	1.424	1.420	1.402	1.401
c′ / Å	1.376	1.383	1.402	1.401
c – *c′* / Å	0.048	0.037	0.000	0.000
d / Å	1.353	1.356	1.370	1.370
d′ / Å	1.397	1.390	1.371	1.370
d – *d′* / Å	–0.044	–0.034	–0.001	0.000
e / Å	1.422	1.417	1.398	1.397
e′ / Å	1.370	1.377	1.397	1.397
e – *e′* / Å	0.052	0.040	0.001	0.000
f / Å	1.354	1.358	1.374	1.374
f′ / Å	1.405	1.396	1.375	1.374
f – *f′* / Å	–0.051	–0.038	–0.001	0.000
g / Å	1.420	1.414	1.392	1.391
g′ / Å	1.363	1.370	1.392	1.391
g – *g′* / Å	0.057	0.044	0.000	0.000
h / Å	1.356	1.361	1.380	1.380
h′ / Å	1.412	1.403	1.380	1.380
h – *h′* / Å	–0.056	–0.042	0.000	0.000
i / Å	1.417	1.409	1.386	1.385
i′ / Å	1.359	1.365	1.386	1.385
i – *i′* / Å	0.058	0.044	0.000	0.000
mean BLA / Å	0.049	0.038	0.000	0.000
BLA sd / Å	±0.007	±0.005	±0.001	–

4.3. Calculated Charge Distributions.

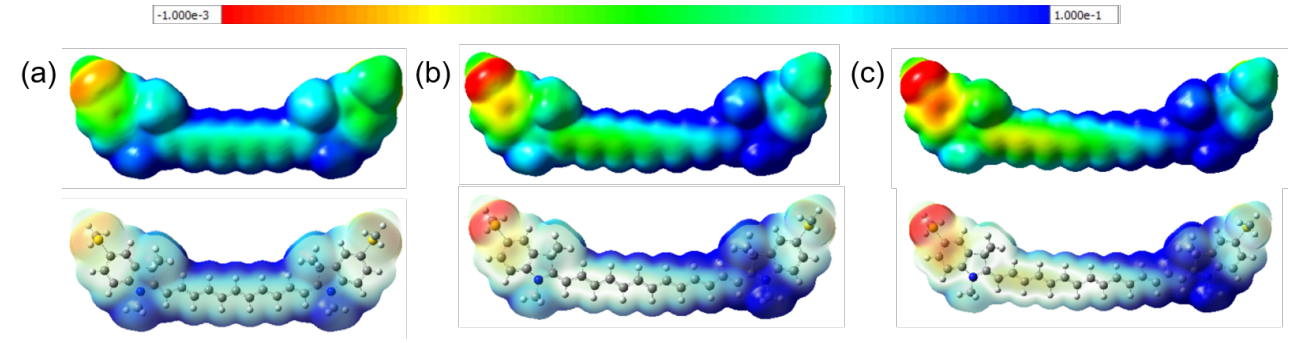

Figure S16. Electrostatic potential surface of (a) **Cy11**$^+$, (b) **Cy13**$^+$ and (c) **Cy15**$^+$ in CH_3CN.

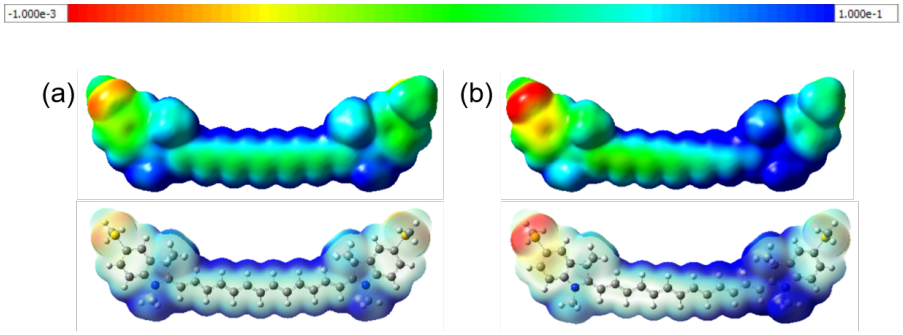

Figure S17. Electrostatic potential surface of **Cy13**$^+$ in (a) toluene and (b) CH_3CN.

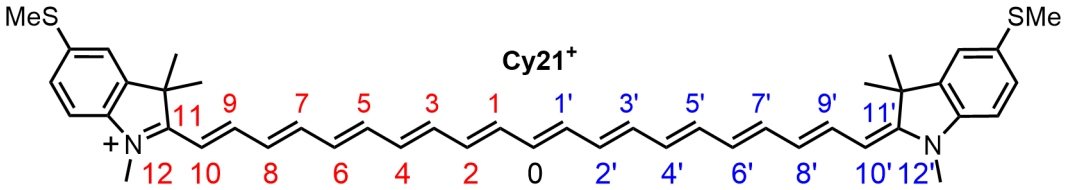

Table 8. Mulliken charge distribution of cyanine molecular wires in CH_3CN.

atom	$Cy3^+$	$Cy5^+$	$Cy7^+$	$Cy9^+$	$Cy11^+$	$Cy13^+$	$Cy15^+$	$Cy17^+$	$Cy19^+$	$Cy21^+$
0	0.1251	–0.0118	0.0659	–0.0215	0.0753	–0.0165	0.0558	–0.0104	0.0374	–0.0066
1	–0.1430	0.1003	–0.0135	0.0699	–0.0202	0.0628	–0.0159	0.0397	–0.0104	0.0261
1'	–0.1430	0.1003	–0.0135	0.0698	–0.0202	0.0726	–0.0111	0.0525	–0.0066	0.0362
1 – 1'	0.0000	0.0000	0.0000	0.0001	0.0000	–0.0098	–0.0048	–0.0128	–0.0038	–0.0101
2	0.5102	–0.1450	0.0969	–0.0131	0.0665	–0.0226	0.0438	–0.0160	0.0275	–0.0104
2'	0.5102	–0.1450	0.0969	–0.0132	0.0665	–0.0146	0.0698	–0.0071	0.0508	–0.0041
2 – 2'	0.0000	0.0000	0.0000	0.0001	0.0000	–0.008	–0.0260	–0.0089	–0.0233	–0.0063
3	–0.5241	0.5012	–0.1449	0.0915	–0.0136	0.0455	–0.0238	0.0298	–0.0160	0.0190
3'	–0.5241	0.5012	–0.1449	0.0914	–0.0137	0.0735	–0.0092	0.0682	–0.0045	0.0500
3 – 3'	0.0000	0.0000	0.0000	0.0001	0.0001	–0.028	–0.0146	–0.0384	–0.0115	–0.031
4		–0.5243	0.4957	–0.1462	0.0869	–0.0209	0.0264	–0.0453	0.0201	–0.0161
4'		–0.5243	0.4957	–0.1463	0.0869	–0.0046	0.0761	–0.0058	0.0673	–0.0029
4 – 4'		0.0000	0.0000	0.0001	0.0000	–0.029	–0.0497	–0.0395	–0.0472	–0.0132
5			–0.5260	0.4907	–0.1480	0.0588	–0.0242	0.0350	–0.0242	0.0137
5'			–0.5260	0.4906	–0.1480	0.1030	0.0019	0.0767	–0.0036	0.0670
5 – 5'			0.0000	0.0001	0.0000	–0.0442	–0.0261	–0.060	–0.066	–0.068
6				–0.5278	0.4863	–0.1604	0.0402	–0.0464	0.0072	–0.0243
6'				–0.5279	0.4862	–0.1333	0.1114	0.0054	0.0769	–0.0025
6 – 6'				0.0001	0.0001	–0.0271	–0.051	–0.0518	–0.0697	–0.0218
7					–0.5297	0.4599	–0.1648	0.0447	–0.0256	0.0025
7'					–0.9297	0.5044	–0.1232	0.1144	0.0075	0.0774
7 – 7'					0.0000	–0.0445	–0.0416	–0.066	–0.071	–0.074
8						–0.5407	0.4447	–0.1685	0.0244	–0.0259
8'						–0.5201	0.5142	–0.1182	0.1160	0.0084
8 – 8'						–0.0206	–0.0695	–0.0503	–0.0916	–0.0343
9							–0.5457	0.4542	–0.1666	0.0208
9'							–0.5142	0.5183	–0.1155	0.1171
9 – 9'							–0.0315	–0.0641	–0.0511	–0.077
10								–0.5478	0.4332	–0.1668
10'								–0.5116	0.5204	–0.1138
10 – 10'								–0.0362	–0.0872	–0.053
11									–0.5488	0.4307
11'									–0.5102	0.5215
11 – 11'									–0.0386	–0.0908
12										–0.5494
12'										–0.5094
12 – 12'										–0.0400

Table 9. Mulliken charge distribution of **Cy15**$^+$ in CH_3CN, CH_2Cl_2, toluene and vacuum.

Cy15$^+$	**CH_3CN**	**CH_2Cl_2**	**toluene**	**vacuum**
0	0.0558	0.0612	0.06386	0.05855
1	–0.0159	–0.0145	–0.0082	–0.0040
1'	–0.0111	–0.0109	–0.0081	–0.0040
1 – 1'	–0.0048	–0.0036	–0.0001	0
2	0.0438	0.0516	0.0634	0.0573
2'	0.0698	0.0716	0.0635	0.0573
2 – 2'	–0.0260	–0.0200	–0.0001	0
3	–0.0238	–0.0215	–0.0123	–0.0064
3'	–0.0092	–0.0108	–0.0123	–0.0064
3 – 3'	–0.0146	–0.0107	0	0
4	0.0264	0.0346	0.0521	0.0449
4'	0.0761	0.0724	0.0526	0.0449
4 – 4'	–0.0497	–0.0378	–0.0005	0
5	–0.0242	–0.0207	–0.0079	–0.0013
5'	0.0019	–0.0019	–0.0082	–0.0013
5 – 5'	–0.0261	–0.0188	0.0003	0
6	0.0402	0.0489	0.0732	0.0687
6'	0.1114	0.1026	0.0737	0.0687
6 – 6'	–0.0712	–0.0537	–0.0005	0
7	–0.1648	–0.1624	–0.1534	–0.1551
7'	–0.1232	–0.1334	–0.1532	–0.1551
7 – 7'	–0.0416	–0.0290	–0.0002	0

4.4. Calculated Absorption Spectra.

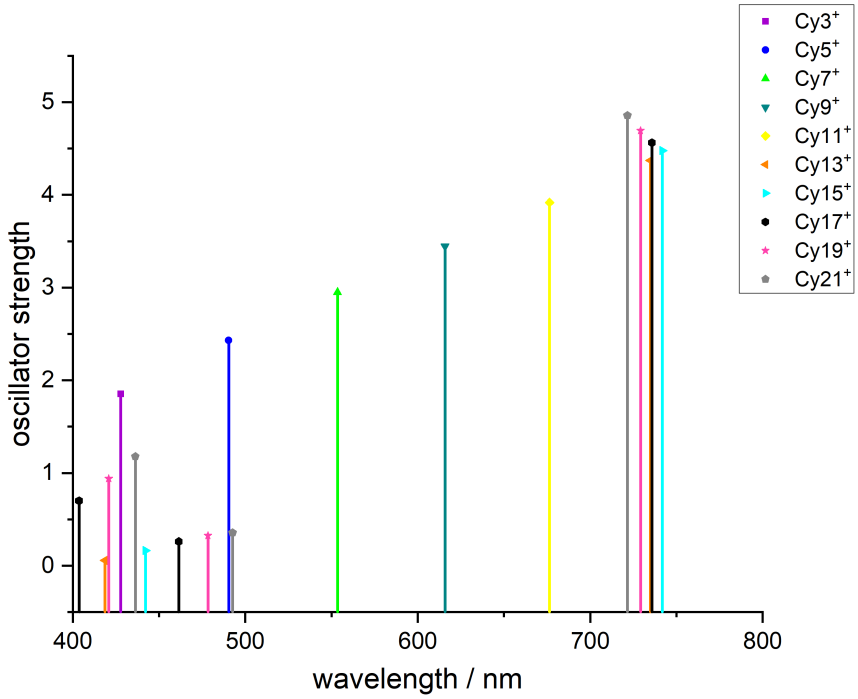

Figure S18. TD-DFT calculated absorption wavelength of cyanine dye molecular wires and oscillator strengths in CH_2Cl_2.

Table 10. TD-DFT calculated absorption wavelength of first excited state, transition energies and oscillator strengths of cyanines in CH_2Cl_2.

cyanine	λ_{max} (nm)	E_{max} (eV)	f
Cy3$^+$	428	2.898	1.85
Cy5$^+$	490	2.529	2.43
Cy7$^+$	553	2.240	2.95
Cy9$^+$	616	2.014	3.44
Cy11$^+$	676	1.833	3.92
Cy13$^+$	735	1.687	4.37
Cy15$^+$	742	1.672	4.48
Cy17$^+$	736	1.685	4.56
Cy19$^+$	729	1.700	4.69
Cy21$^+$	722	1.718	4.85

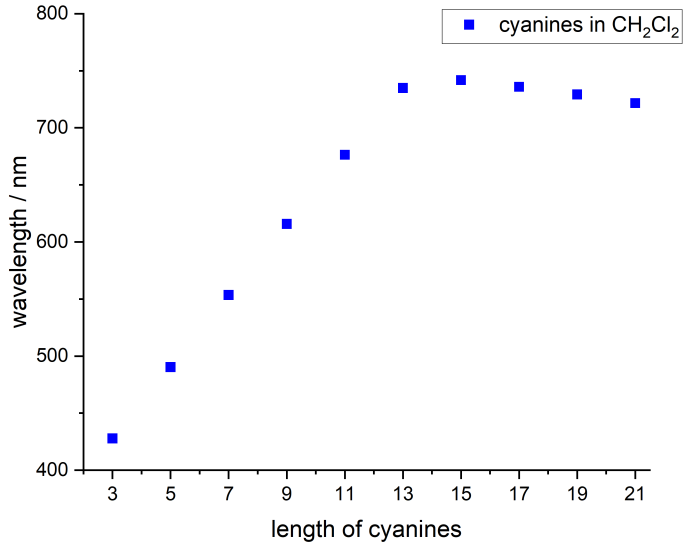

Figure S19. TD-DFT calculated absorption wavelength of cyanine dye molecular wires in CH_2Cl_2.

4.5. Calculated Activation Energies for Bond-Shift Tautomerism

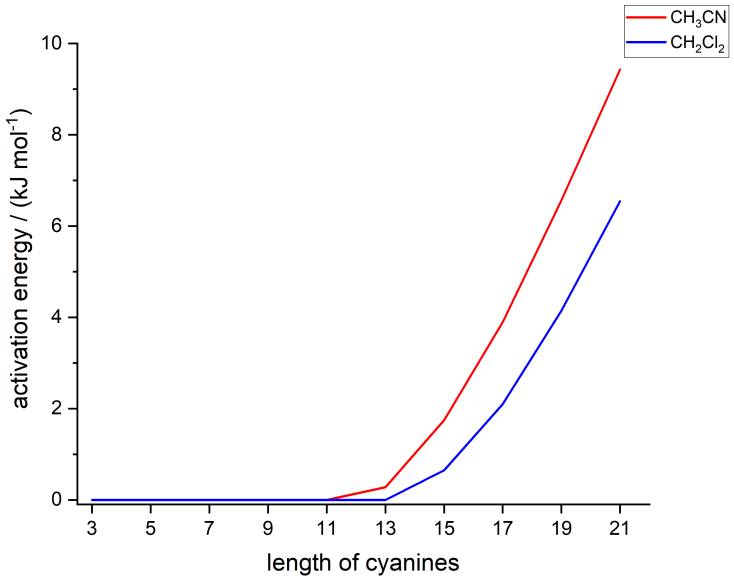

Figure S20. Calculated activation energy of for bond-shift tautomerism to relocate the positive charge in **Cy3$^+$–Cy21$^+$**, in acetonitrile and dichloromethane, respectively. Both results are from DFT calculations using intrinsic reaction coordinate (IRC) calculations with the local quadratic approximation (LQA) method and a stepsize of 0.05 Bohr, using Gaussian 16/A.03 with BHandHLYP/6-311G*. The transition states were confirmed by single imaginary frequencies.

Table 11. Calculated activation energy of the bond-shift tautomerization in cyanine dye molecular wires in CH_3CN and CH_2Cl_2.

cyanine	$\Delta E^{\ddagger}(CH_3CN)$ / kJ mol^{-1}	$\Delta E^{\ddagger}(CH_2Cl_2)$ / kJ mol^{-1}
Cy3$^+$	0.00	0.00
Cy5$^+$	0.00	0.00
Cy7$^+$	0.00	0.00
Cy9$^+$	0.00	0.00
Cy11$^+$	0.00	0.00
Cy13$^+$	0.28	0.00
Cy15$^+$	1.75	0.65
Cy17$^+$	3.89	2.10
Cy19$^+$	6.56	4.14
Cy21$^+$	9.43	6.54

4.6. Charge Transport Calculations

We used density functional theory to find an optimized structure of the cyanine dye molecular wires in the gas phase and between gold electrodes. The optimized geometry, ground state Hamiltonian and overlap matrix element of each structure was self-consistently obtained using the SIESTA[23] implementation of density functional theory (DFT). SIESTA employs norm-conserving pseudopotentials to account for the core electrons, and linear combinations of atomic orbitals to construct the valence states. The generalized gradient approximation (GGA) of the exchange and correlation functional is used with the Perdew-Burke-Ernzerhof parameterization (PBE) a double-ζ polarized (DZP) basis set, a real-space grid defined with an equivalent energy cut-off of 250 Ry. The geometry optimization for each structure is performed to achieve forces smaller than 10 meV / Å. The mean-field Hamiltonian obtained from the converged DFT calculation was combined with the Gollum[24] implementation of the non-equilibrium Green's function method to calculate the phase-coherent, elastic scattering properties of each system consisting of left gold (source) and right gold (drain) leads and the scattering region. The transmission coefficient $T(E)$ for electrons of energy E (passing from the source to the drain) is calculated via the relation: $T(E) = Trace(\Gamma_R(E)G^R(E)\Gamma_L(E)G^{R\dagger}(E))$. In this expression, $\Gamma_{L,R}(E) = i\left(\sum_{L,R}(E) - \sum_{L,R}{}^{\dagger}(E)\right)$ describe the level broadening due to the coupling between left (L) and right (R) electrodes and the central scattering region, $\sum_{L,R}(E)$ are the retarded self-energies associated with this coupling and $G^R = (ES - H - \sum_L - \sum_R)^{-1}$ is the retarded Green's function, where H is the Hamiltonian and S is overlap matrix. Using obtained transmission coefficient $T(E)$, the conductance could be calculated by Landauer formula ($G = G_0 \int dE\, T(E)(-\partial f/\partial E)$) where $G_0 = 2e^2/h$ is conductance quantum.

Figure S21 illustrated an example of molecular junction and the calculated conductance of the molecules **Cy3$^+$–Cy11$^+$** in presence of PF_6^-. Comparing with the experimental trend our results suggest that E_F falls within the highlighted region in the figure near the middle of the HOMO-LUMO gap.

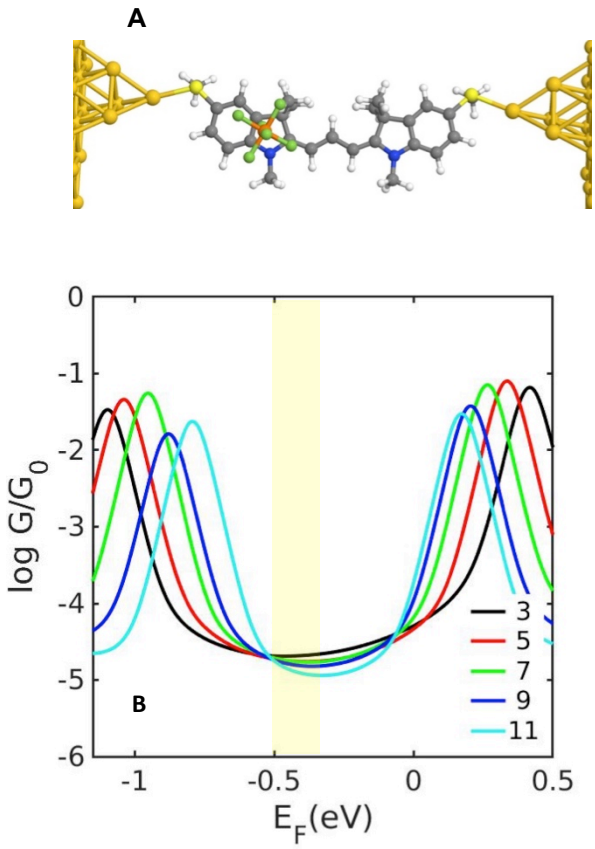

Figure S21. (A) Optimized junction structures of **Cy3·PF$_6$** (B) Calculated conductance for **Cy3·PF$_6$** – **Cy11·PF$_6$** versus electrode energy.

The bond length alternation for the longer cyanine dyes is underestimated by the DFT method used in this work (GGA-PBE/DZP) to calculate the charge transport of the junction as also reported for the cumulenes series.[25] So the attenuation factor, β, is predicted to be higher in the experiment.

Figure S22 shows the transmission coefficient and the electrical conductance of the optimized structures of the cyanine dye molecular wires in acetonitrile using BHandHLYP/6-311G*. As shown in Figure S22.C, the overall conductance for **Cy3–Cy11** are very similar. However as we go beyond the length of C**y11** the conductances drop more rapidly. This is in agreement with our bond length alternation calculation for the molecules in acetonitrile environment.

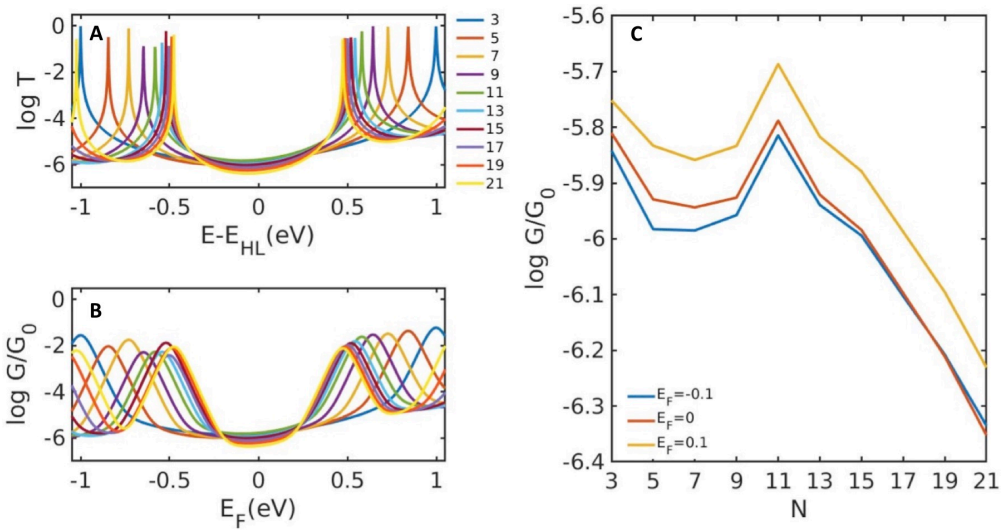

Figure S22. (A) Calculated transmission coefficient and (B) conductance for the optimized structures of **Cy3–Cy21** in acetonitrile using BHandHLYP/6-311G*, where $E_{HL} = (E_H - E_L/2)$. (C) Conductance value versus length for selected Fermi energies.

4.7. The Hückel model for a linear polymethine chain

Equation (4) results from analysis of a Hückel model of a linear chain with alternating bonds.[26] It is valid when $t_s = t_D$ and its derivation makes no assumptions about the extent of bond-length-alternation. Its validity when $t_s = t_D$ is demonstrated by equation (S1),[27] which shows that the Green's function of a Hückel model of a linear chain of N sites with non-alternating bonds of strength t_s, is given by:

$$G_{jp}(E) = \frac{\sin(kp)\sin\{k[j-(N+1)]\}}{t_s \sin[k(N+1)]\sin(k)} \qquad \text{(S1)}$$

where the Green's function G_{jp} is the wave amplitude at site j created by a source connected to site $p \leq j$, and k is the dimensionless wave vector.

When the electrodes are weakly coupled to terminal sites $p = 1$ and $j = N$, the electrical conductance is proportional to $[G_{N1}]^2$, where from equation (S1),

$$G_{N1} = \frac{-\sin(k)}{t_s \sin[k(N+1)]} \qquad \text{(S2)}$$

For N even and in the presence of $N/2$ π electrons, the middle of the HOMO-LUMO gap corresponds to $k = \pi/2$, in which case, equation (S2) yields

$$G_{N1}(0) = \frac{(-1)^{\frac{N}{2}+1}}{t_s} \qquad \text{(S3)}$$

For N odd and $(N-1)/2$ π electrons, the middle of the HOMO-LUMO gap corresponds to $k \approx \frac{\pi}{2} - \frac{\pi}{2(N+1)}$.

In this case, equation (S2) yields

$$G_{N1}(0) = \frac{1}{t_s} \qquad \text{(S4)}$$

In either case, equations (S3) and (S4) show that the electrical conductance is proportional to $[G_{N1}]^2 = 1/t_s^2$, which is independent of the length N of the chain, in agreement with equation (4).

Section 5. STM Break-Junction Measurements

5.1 Sample preparation: A gold substrate was immersed in a dichloromethane solution (10^{-4} M) containing the relevant compound for 15 minutes and subsequently removed, dried, and placed directly inside the STM. Experiments were carried out under dry ambient conditions, applying a tip-sample bias of 0.2 V.

5.2 Single Molecule Conductance Measurements: The conductance of each compound was measured using the STM-BJ method. All experiments were performed using a home-built STM, optimized for room temperature measurements in air. During the break-junction experiment, the tip is moved vertically in and out of contact with the substrate at a constant speed of approximately 10 nm/s, in 1 pm steps. For the conductance ($G = I/V$) *versus* distance measurements, a bias voltage V of 0.2 V was applied between the tip and the substrate. A linear current-to-voltage converter with two amplification stages allows us to record conductance values over a large dynamic range. The gains used in this study were 9.7×10^6 V A^{-1} and 4.6×10^8 V A^{-1}. We placed a resistor in series with the circuit of 1 MΩ to limit the current in the contact regime.

The motion of the tip and the conductance measurement are controlled by an in-house computer program to record conductance *versus* tip-displacement (*G-z*) curves. Typically, when moving out of contact, we move several nm after reaching our lower conductance limit. When in contact, the piezo moves a further 1–2 nm after reaching 1.0 G_0. These limits guarantee that a broad gold contact is formed and broken in each cycle, and that any molecular junction is broken at the end of the cycle. We aim to carry out 5000–10000 approach and retraction cycles in each run, and we vary the location of the tip over the sample in order to avoid systematic errors in the data. We focus on the opening stages of the cycle. After data acquisition is complete, we first remove any blocks of traces in which there is a clear degradation in trace quality due (most likely) to tip blunting or excessive build-up of material between the electrodes. We then use an automated routine to separate traces displaying plateaus from those with tunneling-only. This searches for regions of individual traces in which the conductance change is less than a certain amount across a minimum distance interval (for example, a plateau is identified when a $\Delta z > 0.1$ nm is needed to produce a change in conductance of $\Delta\log(G/G_0) < 0.1$ at any region below 0.5 G_0). We aim to use very similar criteria for all compounds.

Reproducibility was checked by performing the experiments on several different samples for selected compounds, preparing fresh electrodes each time. Fig. S41 shows the comparison of two samples each of **Cy7/9/11·PF$_6$** in which the histogram peak positions hardly vary.

5.3 Break-junction analysis and clustering results

Example conductance *vs.* distance traces (*G-z*) are shown in Fig. S23. The *G-z* traces were initially divided into two groups, with and without conductance plateaus (see Figs. S24 and S25 for the $B(C_6F_5)_4^-$ and PF_6^- salts, respectively). The resulting 1D conductance histograms of the plateau group (Fig. S26) contain contributions from (at least) two separate groups and cannot be described with a single Gaussian peak. We thus performed a further clustering analysis using a *k*-means based algorithm to divide the traces into subgroups (for details see reference 28). This procedure identified two main groups per compound, a 'high' and a 'low' conductance group, plus several minor groups. We then compared the 'high' and 'low' conductance groups with histograms built using only data points recorded above a (molecule dependent) threshold distance using the full

plateau-containing data set (i.e., before the clustering analysis), which focuses on the conductance of fully stretched junctions. The 'length cut' histograms coincide very closely with the 'low' conductance group (Figs. S38, 39). This analysis shows that the low conductance group represents the end-to-end transport pathway. We note that the conclusions also hold if we only consider the 'high' conductance group; Fig. S40.

Most traces fall into two main groups, a 'high' and a 'low' conductance group. A further two groups, not seen in all cases, result from traces with either 'short/high' or 'short/low' conductance plateaus. The 'high' and 'low' conductance groups both contain traces which reach the maximum expected junction length and are thus consistent with anchoring to the SMe terminal groups (Tables 12 and 13). The difference between 'high' and 'low' groups (visible from the 2D histograms shown in Figs. S28–S37) is that the high conductance traces tend to begin at high conductance and decrease upon elongation. The 'low' group traces, on the other hand, tend to show little to no change with length. The conductance at the greatest elongation of the 'high' group appears to coincide with the mean conductance for the 'low' group. This is confirmed by plotting histograms using only data points recorded above a certain threshold distance for all the plateau-containing traces for each compound (see Section 5.4 for further details).

Possible mechanisms for a decreasing conductance with length include successive rupture of multiple molecular junctions, each time reducing the number of transport pathways. Alternatively, this behavior may be explained by a single molecule initially interacting with one electrode (or both) strongly through its backbone. The majority of junctions on each sample do not contain a molecule, and typically less than 20% of all traces recorded fall into the high group. This makes multiple-molecule effects seem unlikely, and thus we suggest the latter single molecule 'sliding' mechanism is responsible for the high conductance junction states.

The short plateaus most likely represent 'failed' molecular junctions that rupture at an early stage of evolution. The 'short/high' group is probably related to highly compressed junctions with significant Au-backbone interactions. The 'short/low' group generally lies below even the 'low' conductance group and is probably representative of poorly contacted junctions.

Finally, in some cases we observe highly inclined traces, more so than generally found in the 'high' group. These probably result from molecular junctions that begin in the same geometry as the 'short/high' group but remain attached as the electrodes separate (see Fig. S31 and S35 for examples).

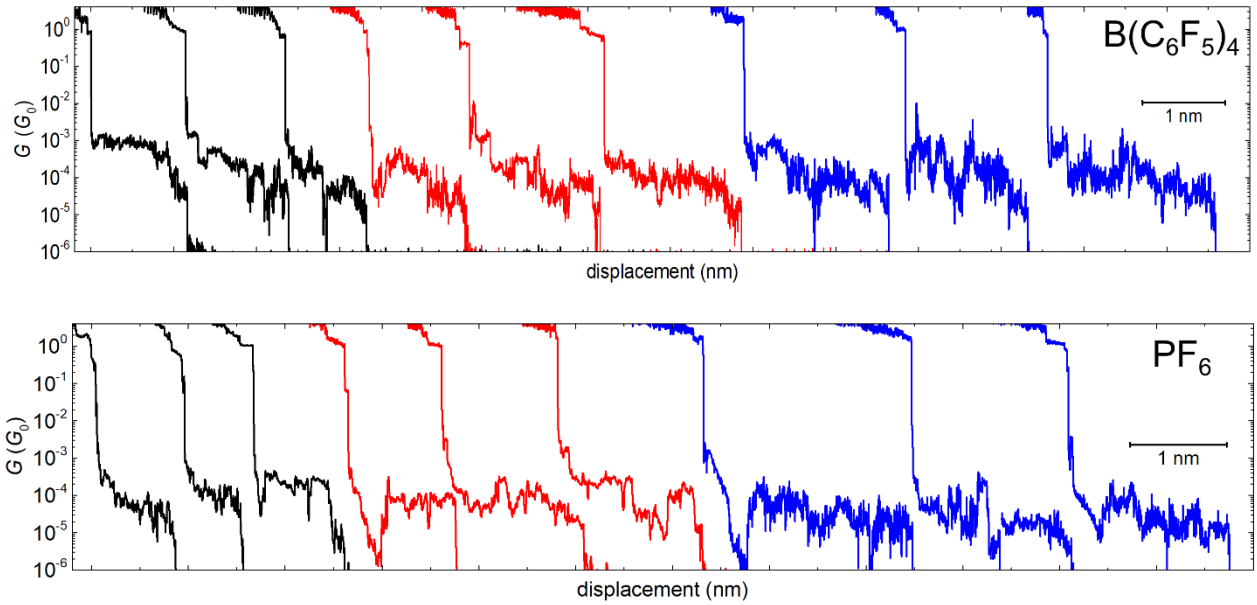

Figure S23. Examples of individual $G(z)$ traces for **Cy3/7/11** as PF_6^- salts (upper panel) and $B(C_6F_5)_4^-$ salts (lower panel). In each panel traces for **Cy3/7/11** are represented in black/red/blue respectively.

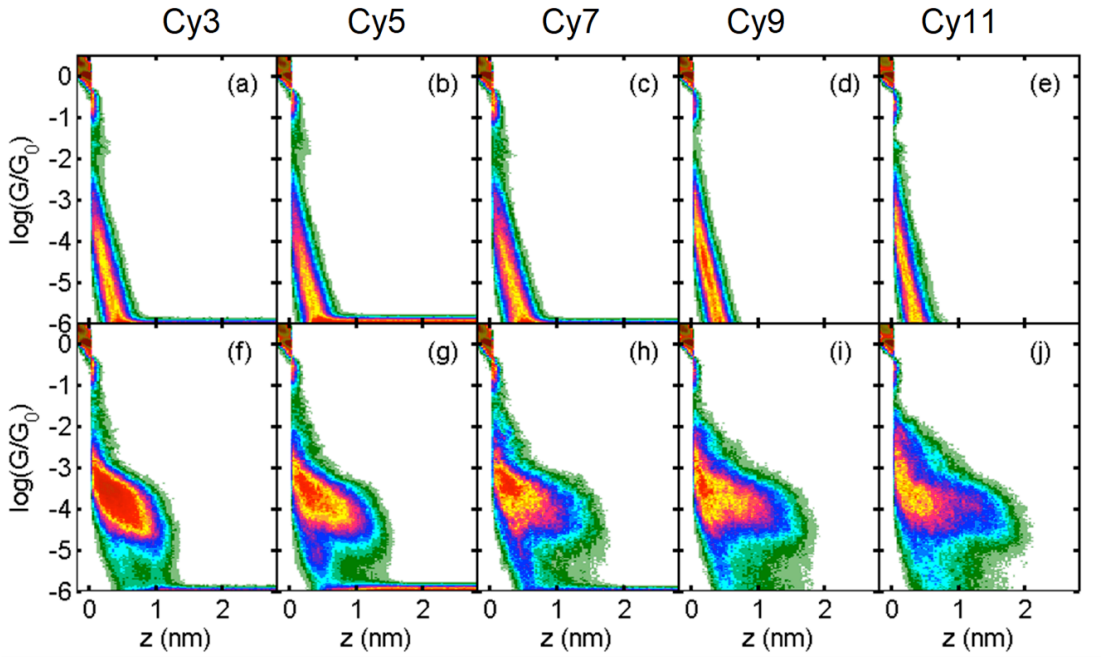

Figure S24. 2D conductance-distance histograms of pure tunneling (molecule-free) traces (a–e) and all plateau-containing traces (f–j) for cyanine-$B(C_6F_5)_4$ salts.

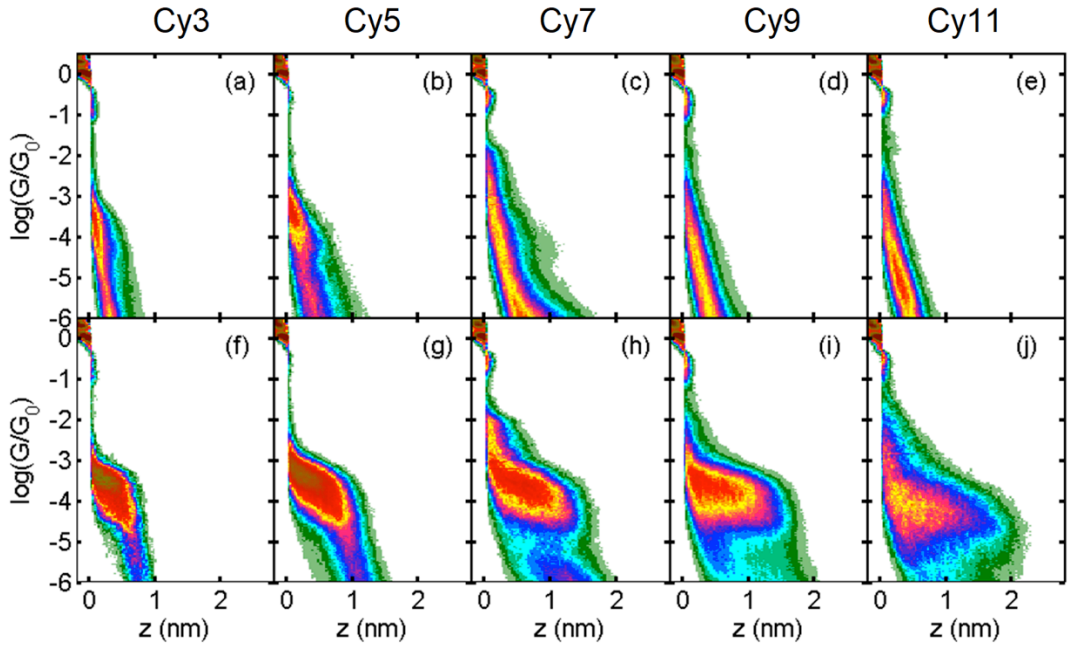

Figure S25. 2D conductance-distance histograms of pure tunneling (molecule-free) traces (a–e) and all plateau-containing traces (f–j) for cyanine-PF_6 salts.

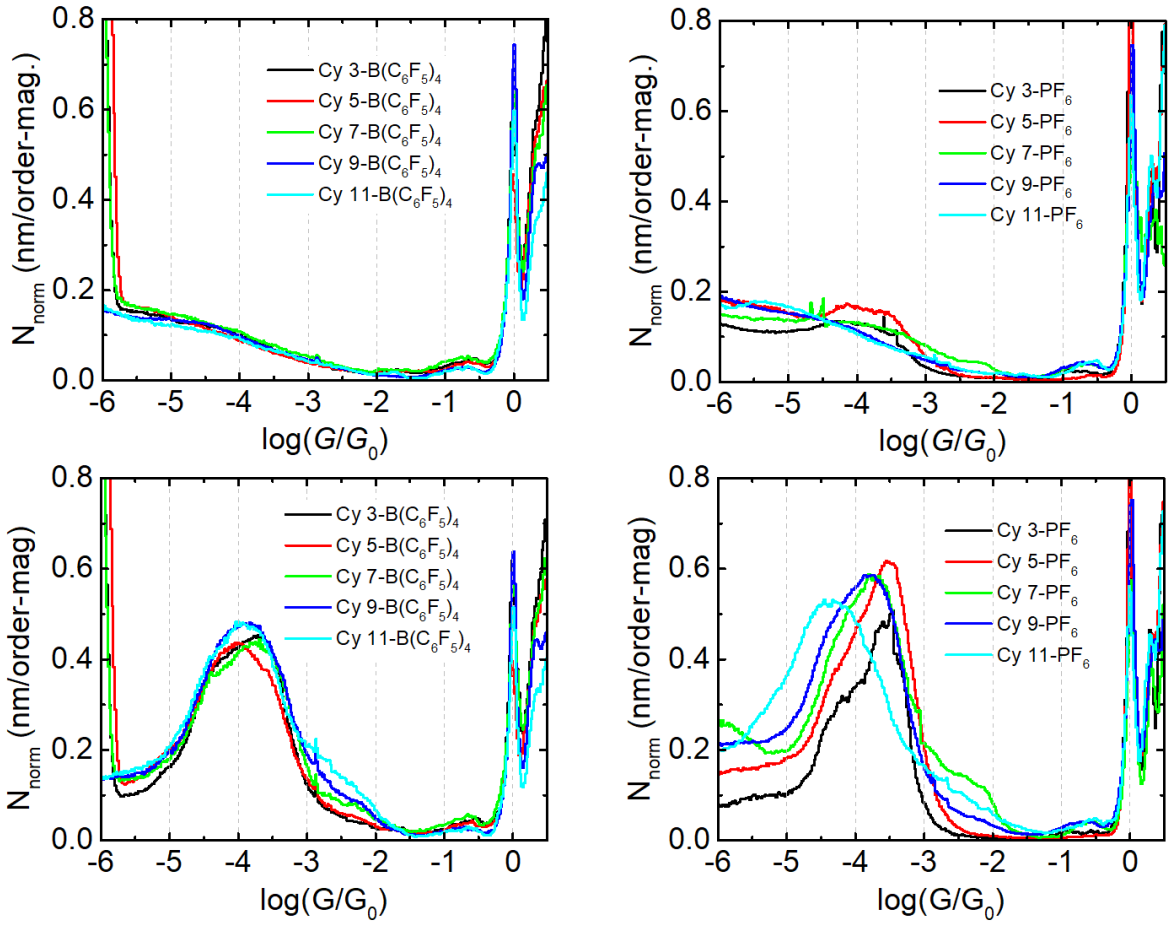

Figure S26. 1D conductance histograms of the pure tunneling (molecule-free) traces (upper panels) and all plateau-containing traces (lower panels) for all compounds measured.

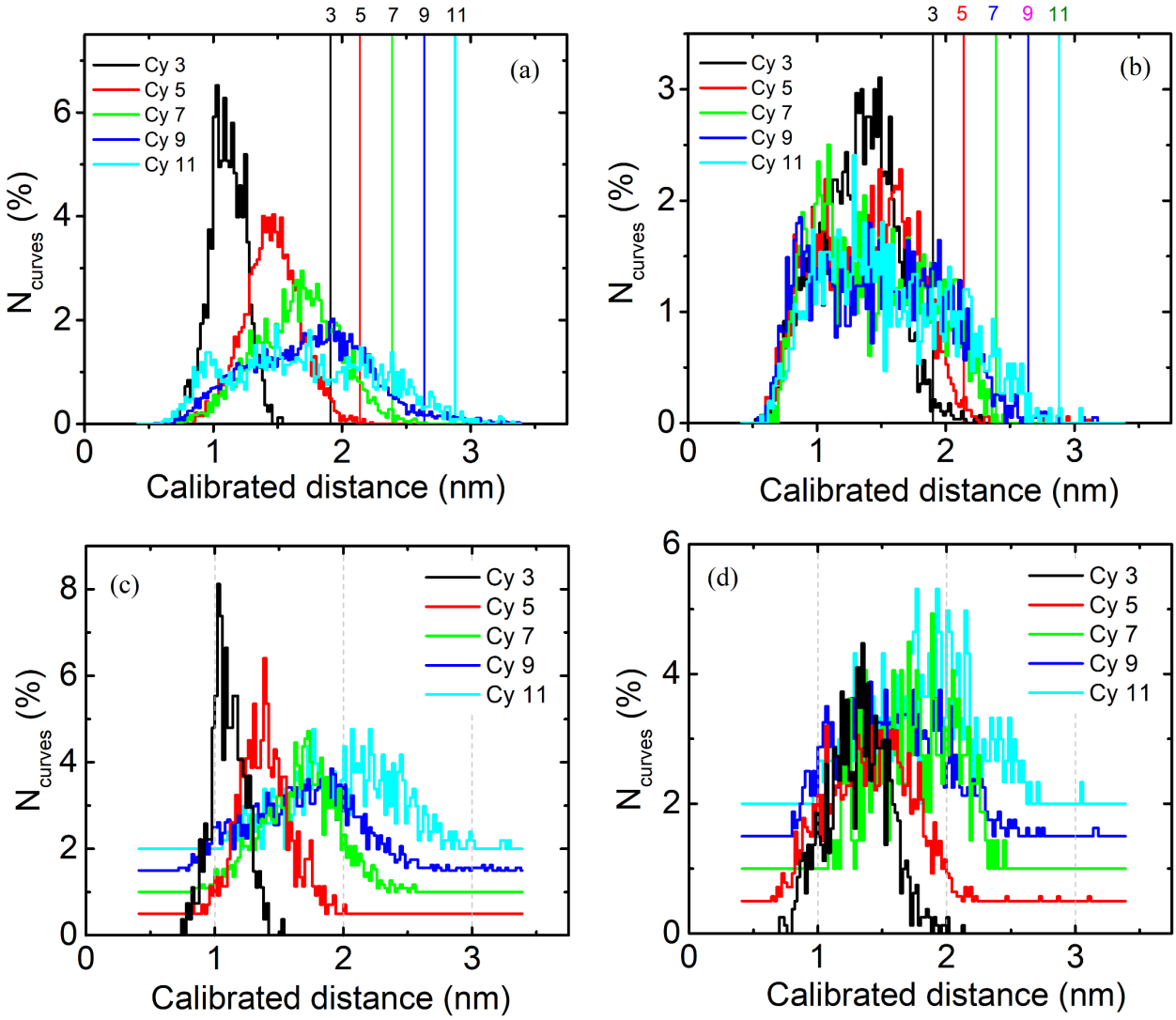

Figure S27. Calibrated plateau length distributions (achieved by adding 0.4 nm to the original plateau lengths). (a) All traces with plateaus for **Cy3-11·PF$_6$**. (b) All traces with plateaus for **Cy3-11·B(C$_6$F$_5$)$_4$**. (c) Low conductance group for **Cy3-11·PF$_6$**. (d) Low conductance group for **Cy3-11·B(C$_6$F$_5$)$_4$**. The histograms in (c) and (d) have been offset in the vertical axis for clarity. The peak values for the low and high conductance groups (not shown) are given in Tables 12 and 13.

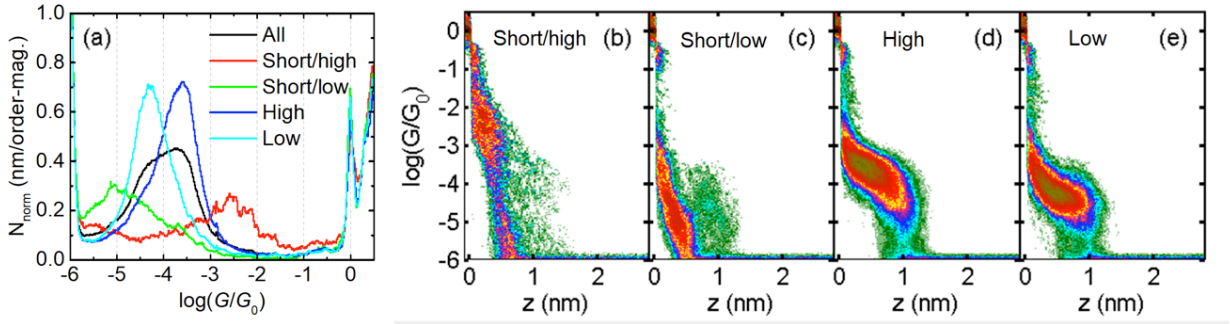

Figure S28. Cluster groups found for **Cy3·B(C$_6$F$_5$)$_4$**. (a) 1D conductance histograms. (b–e) 2D conductance-distance histograms.

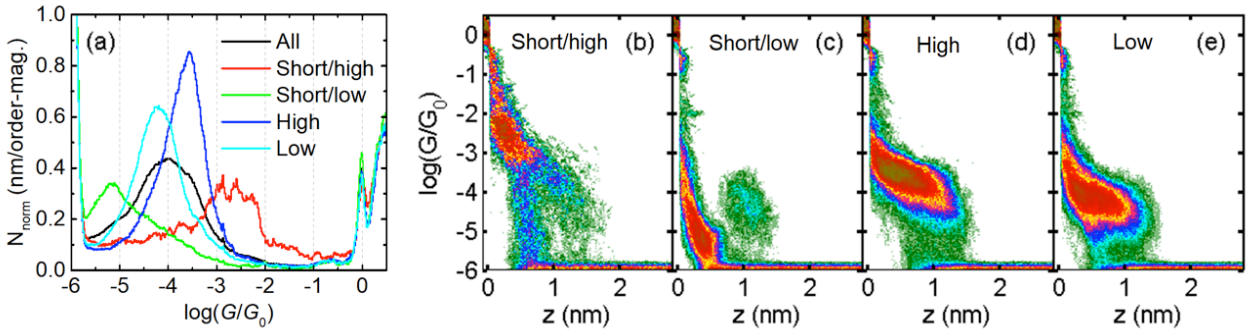

Figure S29. Cluster groups found for **Cy5·B(C$_6$F$_5$)$_4$**. (a) 1D conductance histograms. (b–e) 2D conductance-distance histograms.

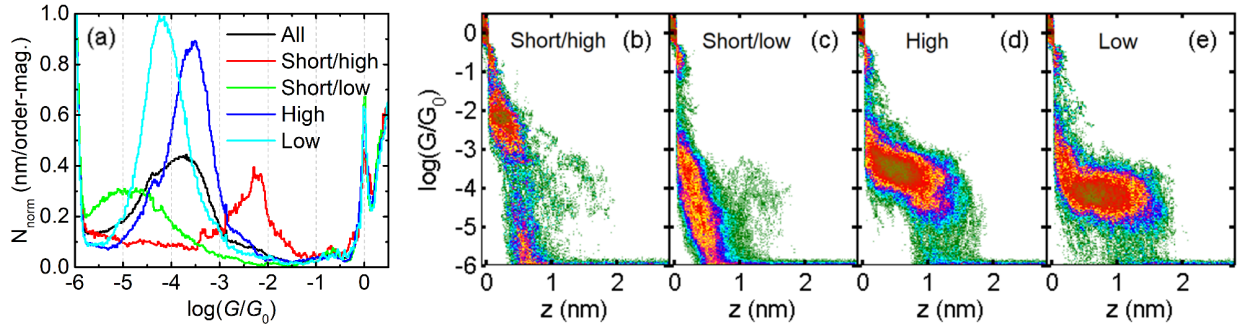

Figure S30. Cluster groups found for **Cy7·B(C$_6$F$_5$)$_4$**. (a) 1D conductance histograms. (b–e) 2D conductance-distance histograms.

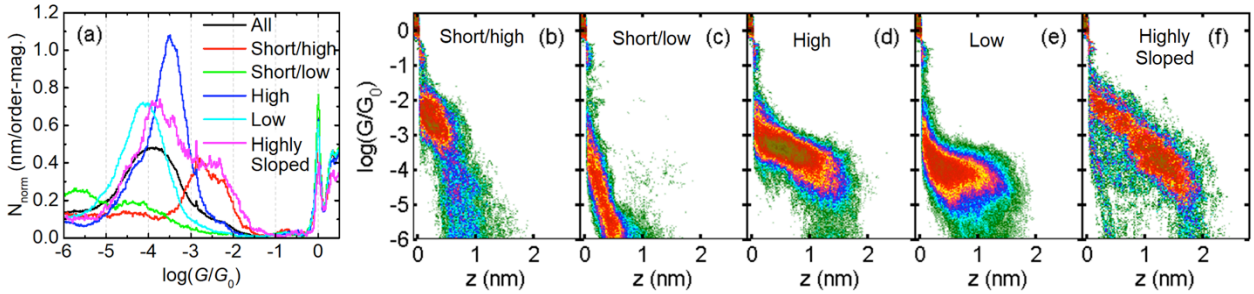

Figure S31. Cluster groups found for **Cy9·B(C$_6$F$_5$)$_4$**. (a) 1D conductance histograms. (b–e) 2D conductance-distance histograms.

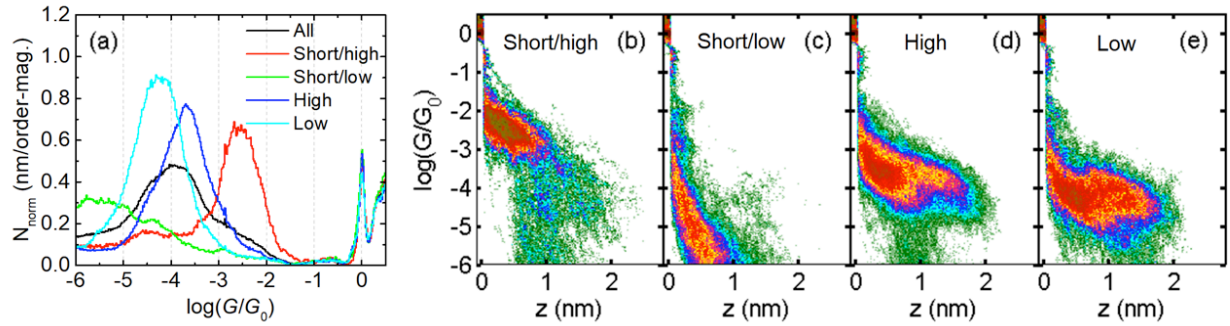

Figure S32. Cluster groups found for **Cy11·B(C$_6$F$_5$)$_4$**. (a) 1D conductance histograms. (b–e) 2D conductance-distance histograms.

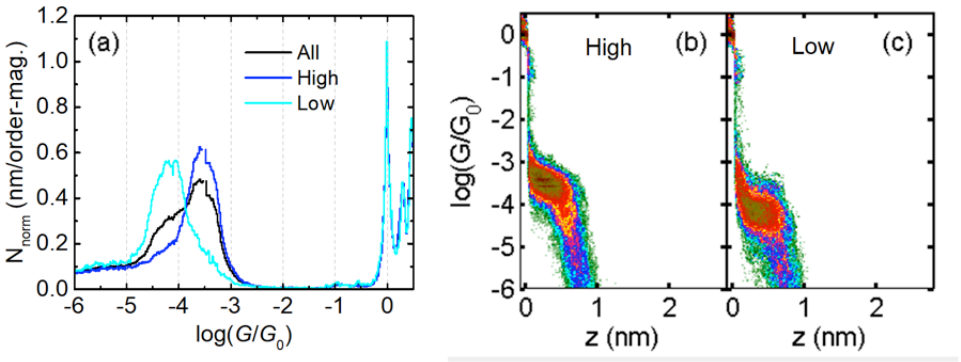

Figure S33. Cluster groups found for **Cy3·PF$_6$**. (a) 1D conductance histograms. (b-e) 2D conductance-distance histograms.

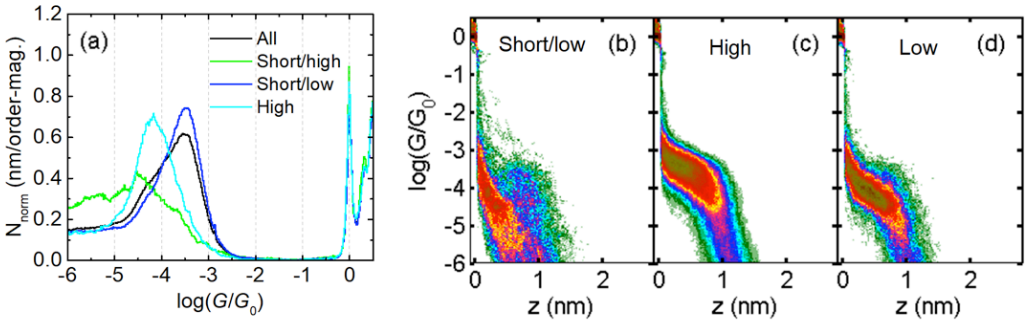

Figure S34. Cluster groups found for **Cy5·PF$_6$**. (a) 1D conductance histograms. (b–e) 2D conductance-distance histograms.

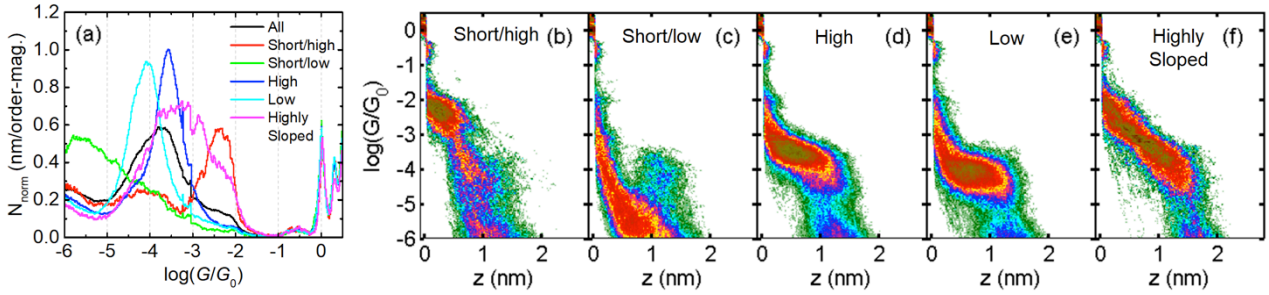

Figure S35. Cluster groups found for **Cy7·PF$_6$**. (a) 1D conductance histograms. (b–e) 2D conductance-distance histograms.

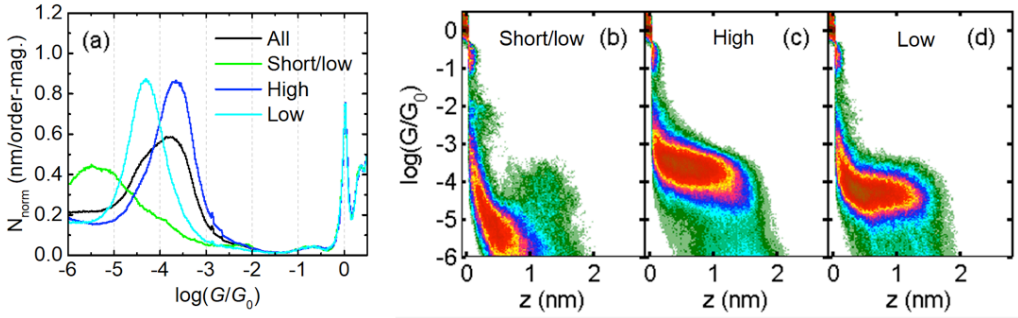

Figure S36. Cluster groups found for **Cy9·PF$_6$**. (a) 1D conductance histograms. (b–e) 2D conductance-distance histograms.

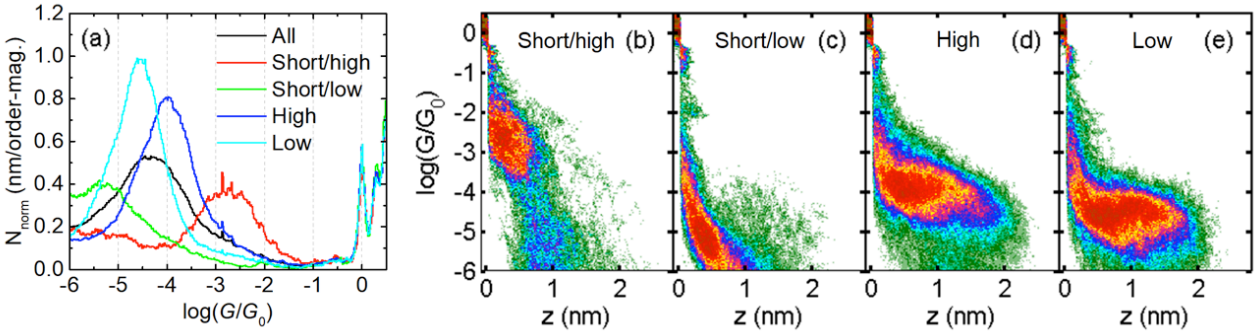

Figure S37. Cluster groups found for **Cy11·PF$_6$**. (a) 1D conductance histograms. (b–e) 2D conductance-distance histograms.

5.4. Measuring the Conductance at the End of the Plateau Length Distribution

To obtain histograms of the conductance at larger electrode separation, we restricted the number of points going into the histograms by removing those below a specified distance for each compound. This was 0.7 nm for **Cy3**, 0.8 nm for **Cy5**, 0.9 nm for **Cy7**, 1.0 nm for **Cy9** and 1.1 nm for **Cy11** (*N.B.* these distances correspond to 1.1 nm, 1.2 nm, 1.3 nm, 1.4 nm and 1.5 nm when considering the calibrated values (i.e. values with snapback distance added). Identical thresholds were used for both counter anions except for **Cy3·PF$_6$** and **Cy5·PF$_6$** whose plateaus were slightly shorter than the corresponding B(C$_6$F$_5$)$_4$ salts. In this case thresholds of 0.4 nm and 0.5 nm were used respectively). They were chosen to correspond with a distance 2–3 Å shorter than the mean plateau length in each case.

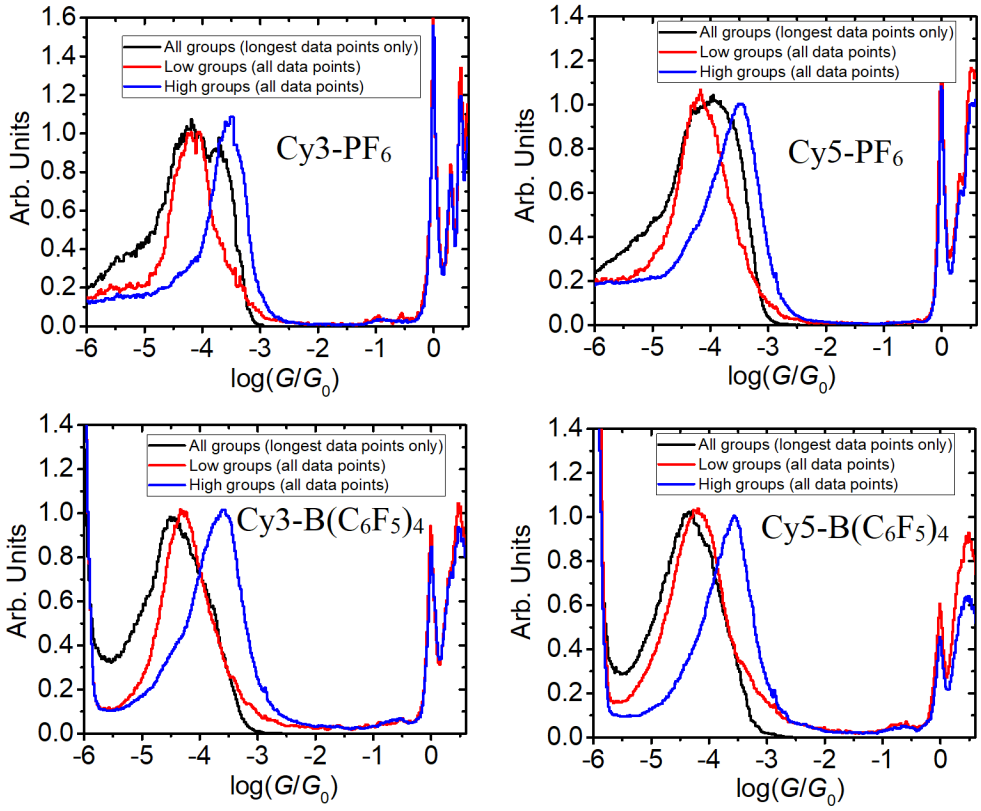

Figure S38. 1D histograms of the high and low conductance groups plotted alongside the length data restricted histograms for **Cy3** and **Cy5** salts.

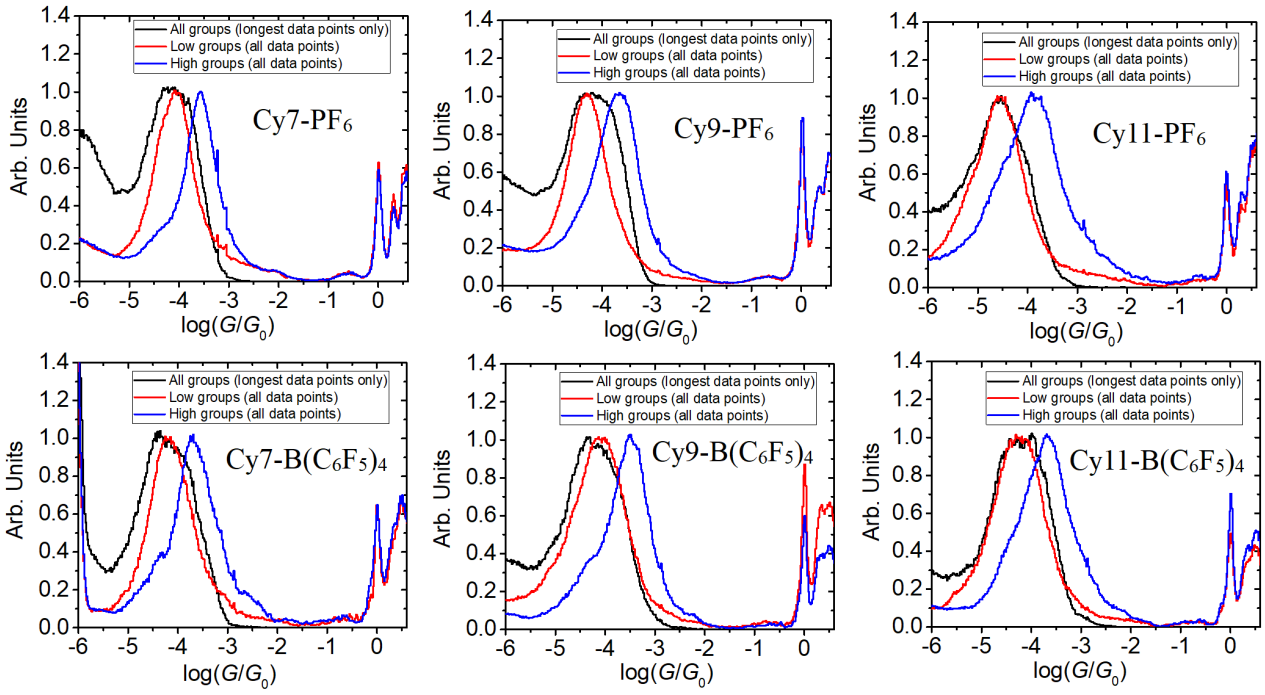

Figure S39. 1D histograms of the high and low conductance groups plotted alongside the length data restricted histograms for **Cy7**, **Cy9** and **Cy11** salts.

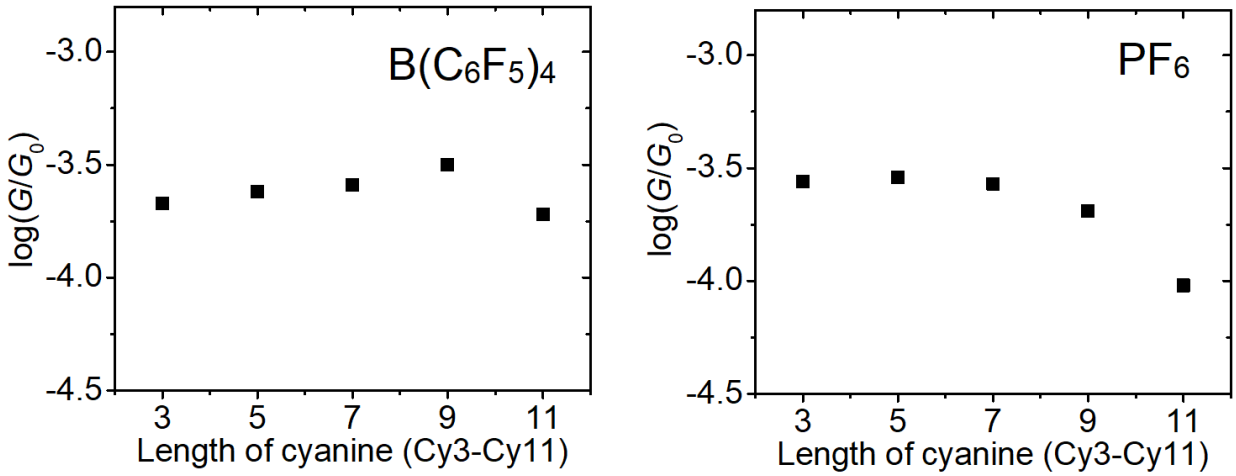

Figure S40. Mean histograms peak positions for 'high' conductance groups for cyanine salts.

Table 12. Single molecule conductance values and plateau lengths for the 'low' and 'high' groups for **Cy3**–**Cy11·B(C_6F_5)$_4$**.

	G_{low} (logG/G_0)	FWHM (logG/G_0)	G_{high} (logG/G_0)	FWHM (logG/G_0)	L_{low} (nm)[a]	L_{high} (nm)[b]	L_{calc} (nm)[c]	E_g(UV) (eV)[d]
Cy3	-4.26	0.88	-3.67	0.87	1.32 (1.77)	1.42 (1.84)	1.91	2.10
Cy5	-4.22	0.98	-3.62	0.95	1.41 (2.06)	1.54 (2.14)	2.14	1.79
Cy7	-4.15	0.96	-3.59	1.01	1.79 (2.39)	1.66 (2.31)	2.39	1.56
Cy9	-4.13	1.10	-3.50	0.88	1.54 (2.44)	1.84 (2.43)	2.64	1.37
Cy11	-4.26	1.14	-3.72	1.28	1.86 (2.65)	1.52 (2.60)	2.88	1.22

[a]Mean plateau length of the 'low' group. Values in parentheses are the 95th percentiles. [b]Mean plateau length of the 'high' group. Values in parentheses are the 95th percentiles. [c]Calculated sulfur-to-sulfur distance. [d]Values extracted from Table 1 using the CH_2Cl_2 data.

Table 13. Single molecule conductance values and plateau lengths for the 'low' and 'high' groups for **Cy3**–**Cy11·PF_6**.

	G_{low} (logG/G_0)	FWHM (logG/G_0)	G_{high} (logG/G_0)	FWHM (logG/G_0)	L_{low} (nm)[a]	L_{high} (nm)[b]	L_{calc} (nm)[c]	E_g(UV) (eV)[d]
Cy3	-4.18	0.74	-3.56	0.62	1.10 (1.34)	1.12 (1.37)	1.91	2.10
Cy5	-4.13	0.88	-3.54	1.00	1.37 (1.70)	1.48 (1.84)	2.14	1.80
Cy7	-4.10	0.82	-3.57	0.74	1.68 (2.19)	1.66 (2.21)	2.39	1.57
Cy9	-4.31	0.86	-3.69	1.08	1.69 (2.49)	1.85 (2.63)	2.64	1.37
Cy11	-4.60	1.08	-4.02	1.34	2.03 (2.86)	1.95 (2.97)	2.88	1.22

[a]Mean plateau length of the 'low' group. Values in parentheses are the 95th percentiles. [b]Mean plateau length of the 'high' group. Values in parentheses are the 95th percentiles. [c]Calculated sulfur-to-sulfur distance. [d]Values extracted from Table 1 using the CH_2Cl_2 data.

Table 14. Number of traces for each group for **Cy3–Cy11·B(C_6F_5)$_4$**.

	Total	Tunneling	All plateaus	Short/high	Short/low	High	Low	Highly Sloped
Cy3	8415	5581 (66 %)	2834 (34 %)	225 (2.7 %)	460 (5.5 %)	1344 (16 %)	805 (9.6 %)	
Cy5	10449	7027 (67 %)	3422 (33 %)	276 (2.6 %)	810 (7.8 %)	930 (8.9 %)	1406 (13 %)	
Cy7	4824	3505 (73 %)	1319 (27 %)	144 (3.0 %)	323 (6.7 %)	376 (7.8 %)	229 (4.7 %)	
Cy9	10681	8734 (82 %)	1947 (18 %)	218 (2.0 %)	464 (4.3 %)	364 (3.4 %)	799 (7.5 %)	102 (1.0 %)
Cy11	4429	2934 (66 %)	1495 (34 %)	179 (4.0 %)	400 (9.0 %)	614 (14 %)	302 (6.8 %)	

Table 15. Number of traces for each group for **Cy3–Cy11·PF_6**.

	Total	Tunneling	All plateaus	Short/high	Short/low	High	Low	Highly Sloped
Cy3	8917	8089 (91 %)	828 (9.3 %)	-	-	557 (6.2 %)	271 (3.0 %)	
Cy5	4952	1729 (35 %)	3223 (65 %)	-	321 (6.5 %)	2427 (49 %)	474 (9.6 %)	
Cy7	10902	7005 (64 %)	3897 (36 %)	368 (3.4 %)	688 (6.3 %)	1368 (13 %)	1129 (10 %)	344 (3.2 %)
Cy9	16602	10185 (61 %)	6417 (39 %)	-	1312 (7.9 %)	3488 (21 %)	1617 (9.7 %)	
Cy11	8707	6602 (76 %)	2105 (24 %)	267 (3.1 %)	491 (5.6 %)	841 (9.7 %)	506 (5.8 %)	

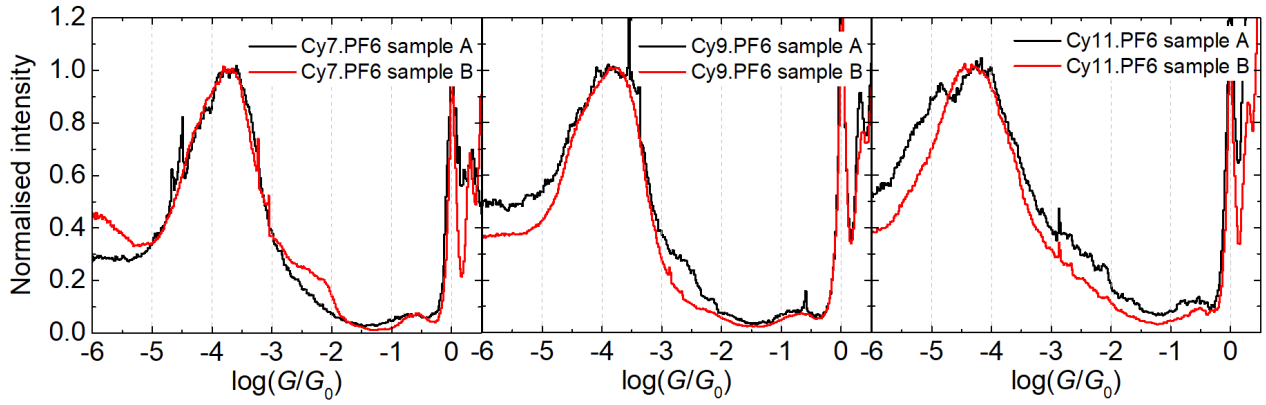

Figure S41. Normalized 1D conductance histograms of **$Cy7^+$-$Cy11^+$** PF_6^- salts from different freshly prepared samples.

5.5. Current *vs.* Voltage (*I-V*) Measurements

We carried out *I–V* measurements on **Cy3**, **Cy7** and **Cy11** PF_6 salts. For the *I–V* measurements, we paused the piezo movement at regular intervals during the stretching of a single molecule junction and perform a voltage ramp. This was done every 0.5 to 1 Å during an opening trace. A sweep rate of roughly 1 V s^{-1} was used. Between each two ramps (+*V* to –*V* and -–*V* to +*V*), the voltage was returned to a predetermined value (0.2 V) and the current recorded as the piezo is moved, thus building the full *G*(*z*) trace. After collecting the data, we selected the clearly defined *G*(*z*) plateaus and extracted the *I–V* curves. For each curve, we divided the current (*I*) by the voltage (*V*) yielding the conductance (*G*) to give a *G*-*V* trace. We then combined each *G–V* trace in the form of 2D-histograms as shown in Fig. S42.

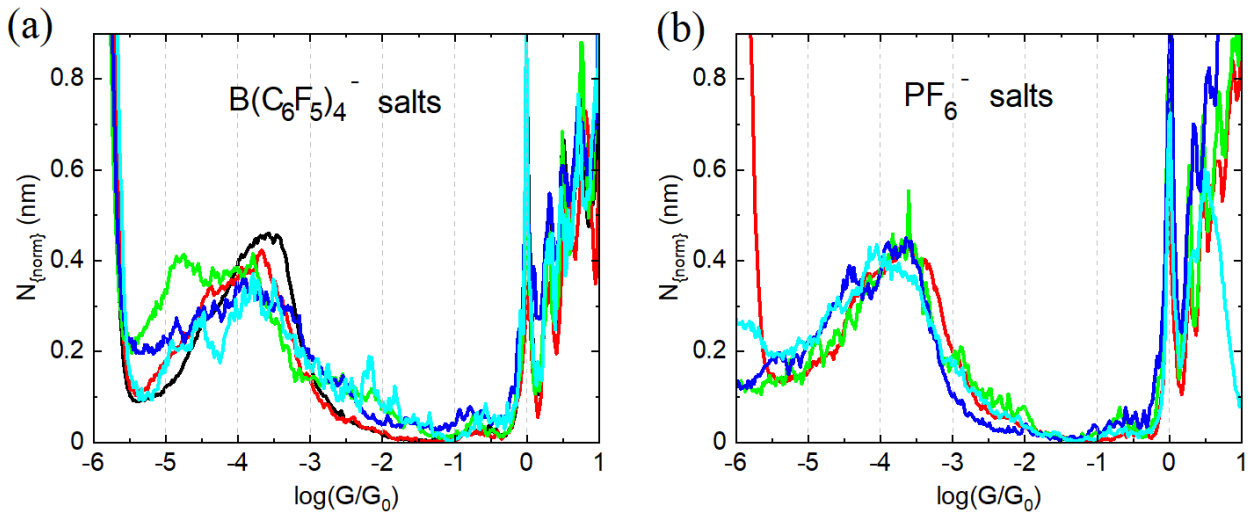

Figure S42. (a and b) 1D G_z histograms for the plateaus recorded for the $B(C_6F_5)_4^-$ salts and PF_6^- salts respectively. The color scheme is the same as used in Figure 5 of the main text.

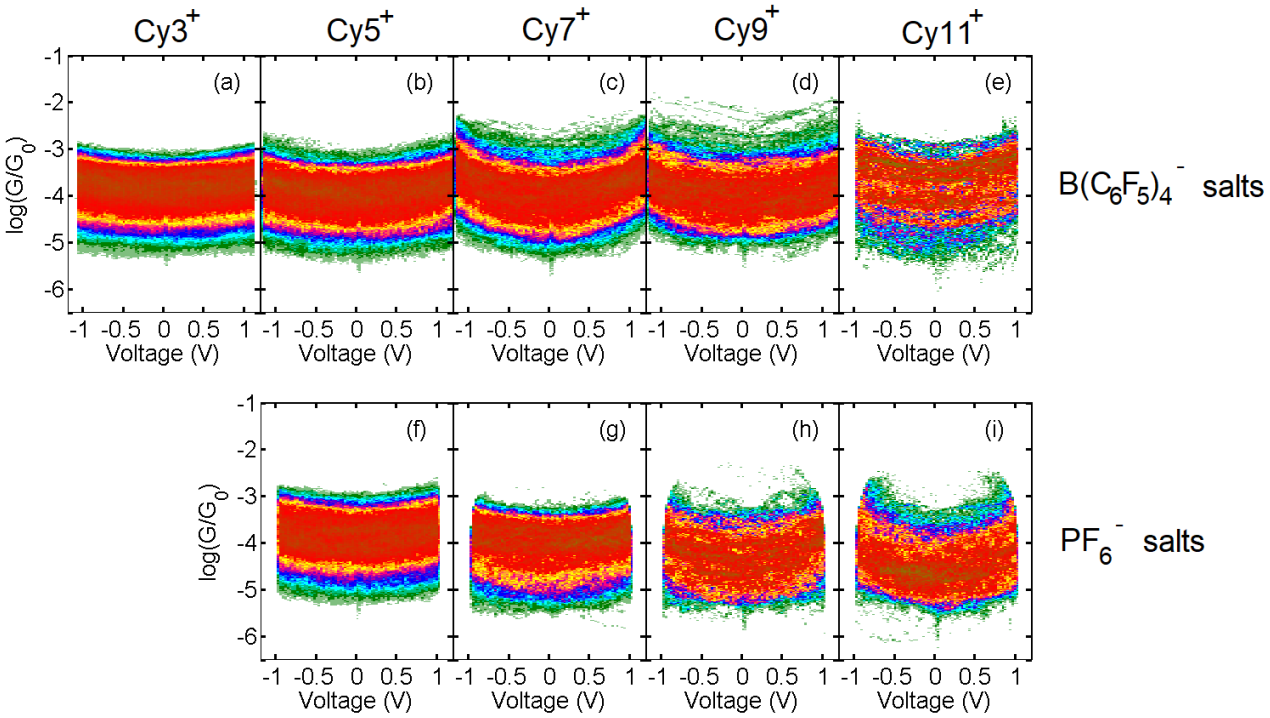

Figure S43. (a-e) 2D histograms of the log(G/G_0)-V curves for **Cy3**$^+$- **Cy11**$^+$ $B(C_6F_5)_4^-$ salts and (f-i) **Cy5**$^+$-**Cy11**$^+$ PF_6 salts. The number of individual G-V curves in each is given in Table 16.

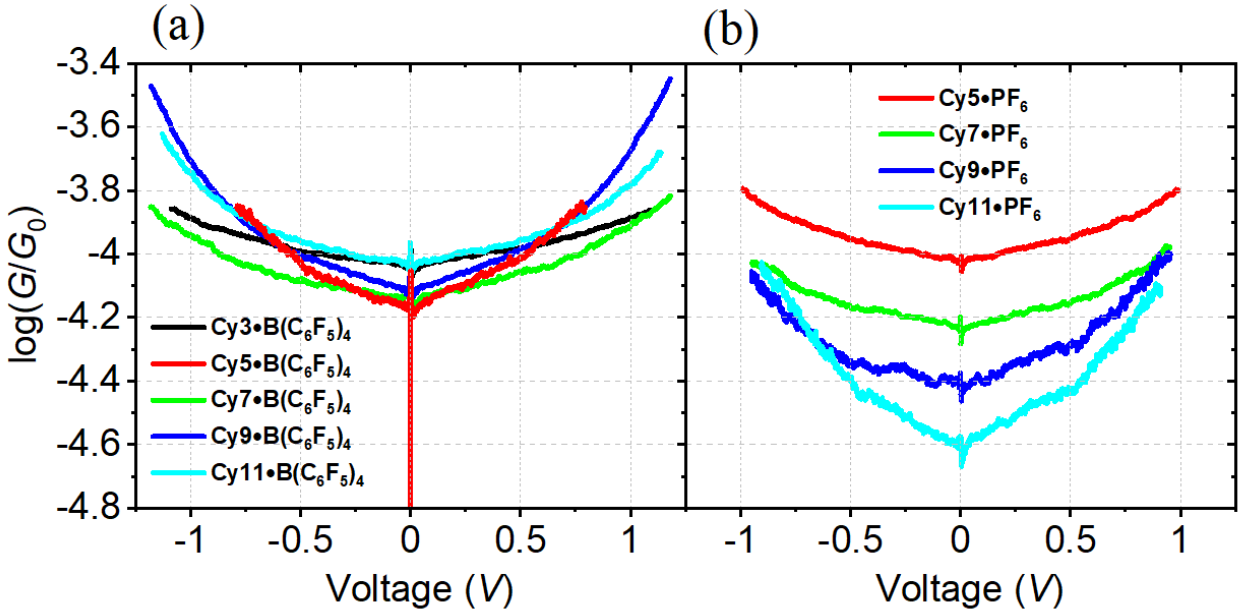

Figure S44. Mean log(G/G_0)-V curves for **Cy3**$^+$-**Cy11**$^+$ as $B(C_6F_5)_4^-$ and PF_6^- salts.

Table 16. Number of *G-V* curves and junctions studied for **$Cy3^+$–$Cy11^+$ $B(C_6F_5)_4^-$ and PF_6^- salts**.

	***G-V* curves $B(C_6F_5)_4^-$ salts**	***G-z* curves $B(C_6F_5)_4^-$ salts**	***G-V* curves PF_6^- salts**	***G-z* curves PF_6^- salts**
$Cy3^+$	3253	1204		
$Cy5^+$	1351	472	1668	389
$Cy7^+$	1205	328	917	125
$Cy9^+$	916	279	236	226
$Cy11^+$	152	68	274	225

5.6. Thermopower Measurements

We carried out a thermoelectric characterization of **Cy5·$B(C_6F_5)_4$**. To do so, a temperature difference, ΔT, was established between the tip and the substrate and small voltage ramps were applied during the formation of the molecular junctions with the STM-BJ technique.[29] The voltage ramps (*IV* curves) allowed simultaneous measurement of conductance, G, and thermovoltage, V_{th}, at different points during the evolution of single molecule junctions. We used a range of ΔT values between 0 and 15 K. The resulting thermovoltage histograms were fitted with Gaussian distributions to obtain the mean thermovoltage. These values are plotted in Fig. S42 as a function of ΔT. The Seebeck coefficient, described by $S = -V_{th}/\Delta T$, was obtained from the slope of a linear fit of V_{th} *vs.* ΔT and the values are shown in Fig. S43.

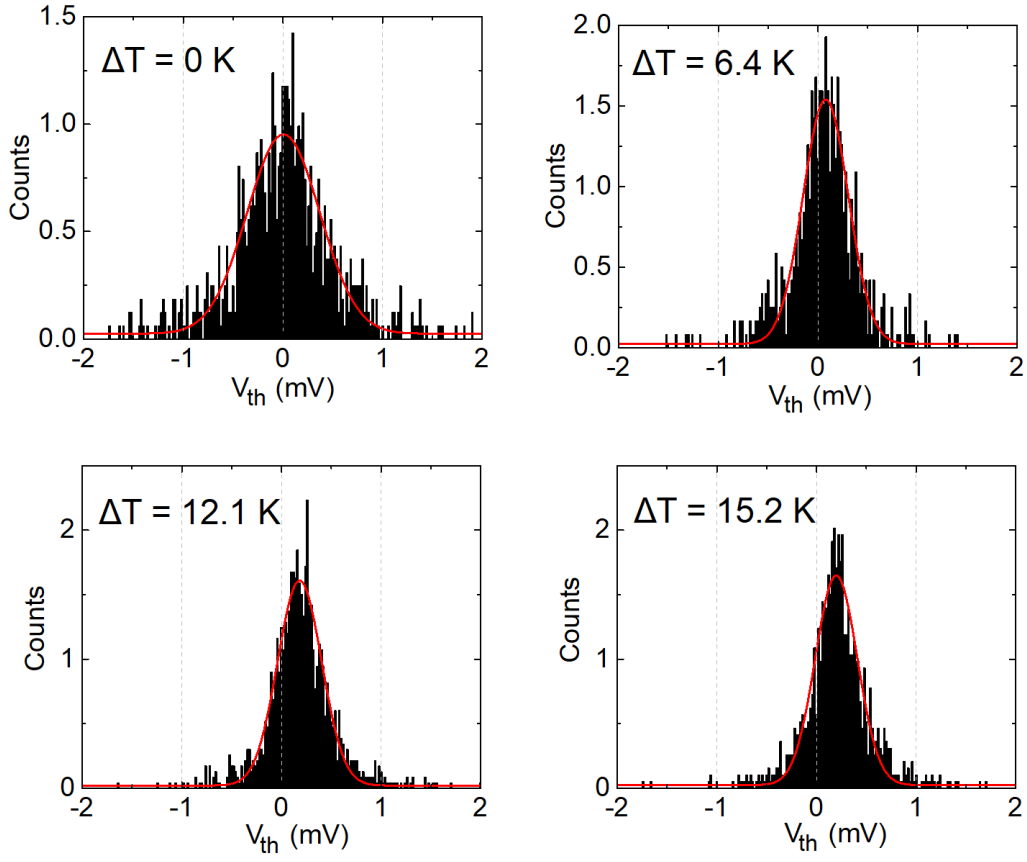

Figure S45. Thermovoltage histograms obtained with different temperature differences applied between the tip and the substrate. Red lines represent Gaussian fits to each histogram.

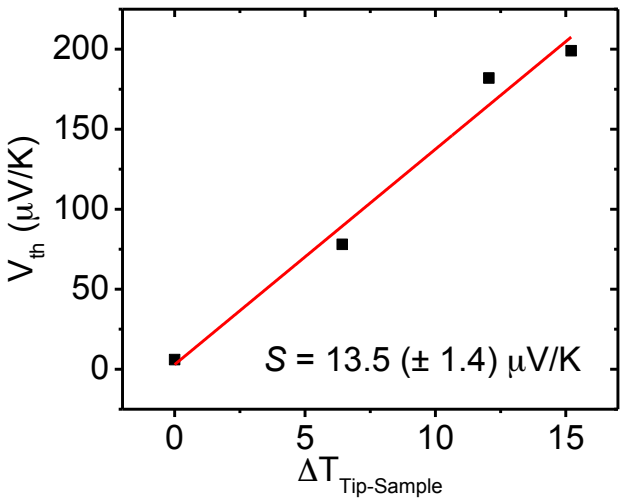

Figure S46. Seebeck coefficient (*S*) of **Cy5·B(C$_6$F$_5$)$_4$**. The red line is a linear fit to the mean thermovoltage values obtained from Gaussian fits to the thermovoltage histograms (black squares). The Seebeck coefficient is taken as the slope of the fit.

Section 6. NMR Spectra

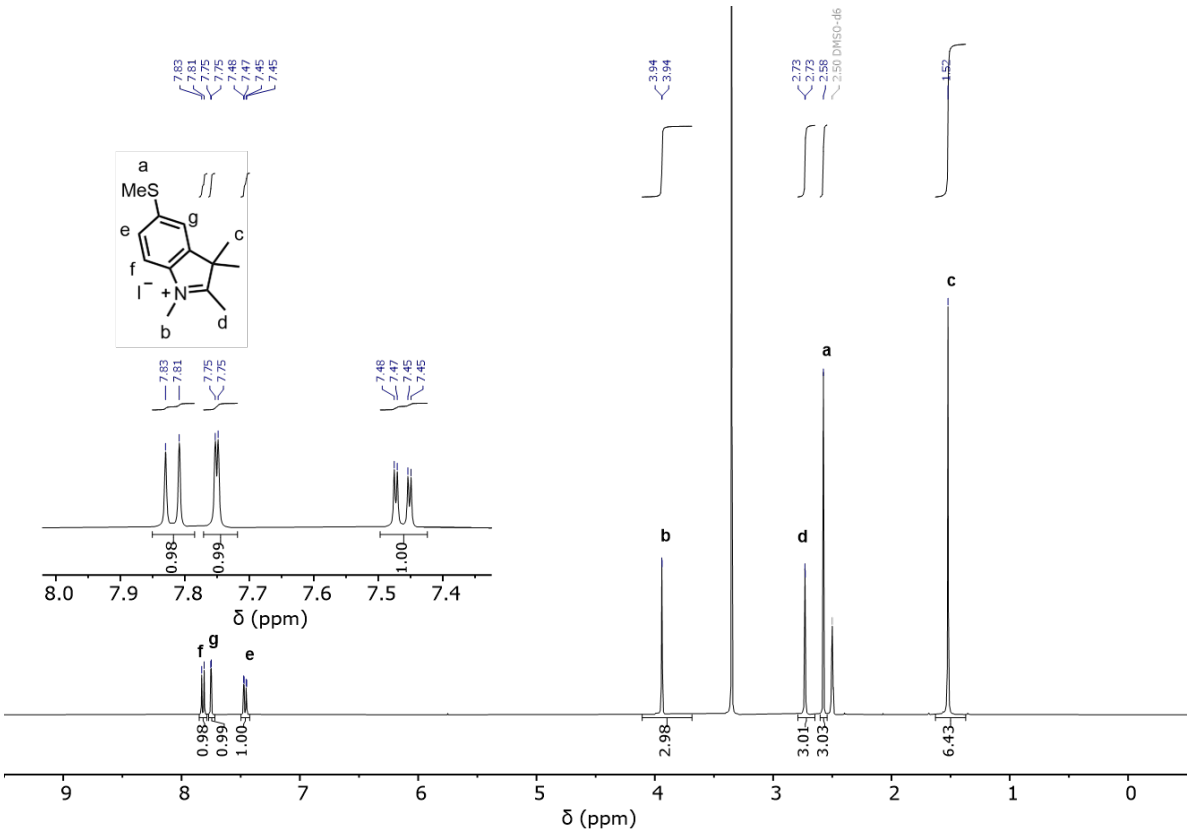

Figure S47. ^{1}H NMR spectrum of compound **S2** (d_6-DMSO, 400 MHz, 298 K).

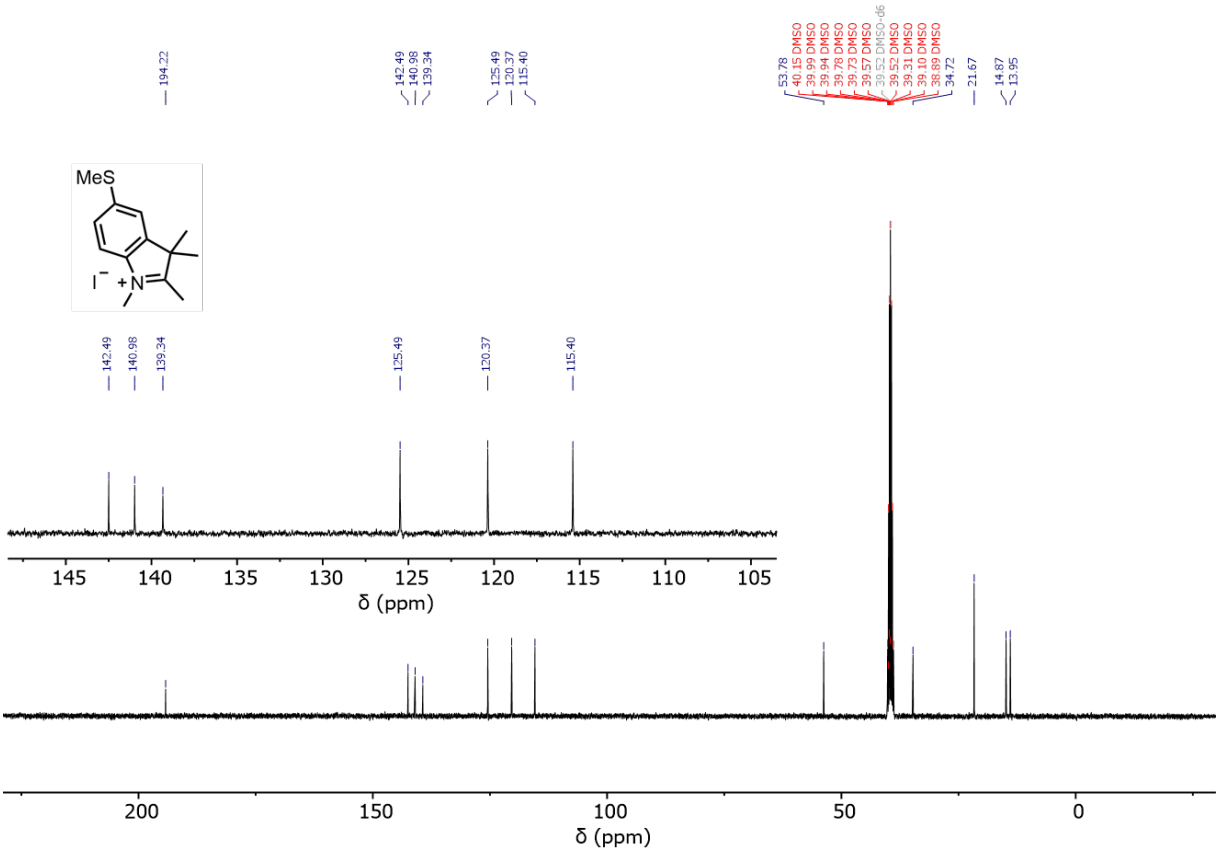

Figure S48. ^{13}C NMR spectrum of compound **S2** (d_6-DMSO, 100 MHz, 298 K).

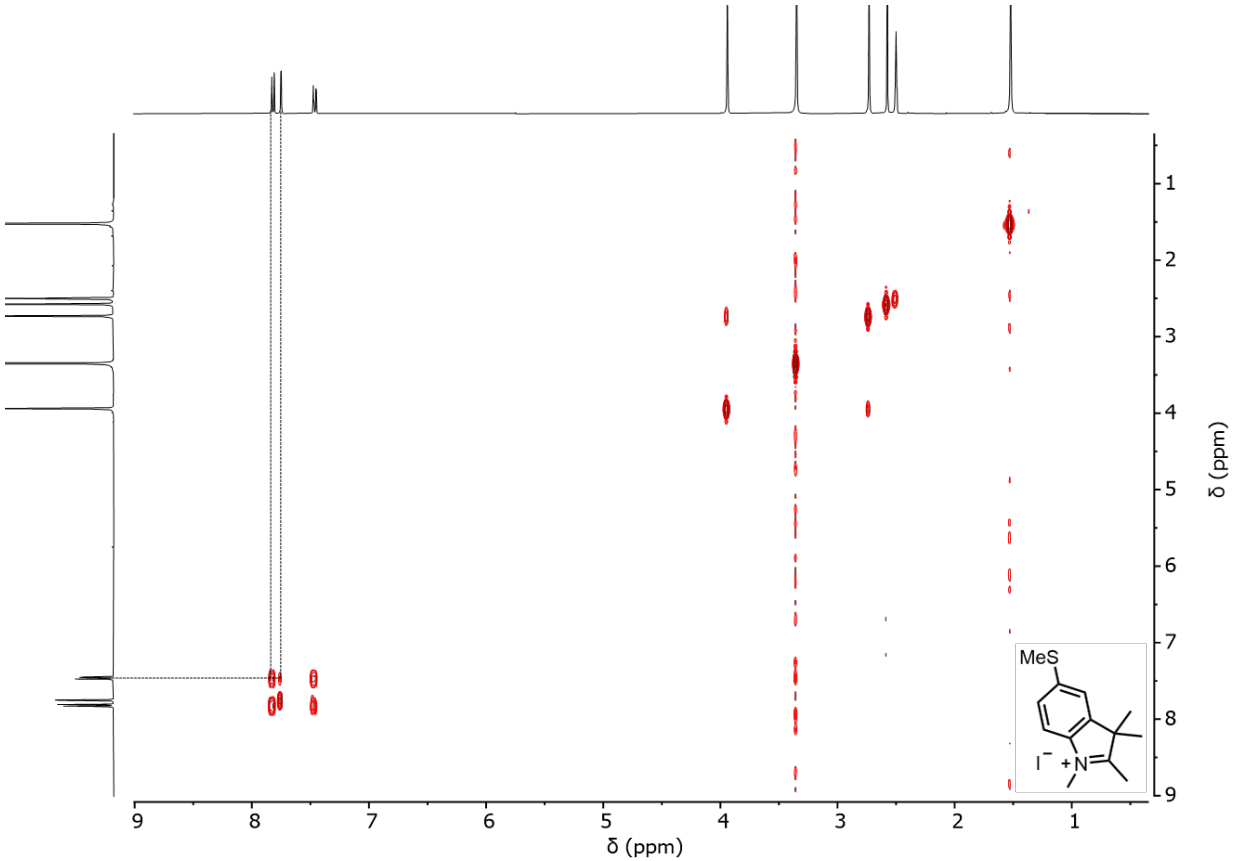

Figure S49. ^{1}H-^{1}H COSY NMR spectrum of compound **S2** (d_6-DMSO, 400 MHz, 298 K).

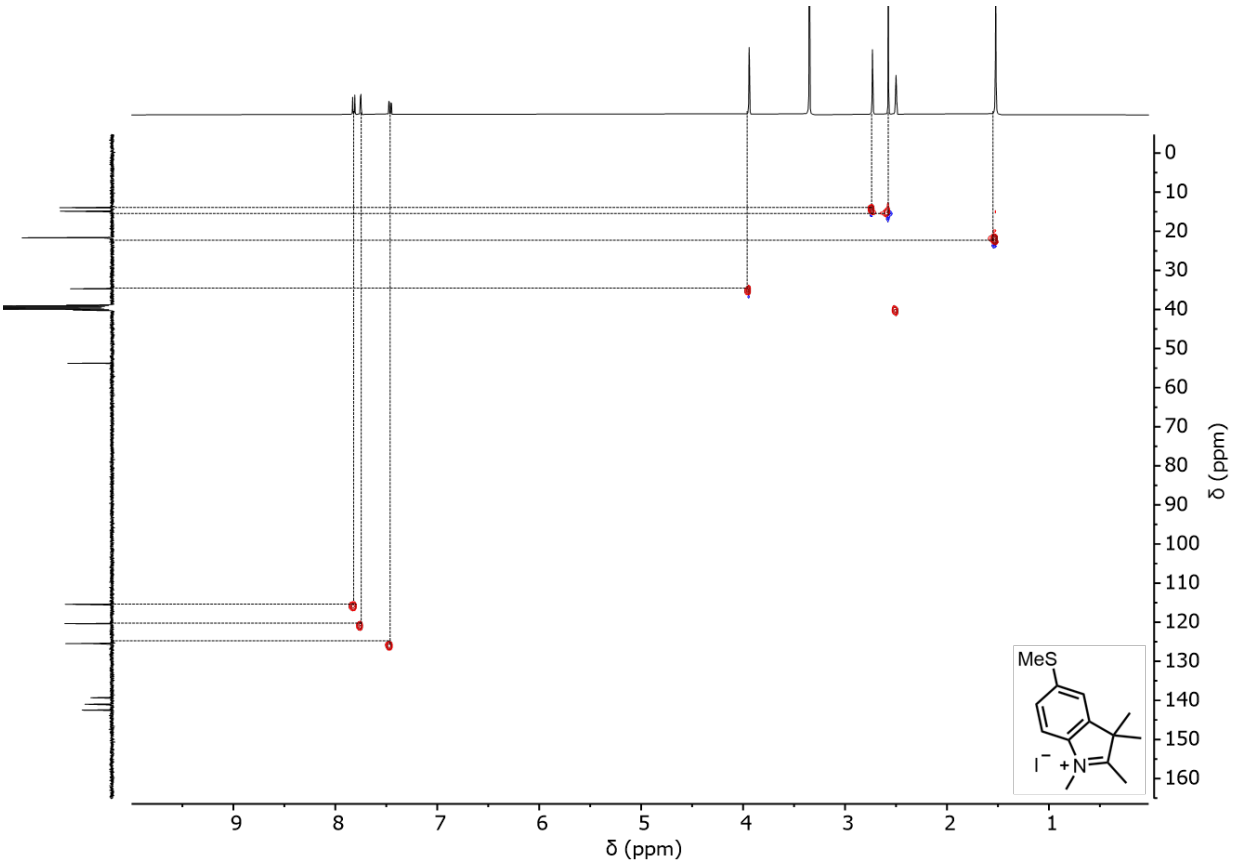

Figure S50. ^{13}C-^{1}H HSQC NMR spectrum of compound **S2** (d_6-DMSO, 100 MHz, 298 K).

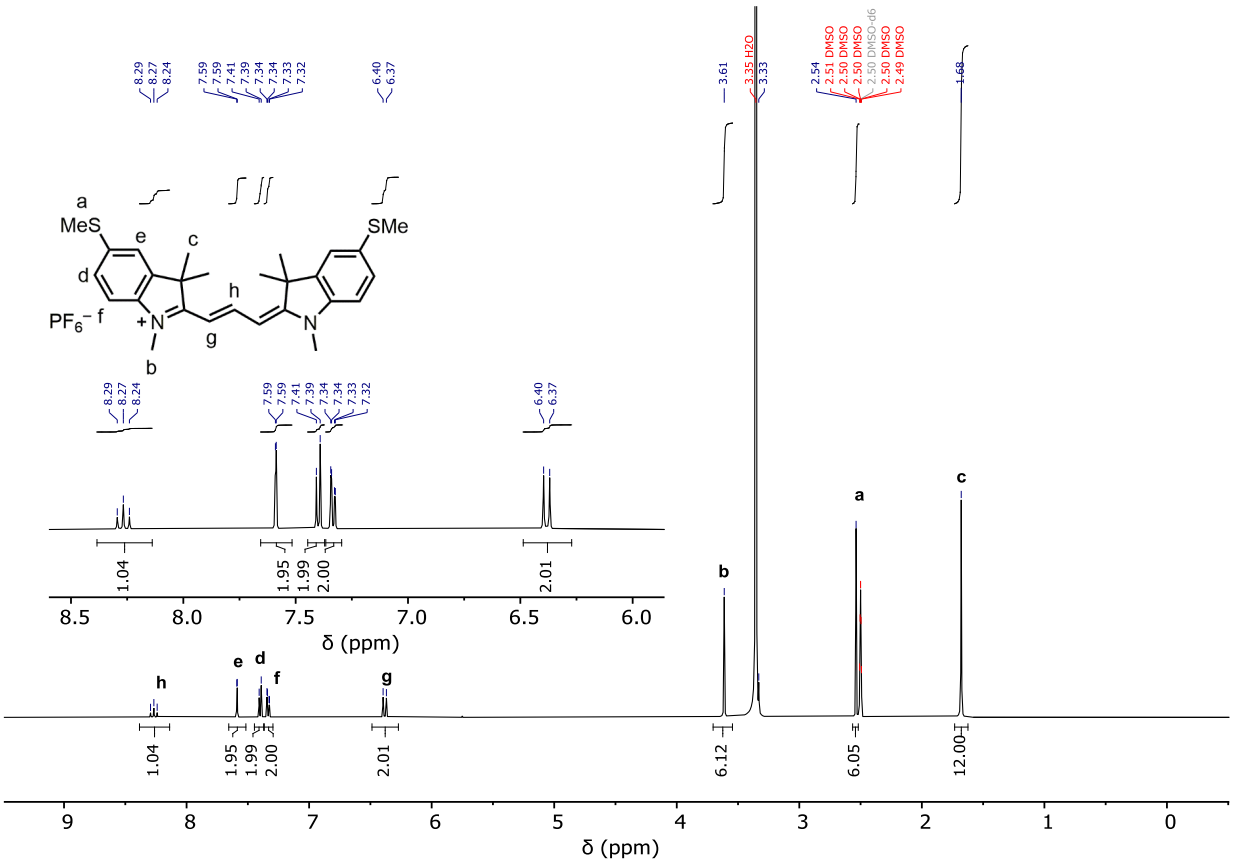

Figure S51. ^{1}H NMR spectra of **Cy3·PF$_6$** (d_6-DMSO, 500 MHz, 298 K).

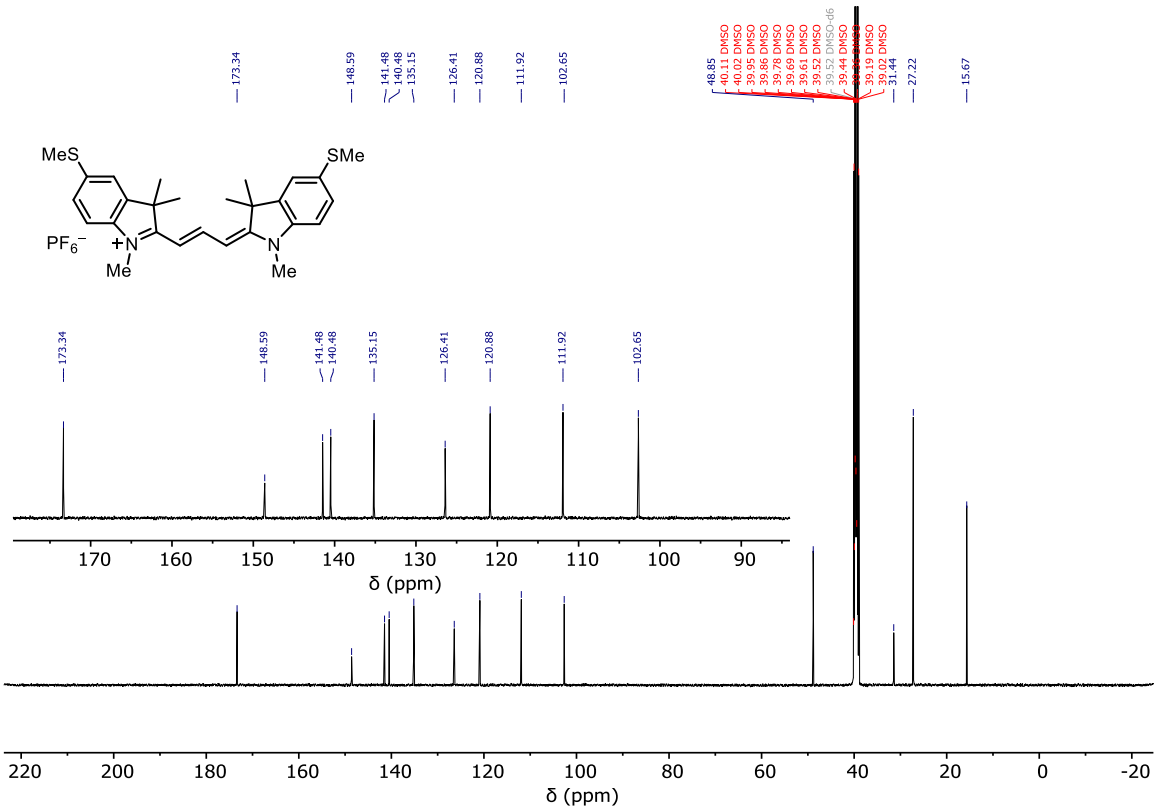

Figure S52. ^{13}C NMR spectra of **Cy3·PF$_6$** (d_6-DMSO, 125 MHz, 298 K).

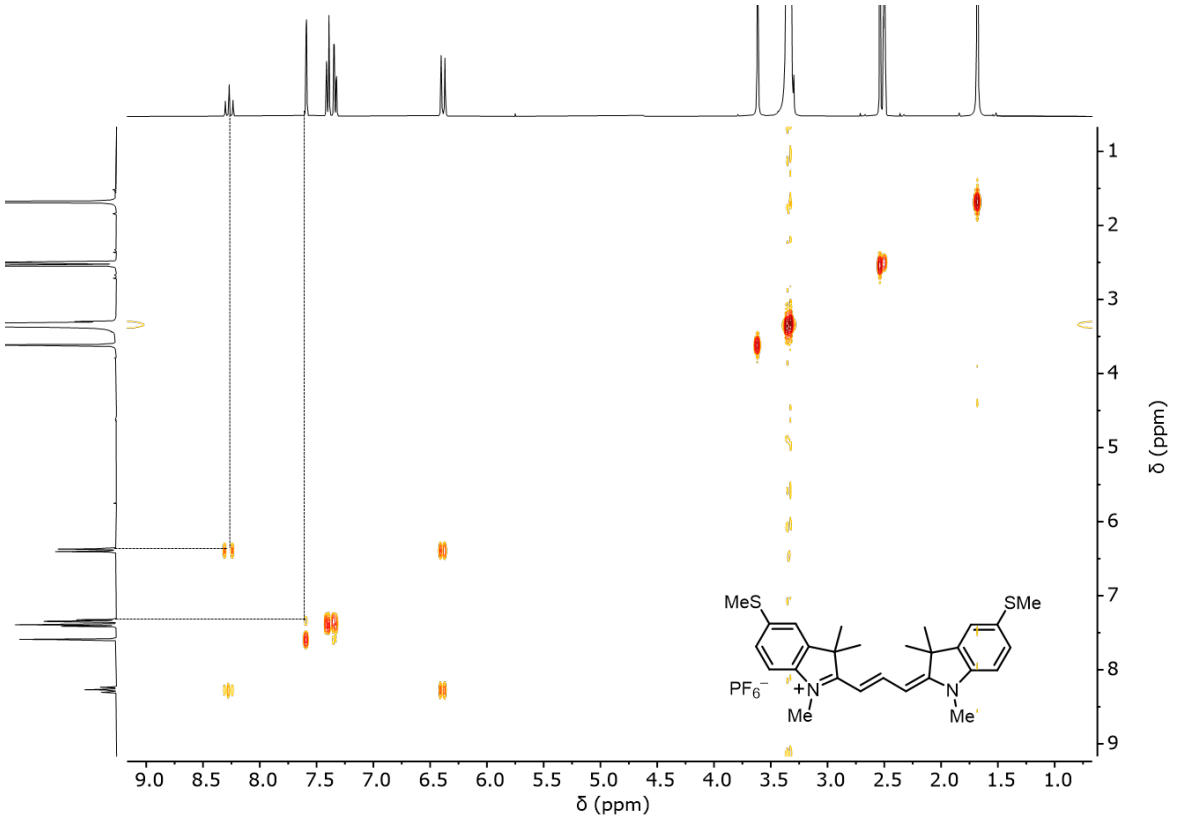

Figure S53. ^{1}H-^{1}H COSY NMR spectrum of **Cy3·PF$_6$** (d_6-DMSO, 400 MHz, 298 K).

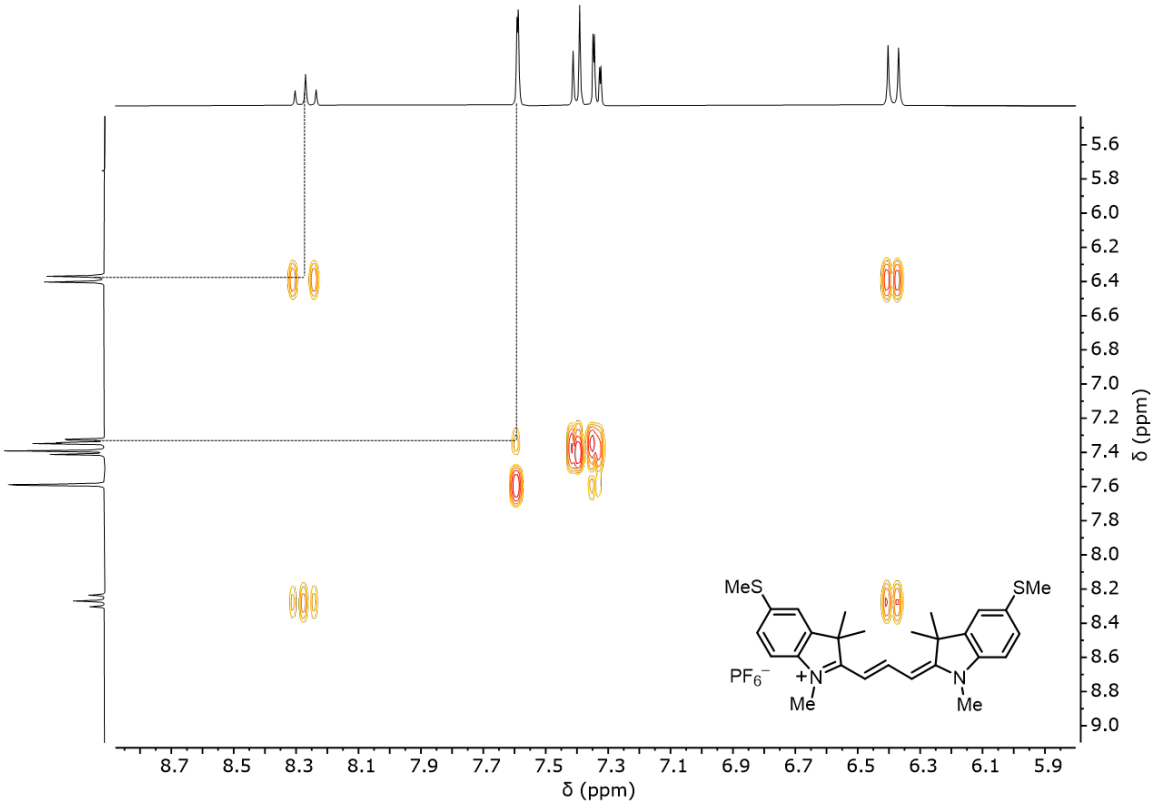

Figure S54. ^{1}H-^{1}H COSY NMR spectrum of **Cy3·PF$_6$**, zoom-in (d_6-DMSO, 400 MHz, 298 K).

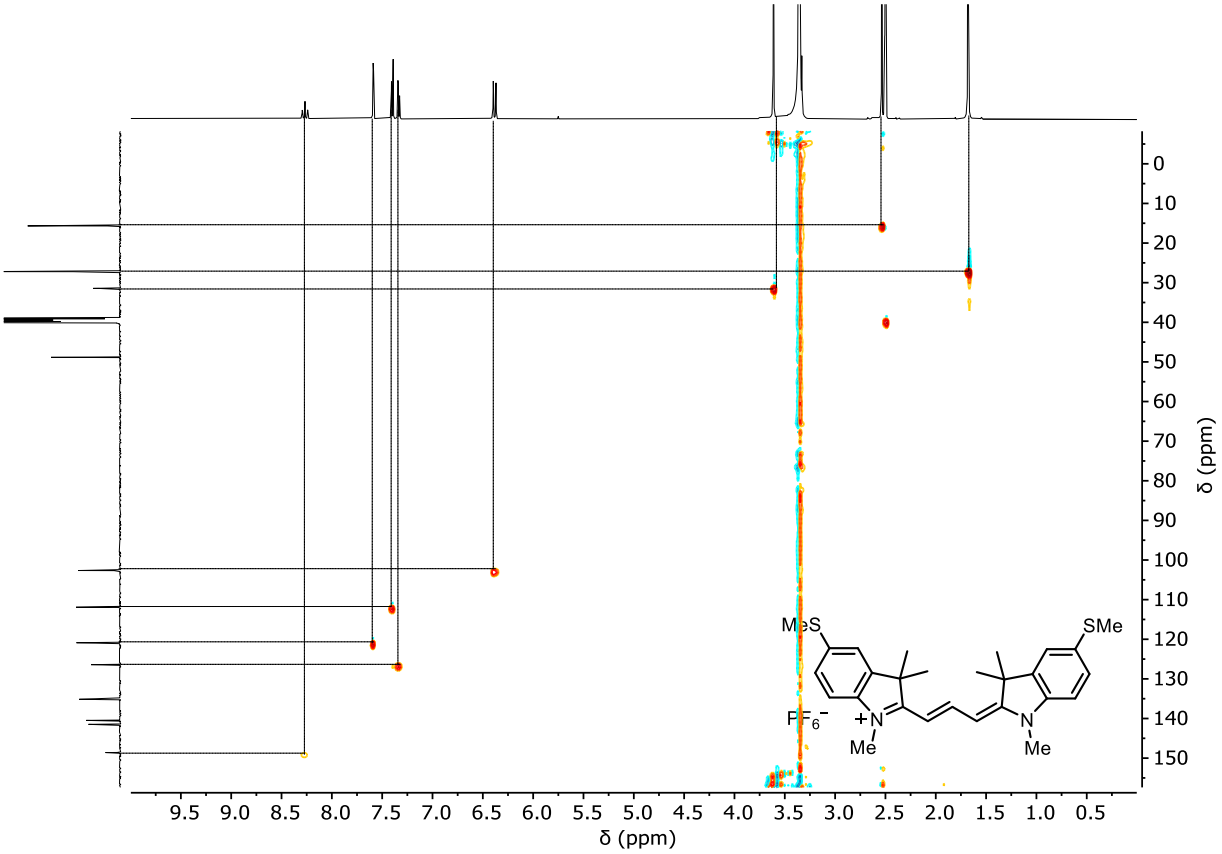

Figure S55. ^{13}C-^{1}H HSQC NMR spectrum of **Cy3·PF$_6$** (d_6-DMSO, 125 MHz, 298 K).

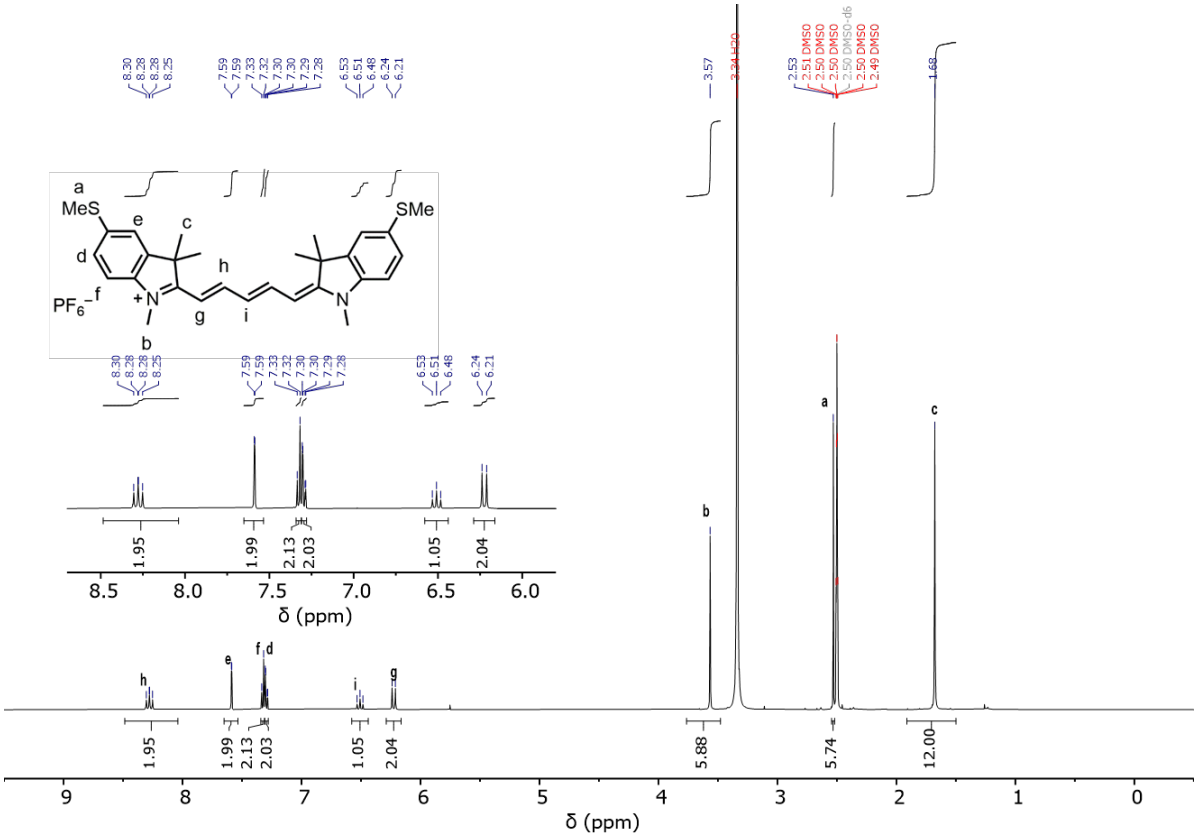

Figure S56. ^{1}H NMR spectrum of **Cy5·PF$_6$** (d_6-DMSO, 500 MHz, 298 K).

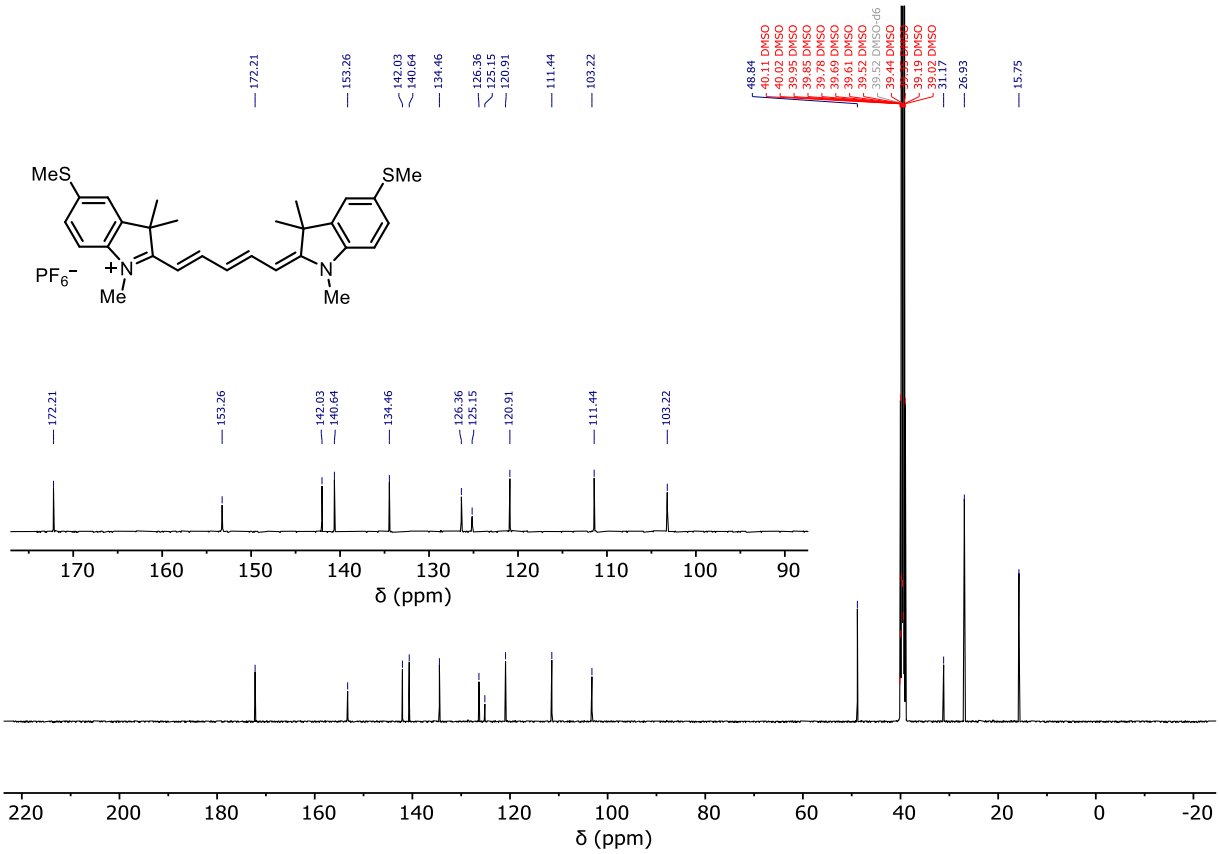

Figure S57. ^{13}C NMR spectra of **Cy5·PF$_6$** (d_6-DMSO, 125 MHz, 298 K).

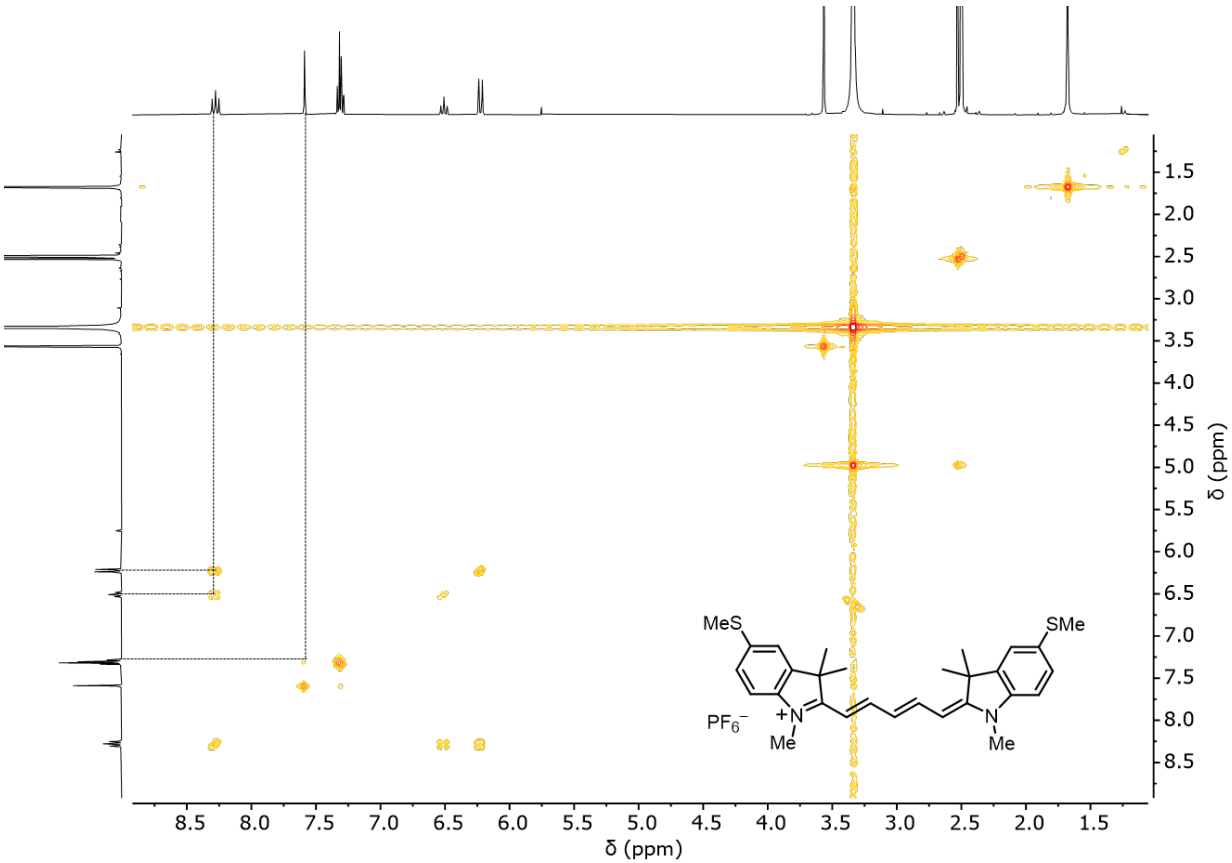

Figure S58. ^{1}H-^{1}H COSY NMR spectrum of **Cy5·PF$_6$** (d_6-DMSO, 500 MHz, 298 K).

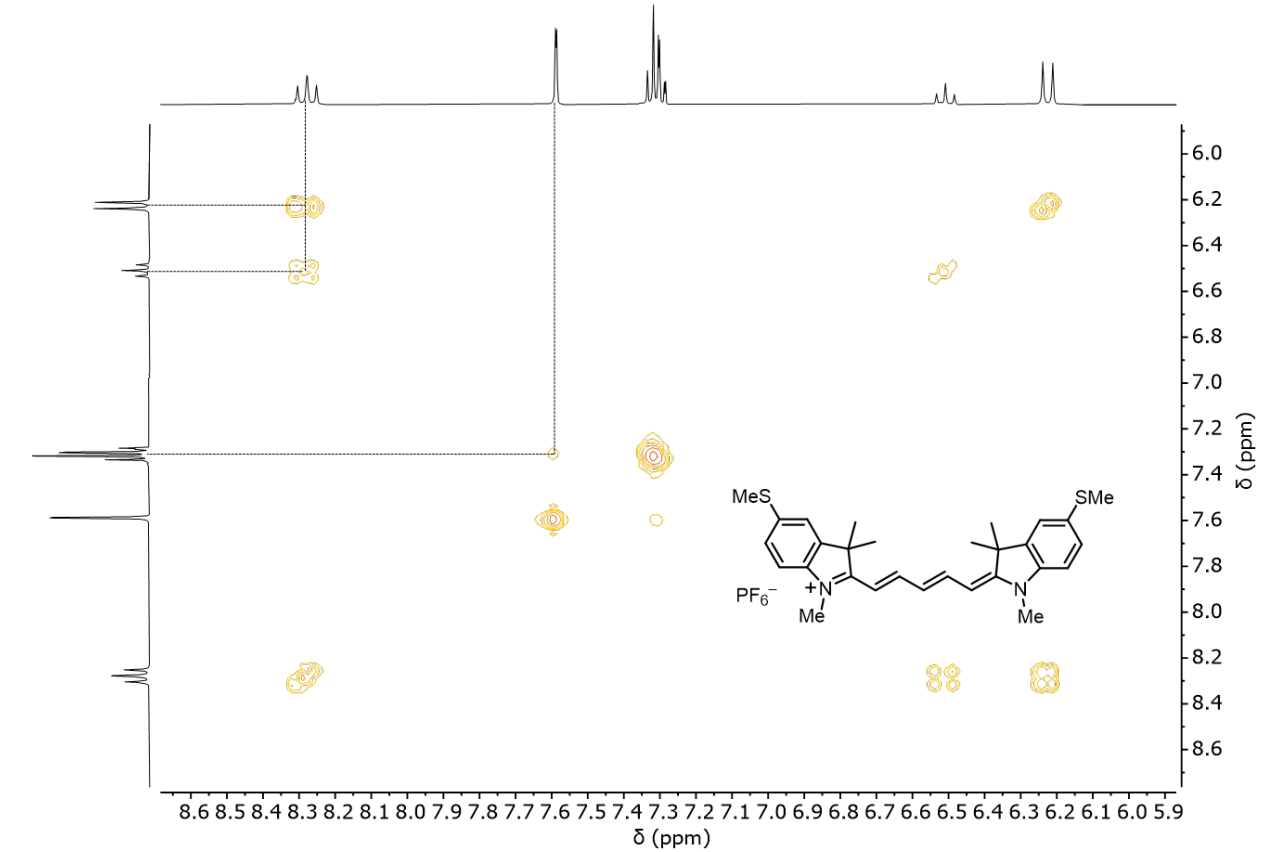

Figure S59. ^{1}H-^{1}H COSY NMR spectrum of **Cy5·PF$_6$** with zoom-in (d_6-DMSO, 500 MHz, 298 K).

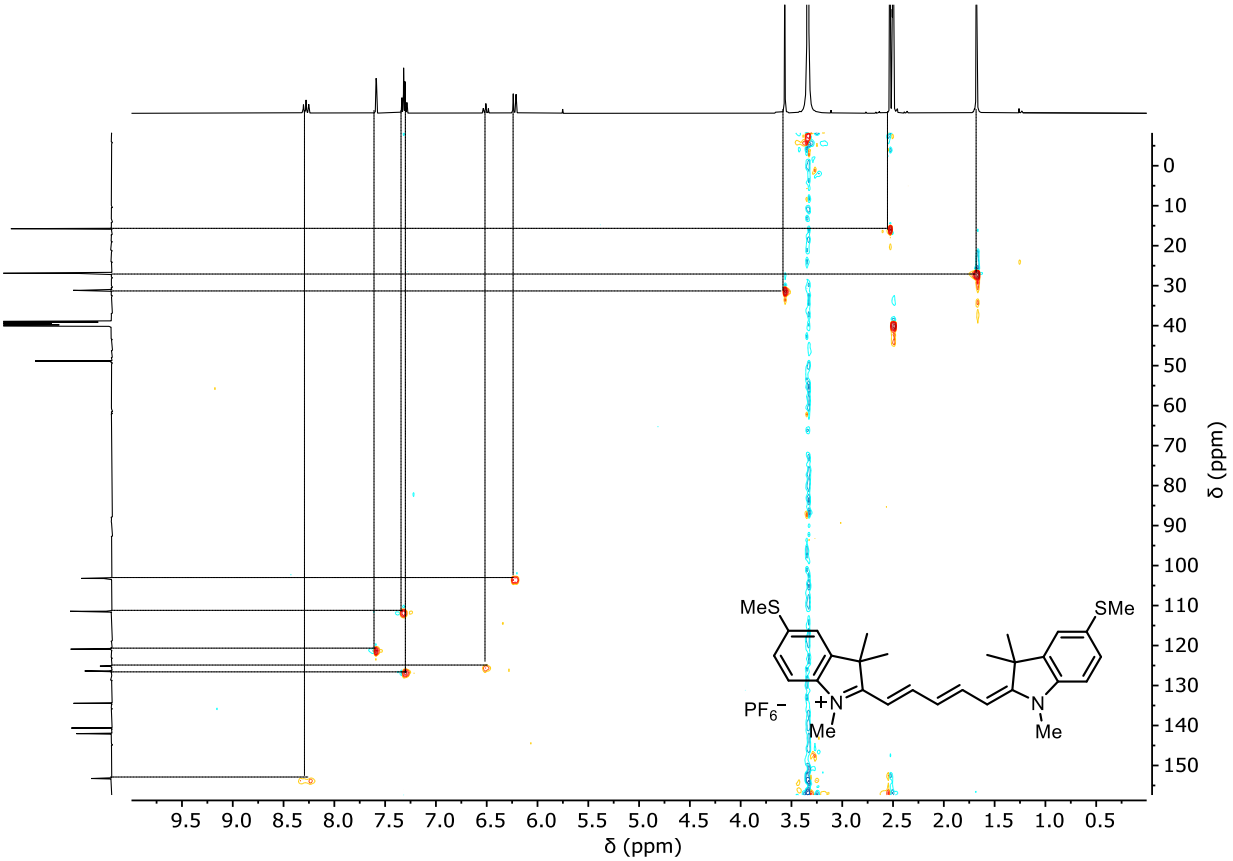

Figure S60. ^{13}C-^{1}H HSQC NMR spectrum of **Cy5·PF$_6$** (d_6-DMSO, 125 MHz, 298 K).

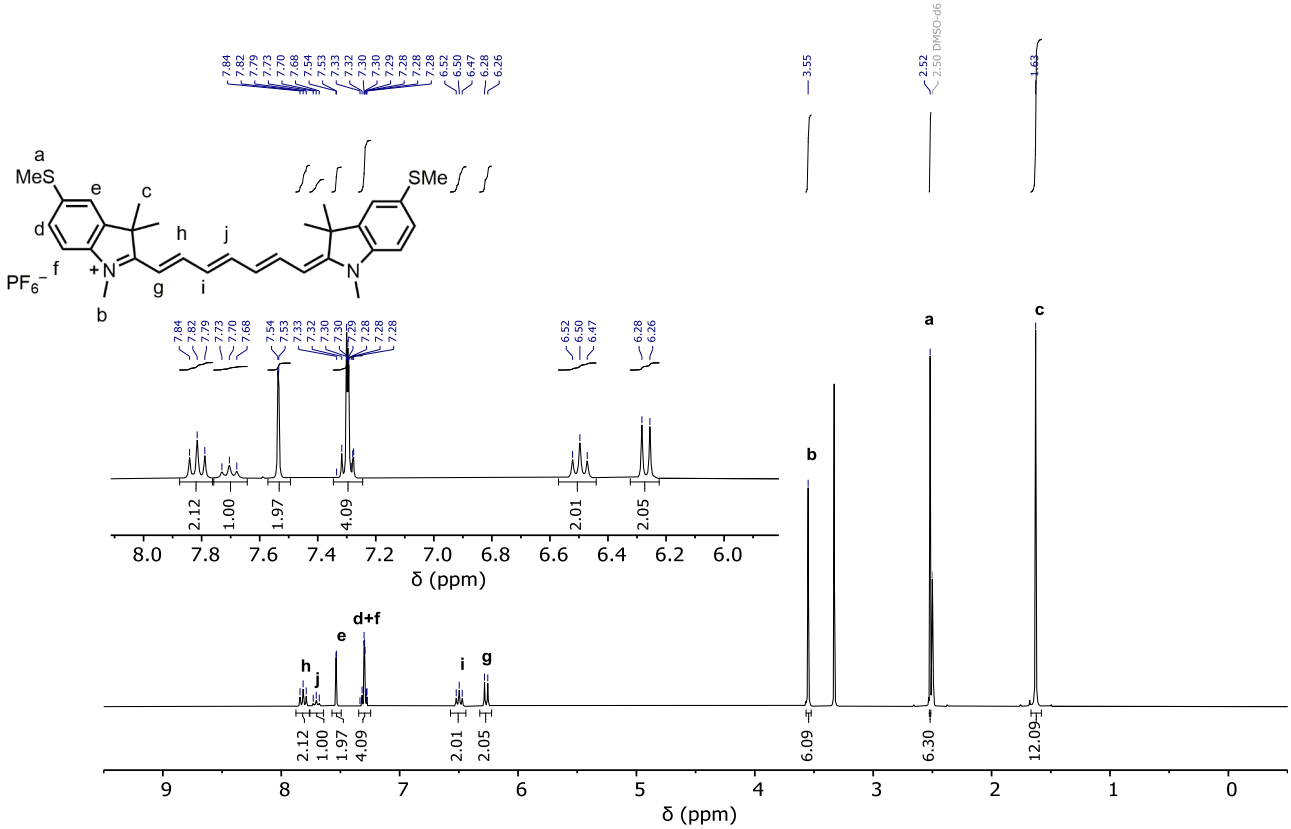

Figure S61. ^{1}H NMR spectrum of **Cy7·PF$_6$** (d_6-DMSO, 500 MHz, 298 K).

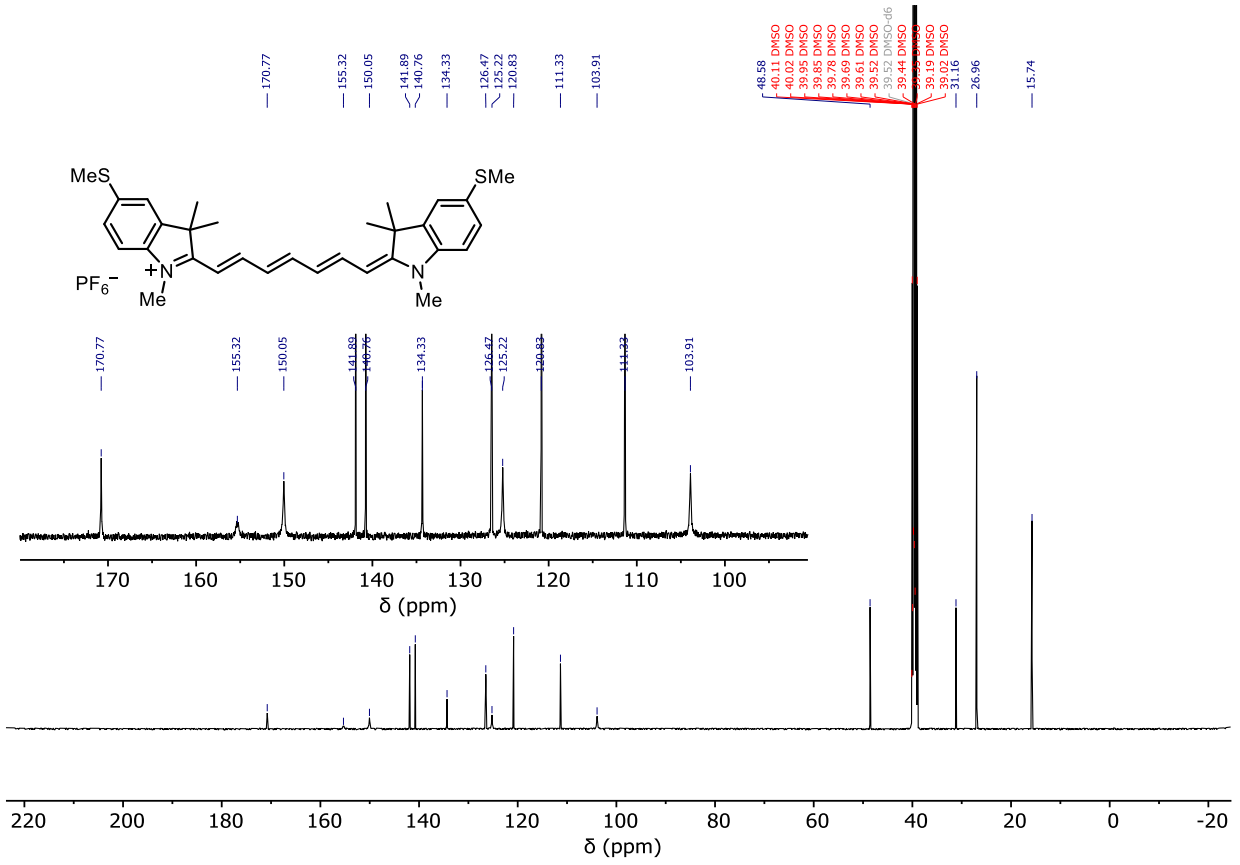

Figure S62. ^{13}C NMR spectrum of **Cy7·PF$_6$** (d_6-DMSO, 125 MHz, 298 K).

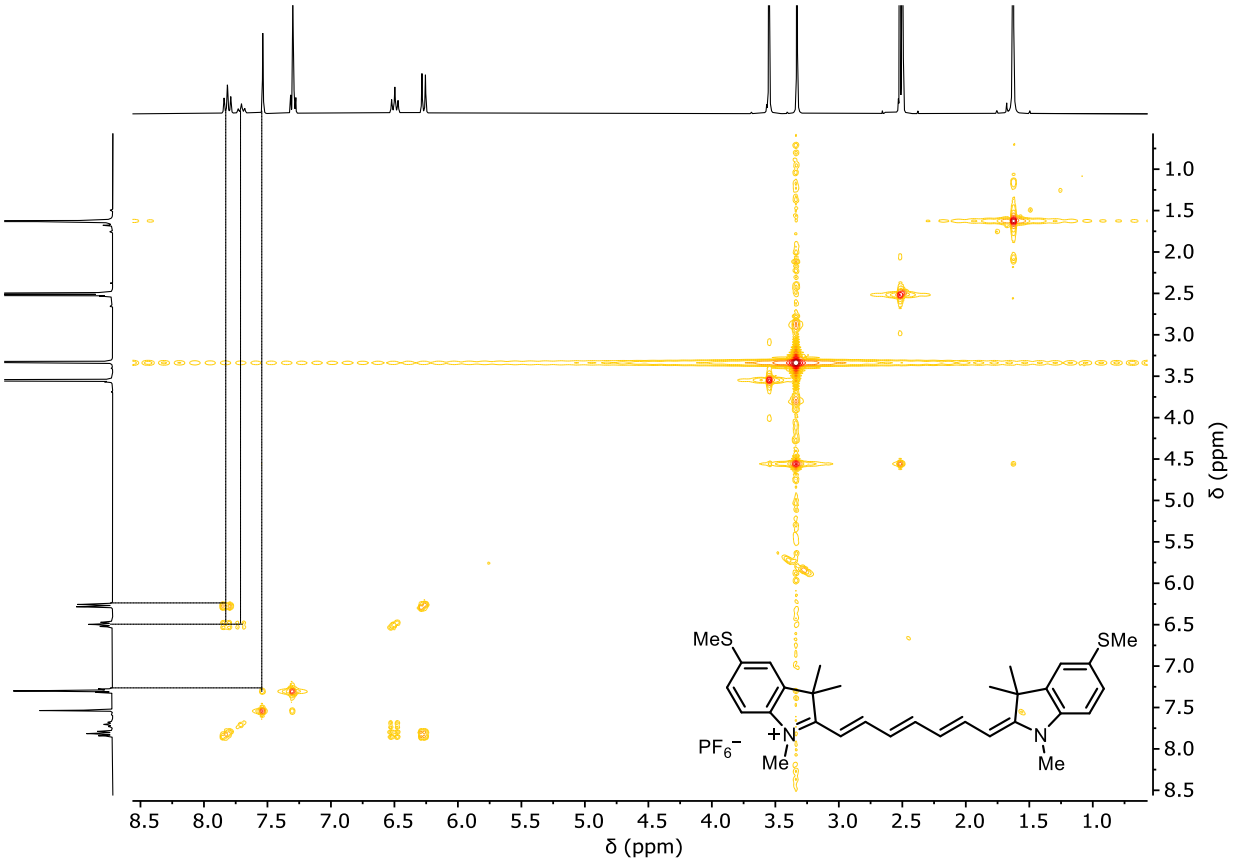

Figure S63. ^{1}H-^{1}H COSY NMR spectrum of **Cy7·PF$_6$** (d_6-DMSO, 500 MHz, 298 K).

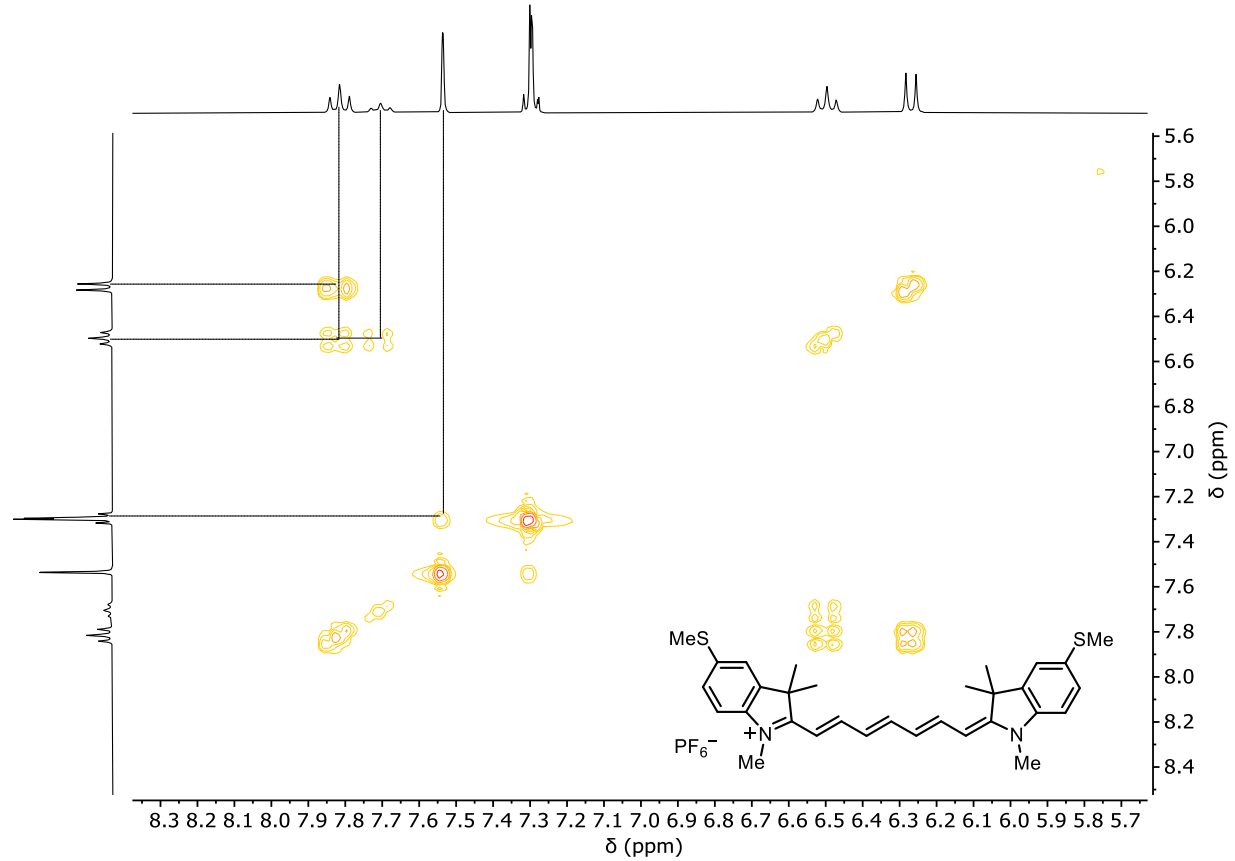

Figure S64. ^{1}H-^{1}H COSY NMR spectrum of **Cy7·PF$_6$** with zoom-in (d_6-DMSO, 500 MHz, 298 K).

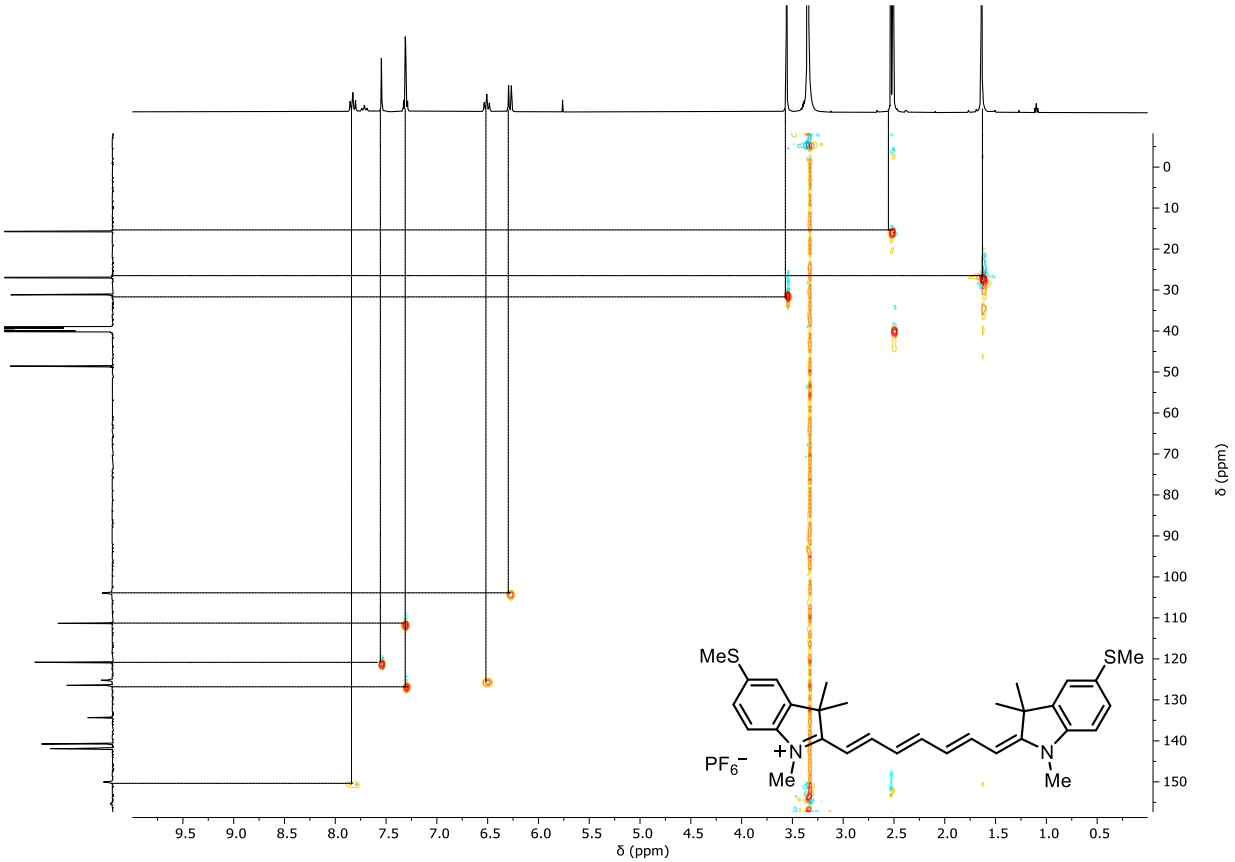

Figure S65. ^{13}C-^{1}H HSQC NMR spectrum of **Cy7·PF$_6$** (d_6-DMSO, 125 MHz, 298 K).

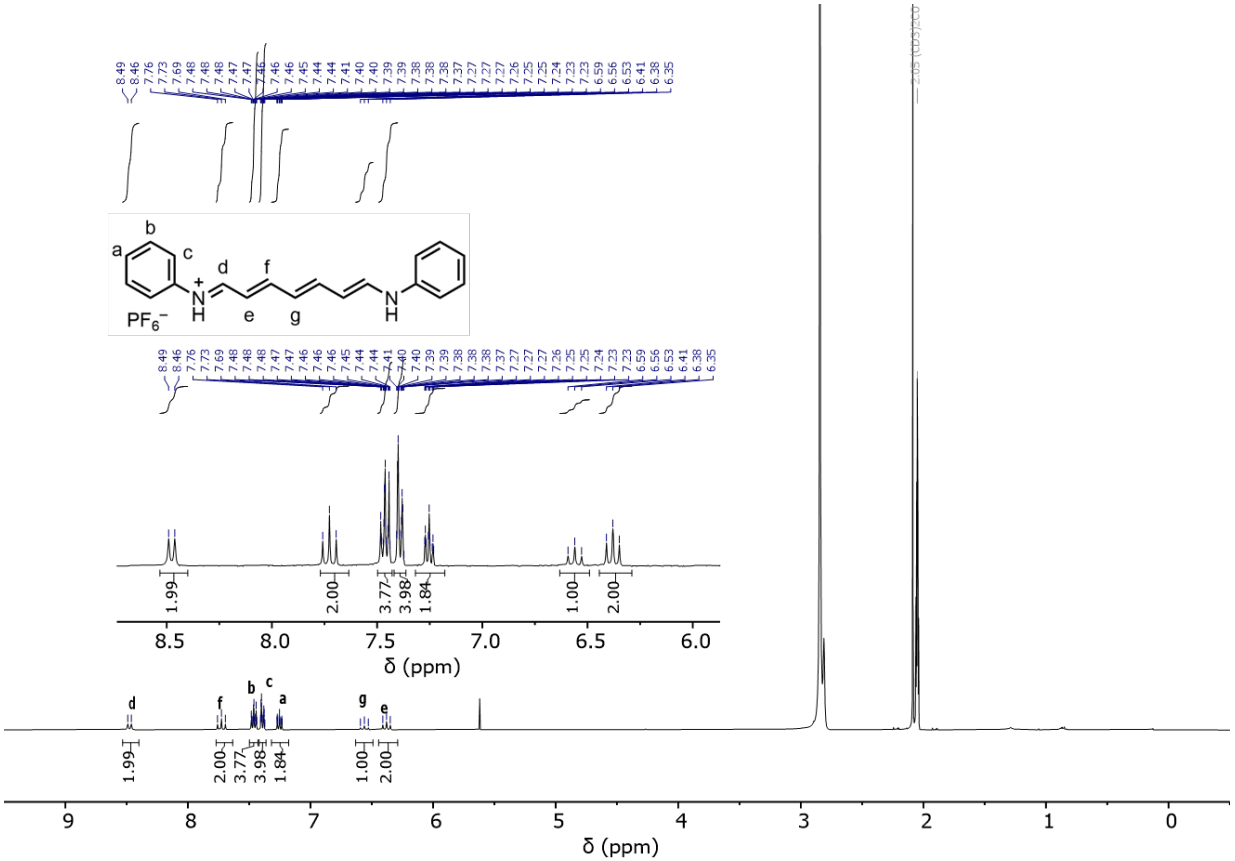

Figure S66. ^{1}H NMR spectrum of **S3** (d_6-acetone, 500 MHz, 298 K).

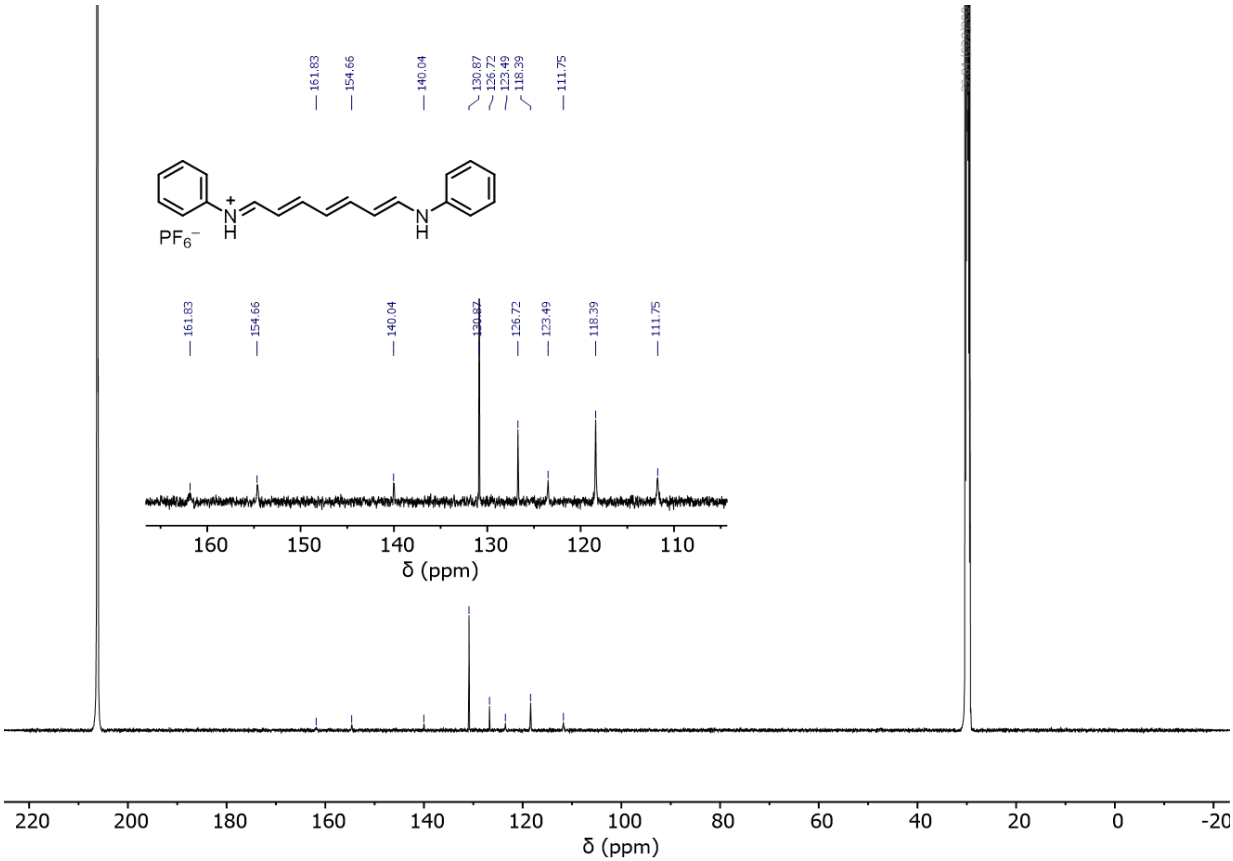

Figure S67. ^{13}C NMR spectrum of **S3** (d_6-acetone, 125 MHz, 298 K).

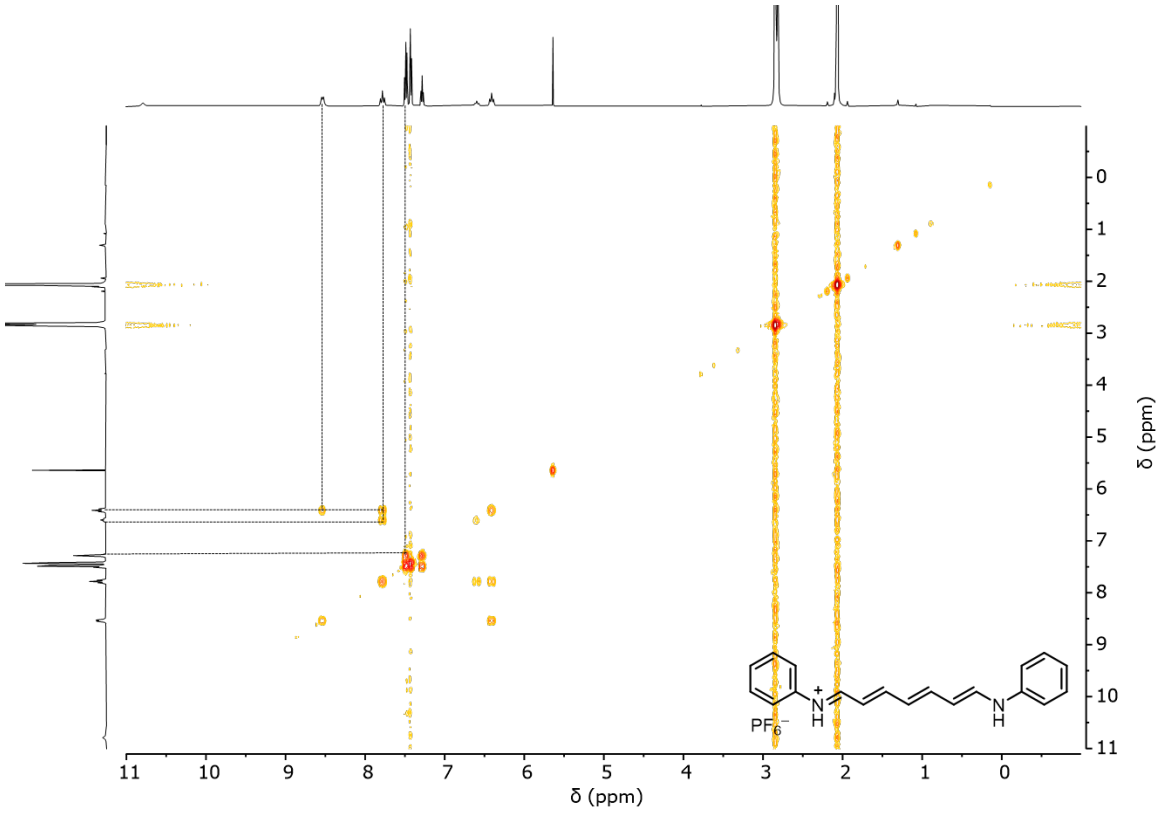

Figure S68. ^{1}H-^{1}H COSY NMR spectrum of **S3** (d_6-acetone, 500 MHz, 298 K).

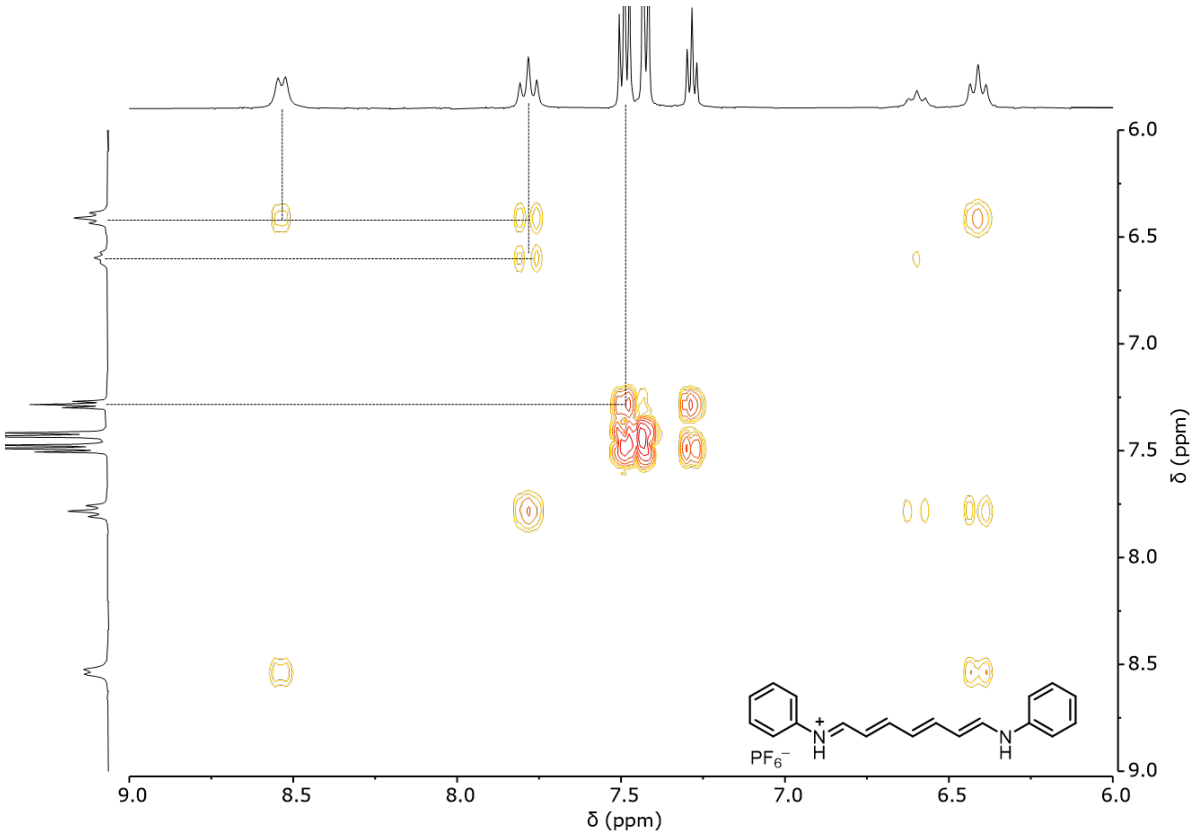

Figure S69. ^{1}H-^{1}H COSY NMR spectrum of **S3** with zoom-in (d_6-acetone, 500 MHz, 298K).

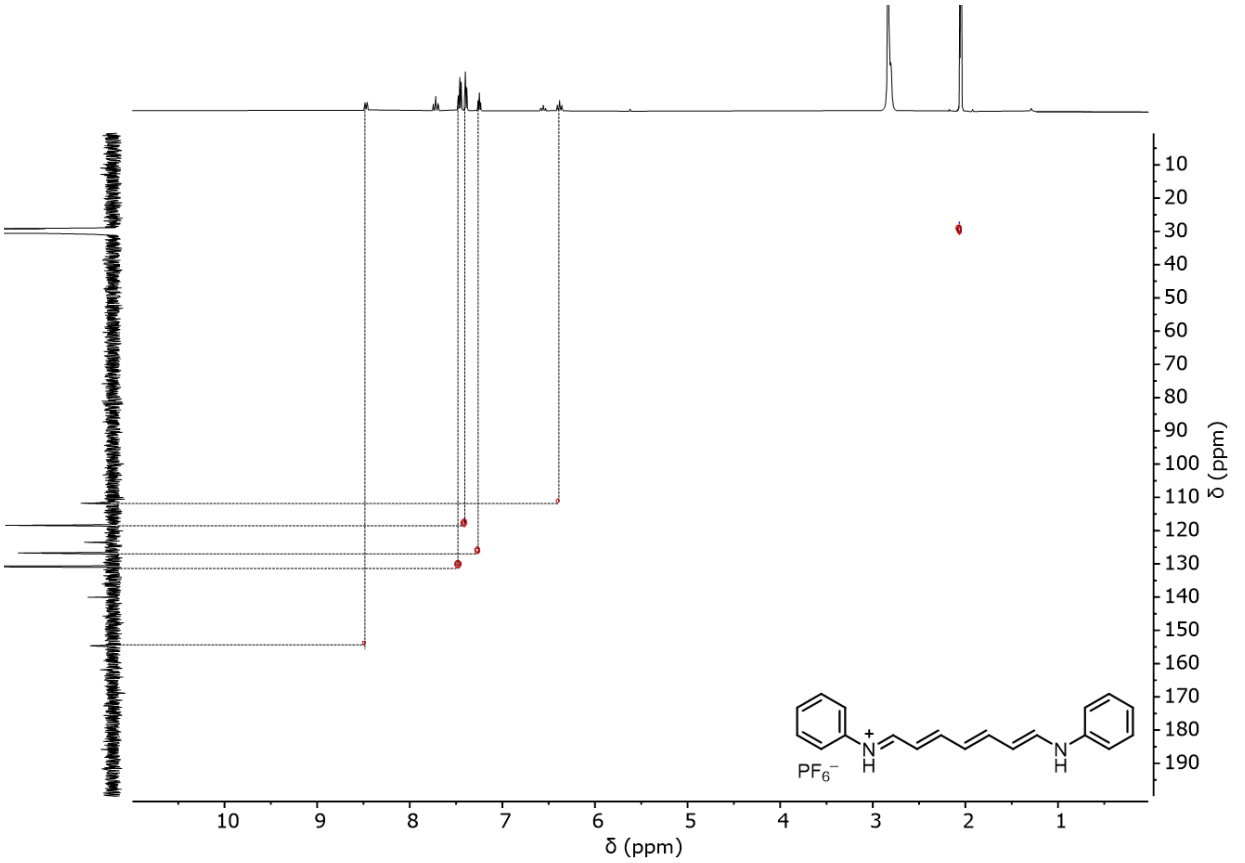

Figure S70. ^{13}C-^{1}H HSQC NMR spectrum of **S3** (d_6-DMSO, 125 MHz, 298 K).

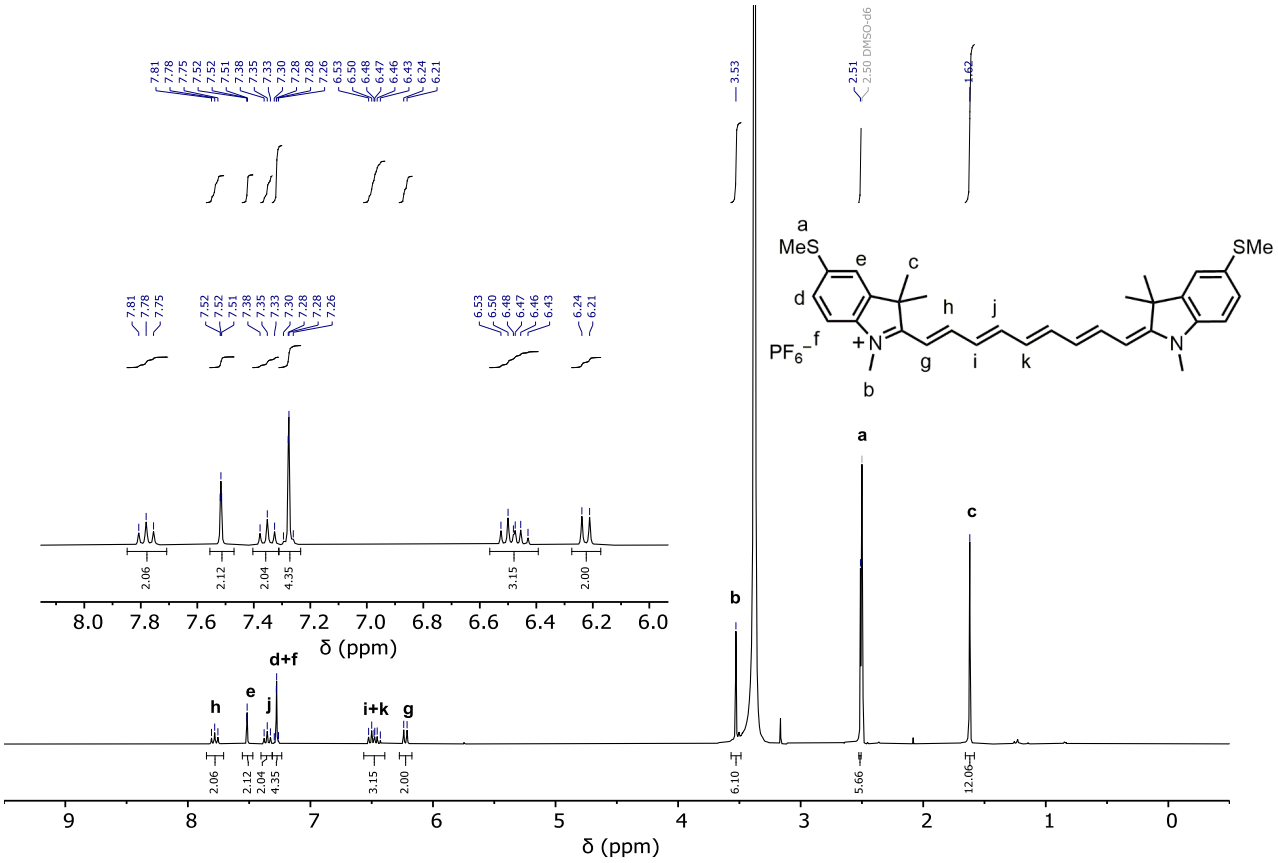

Figure S71. ^{1}H NMR spectra of **Cy9·PF$_6$** (d_6-DMSO, 500 MHz, 298 K).

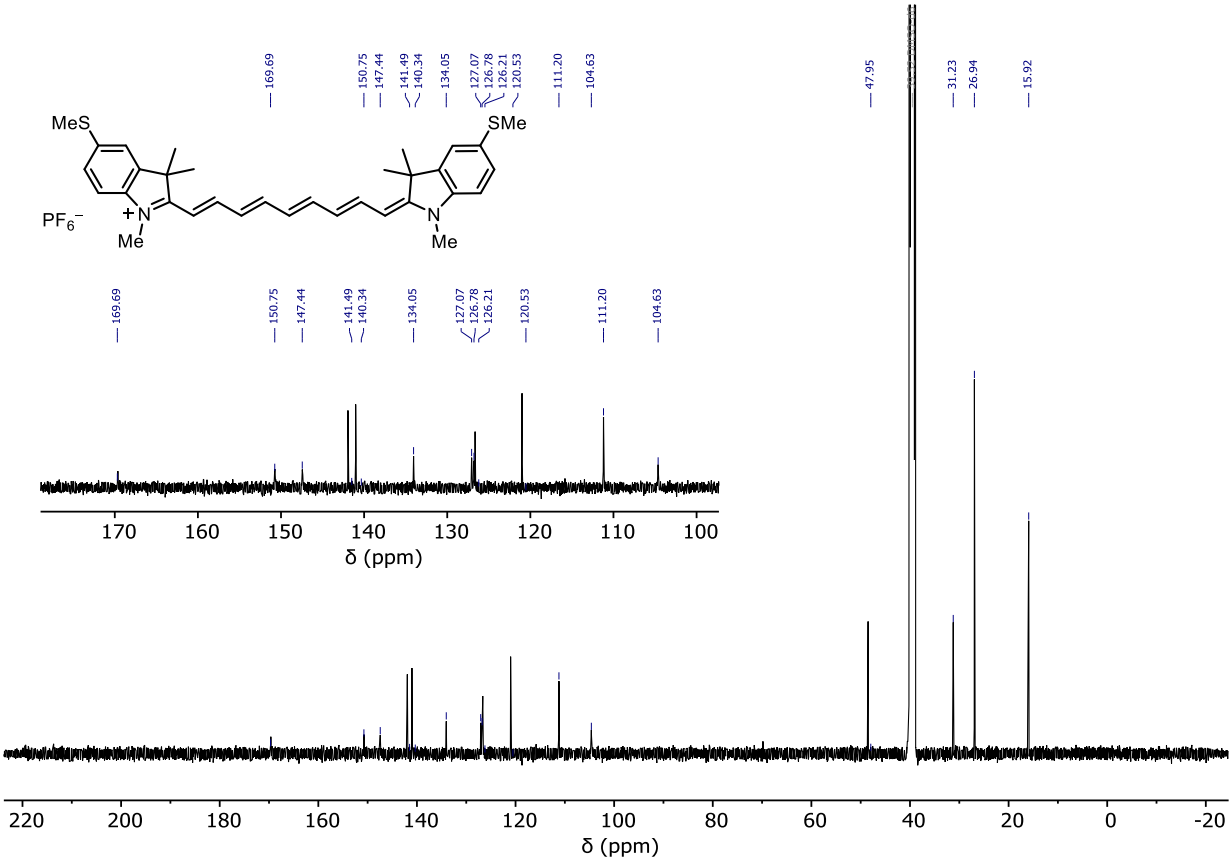

Figure S72. ^{13}C NMR spectra of **Cy9·PF$_6$** (d_6-DMSO, 125 MHz, 298 K).

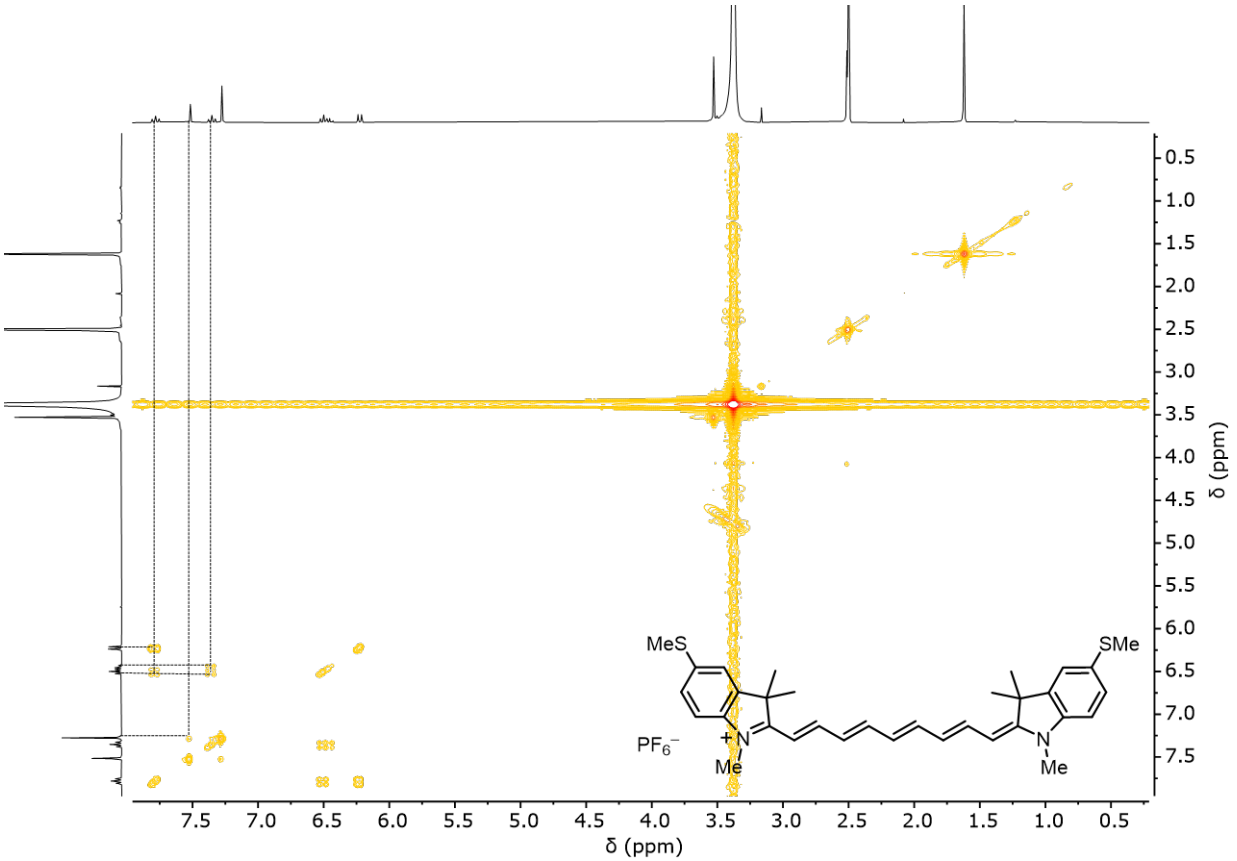

Figure S73. ^{1}H-^{1}H COSY NMR spectrum of **Cy9·PF$_6$** (d_6-DMSO, 500 MHz, 298 K).

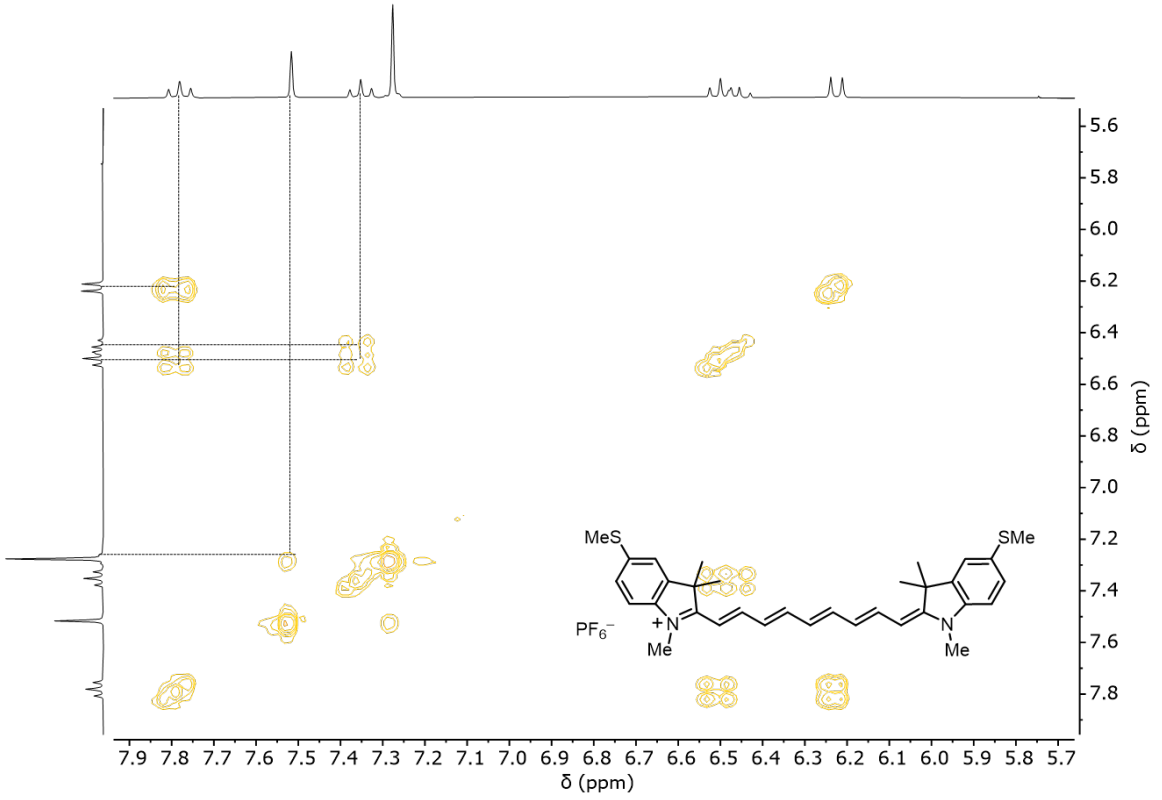

Figure S74. ^{1}H-^{1}H COSY NMR spectrum of **Cy9·PF$_6$**, zoom-in (d_6-DMSO, 500 MHz, 298 K).

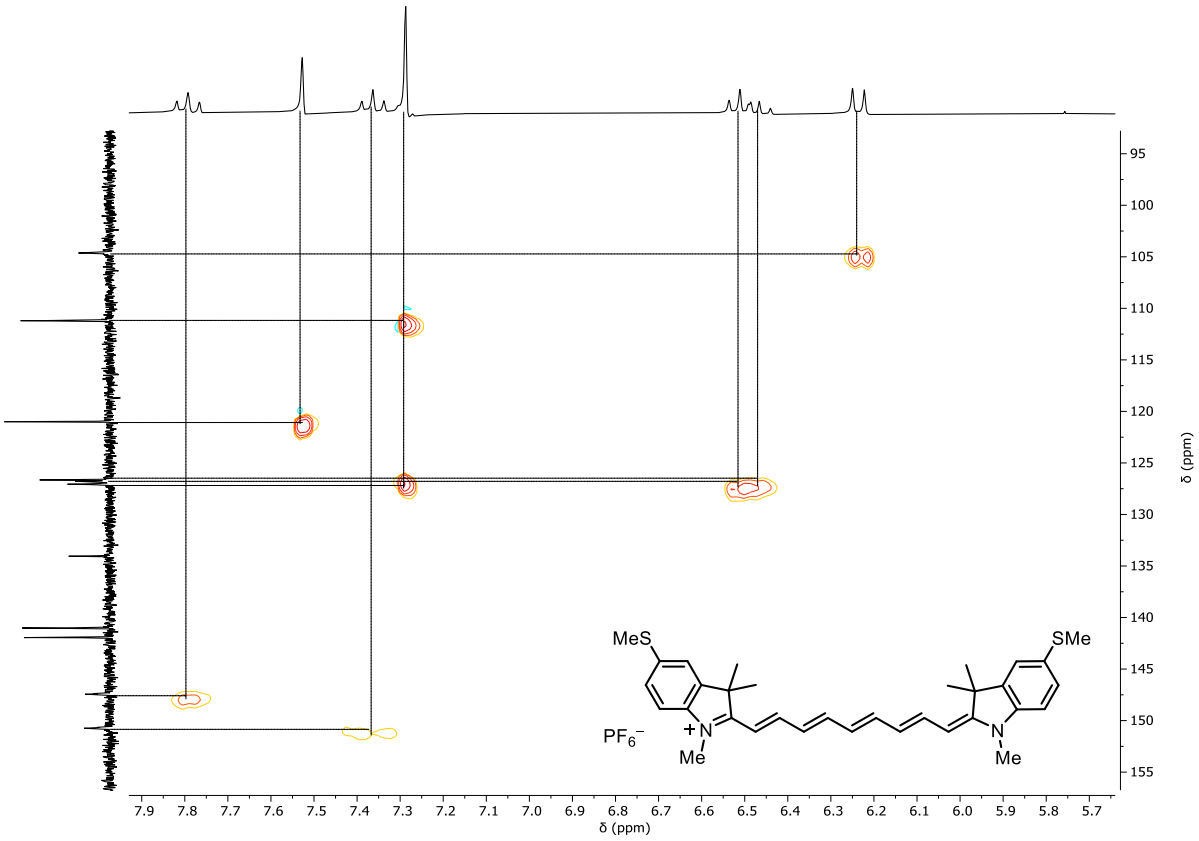

Figure S75. ^{13}C-^{1}H HSQC NMR spectrum of **Cy9·PF$_6$**, zoom-in (d_6-DMSO, 125 MHz, 298 K).

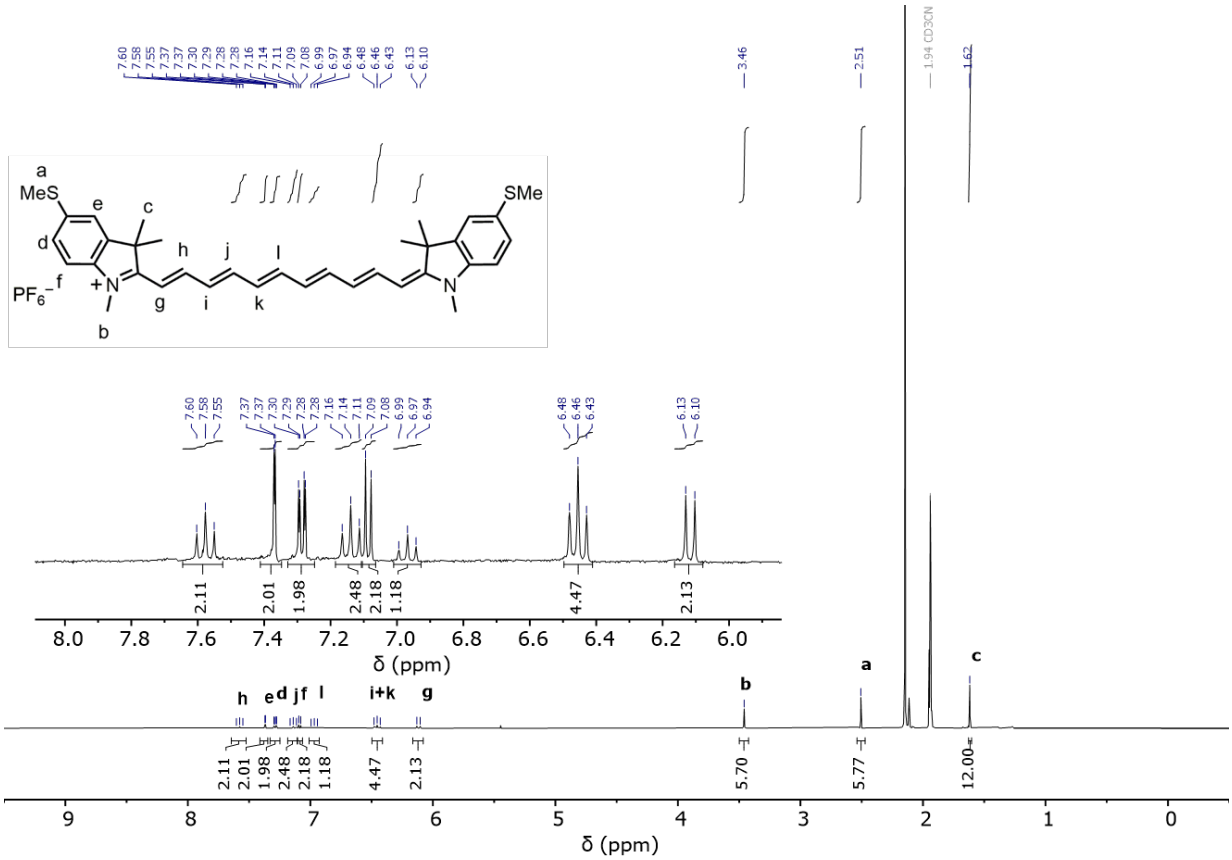

Figure S76. ^{1}H NMR spectra of **Cy11·PF$_6$** (d_3-CH$_3$CN, 500 MHz, 298 K).

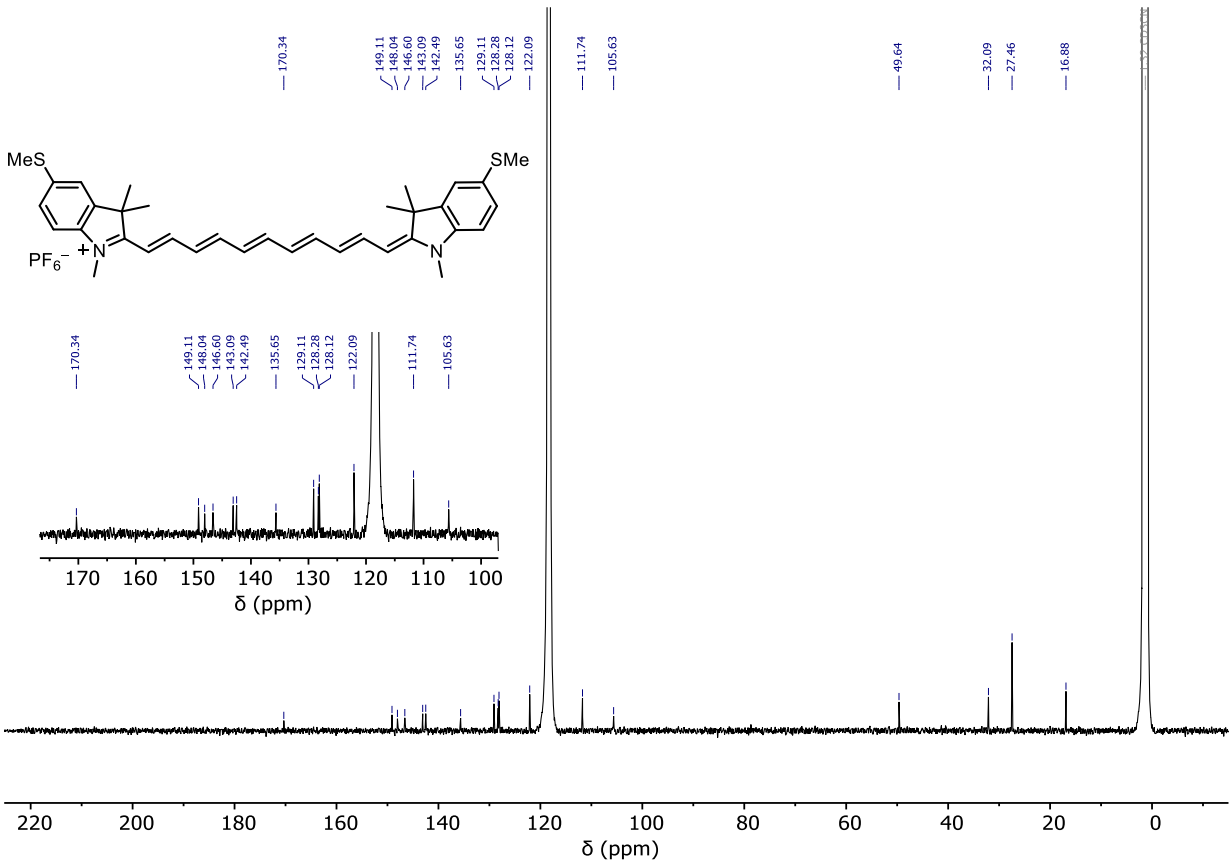

Figure S77. ^{13}C NMR spectrum of **Cy11·PF$_6$** (d_3-CH$_3$CN, 125 MHz, 298 K).

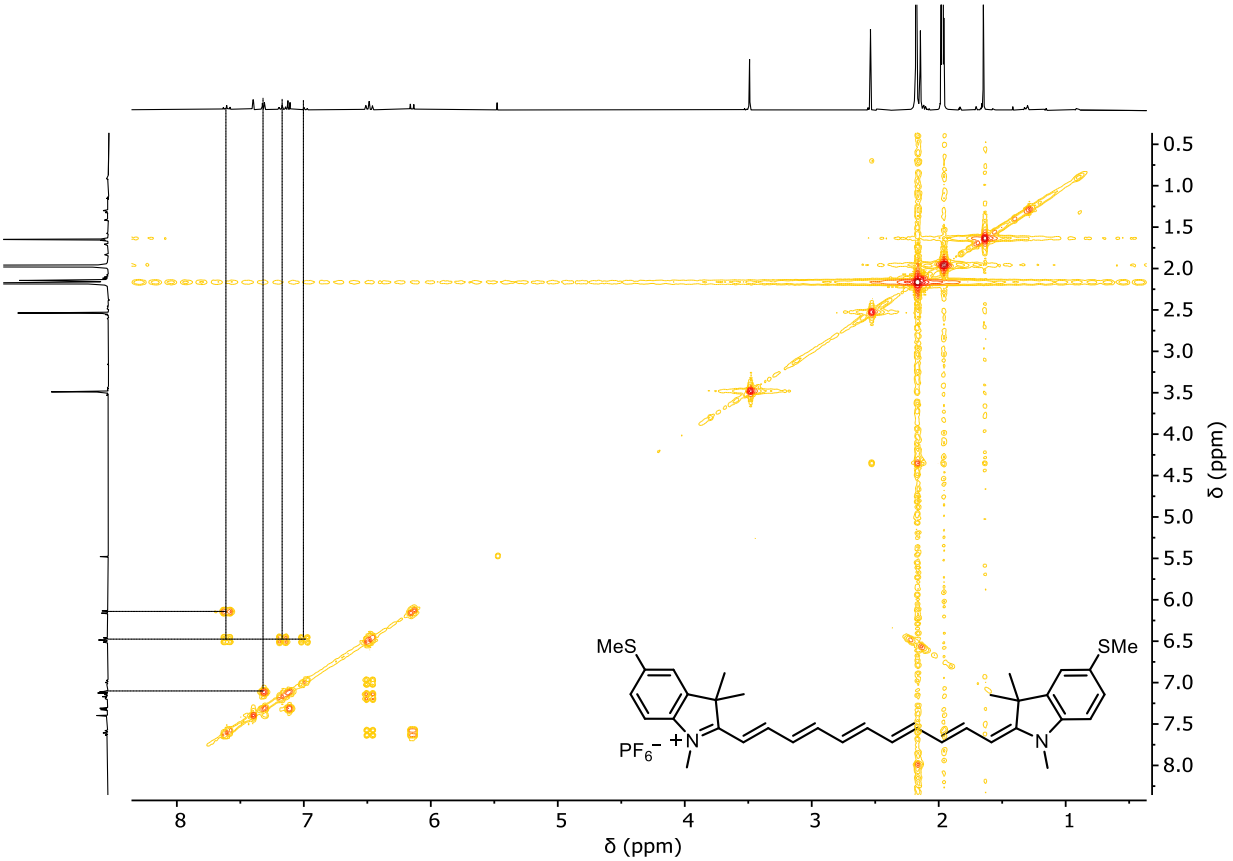

Figure S78. ^{1}H-^{1}H COSY NMR spectrum of **Cy11·PF$_6$** (d_3-CH$_3$CN, 500 MHz, 298 K).

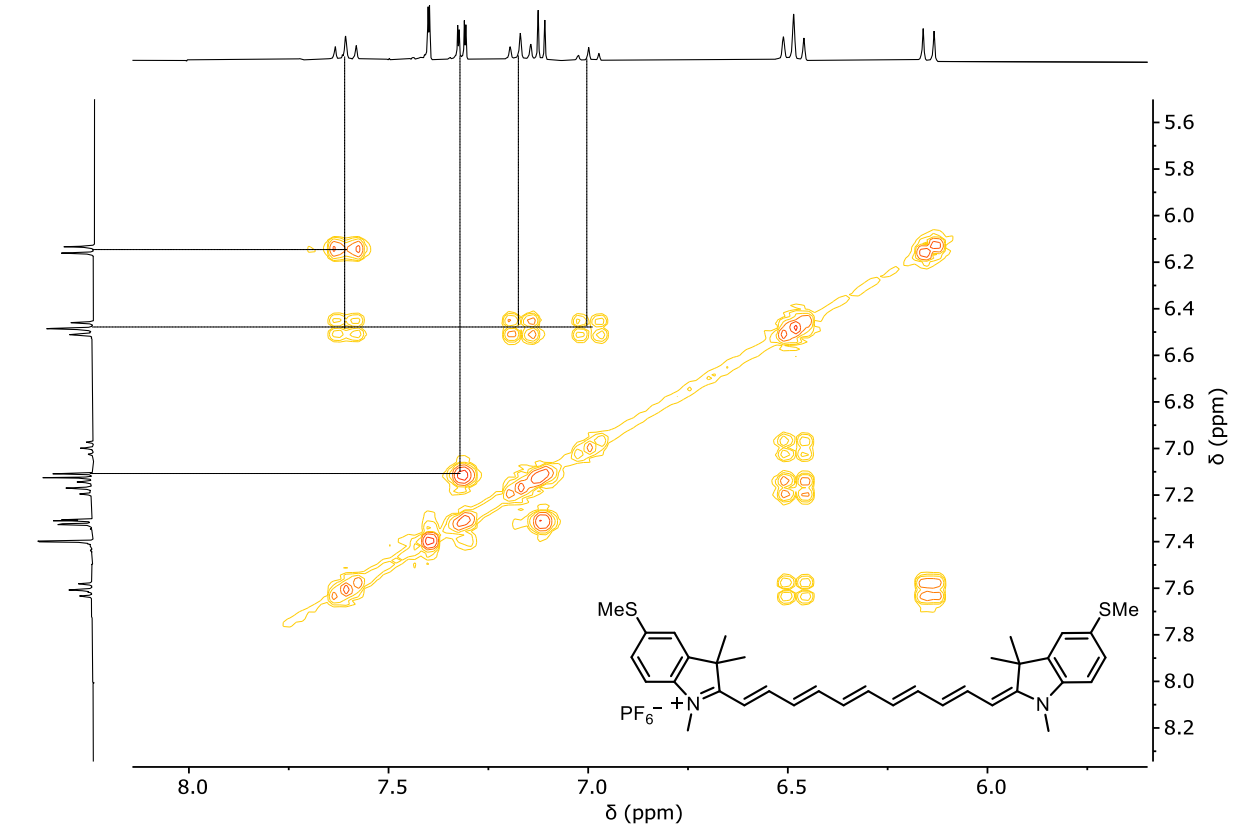

Figure S79. ^{1}H-^{1}H COSY NMR spectrum of **Cy11·PF$_6$** with zoom-in (d_3-CH$_3$CN, 500 MHz, 298K).

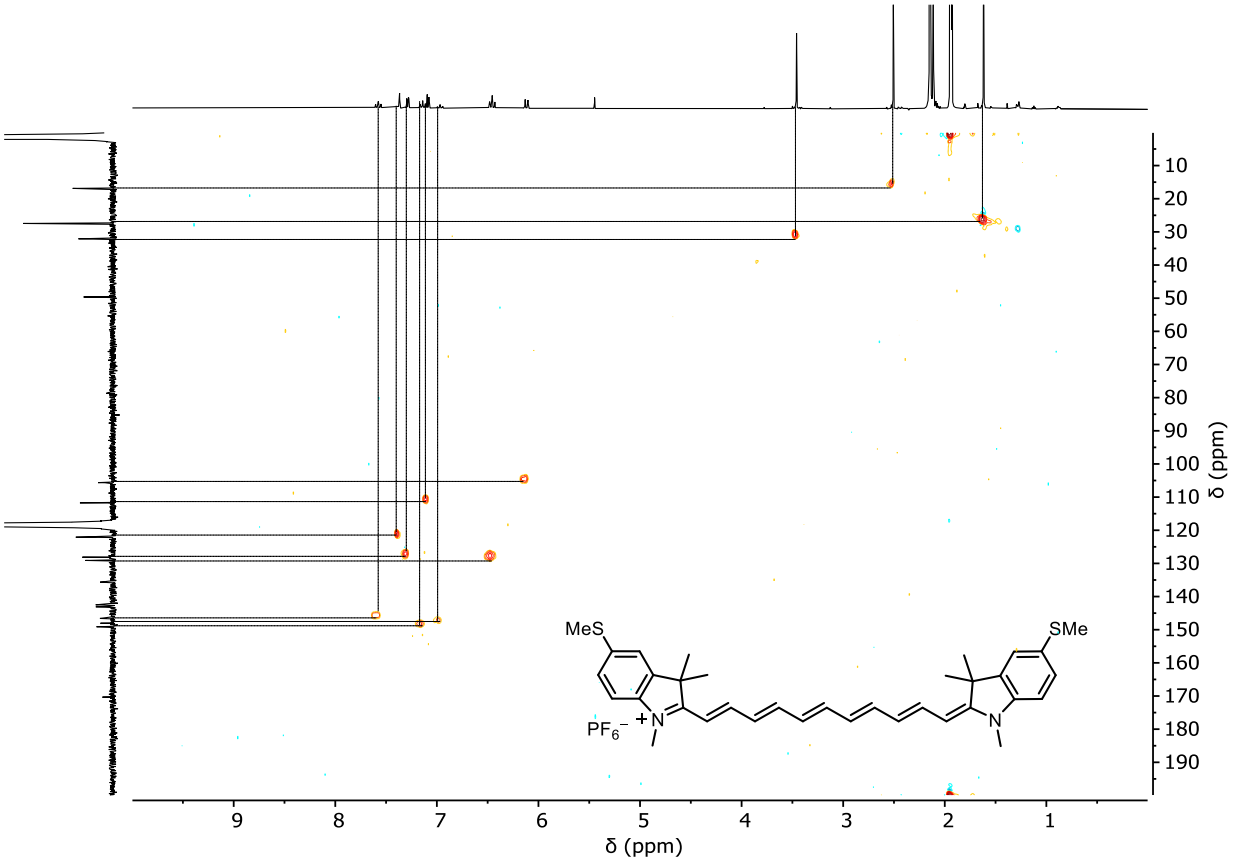

Figure S80. ^{13}C-^{1}H HSQC NMR spectrum of **Cy11·PF$_6$** (d_3-CH$_3$CN, 125 MHz, 298 K).

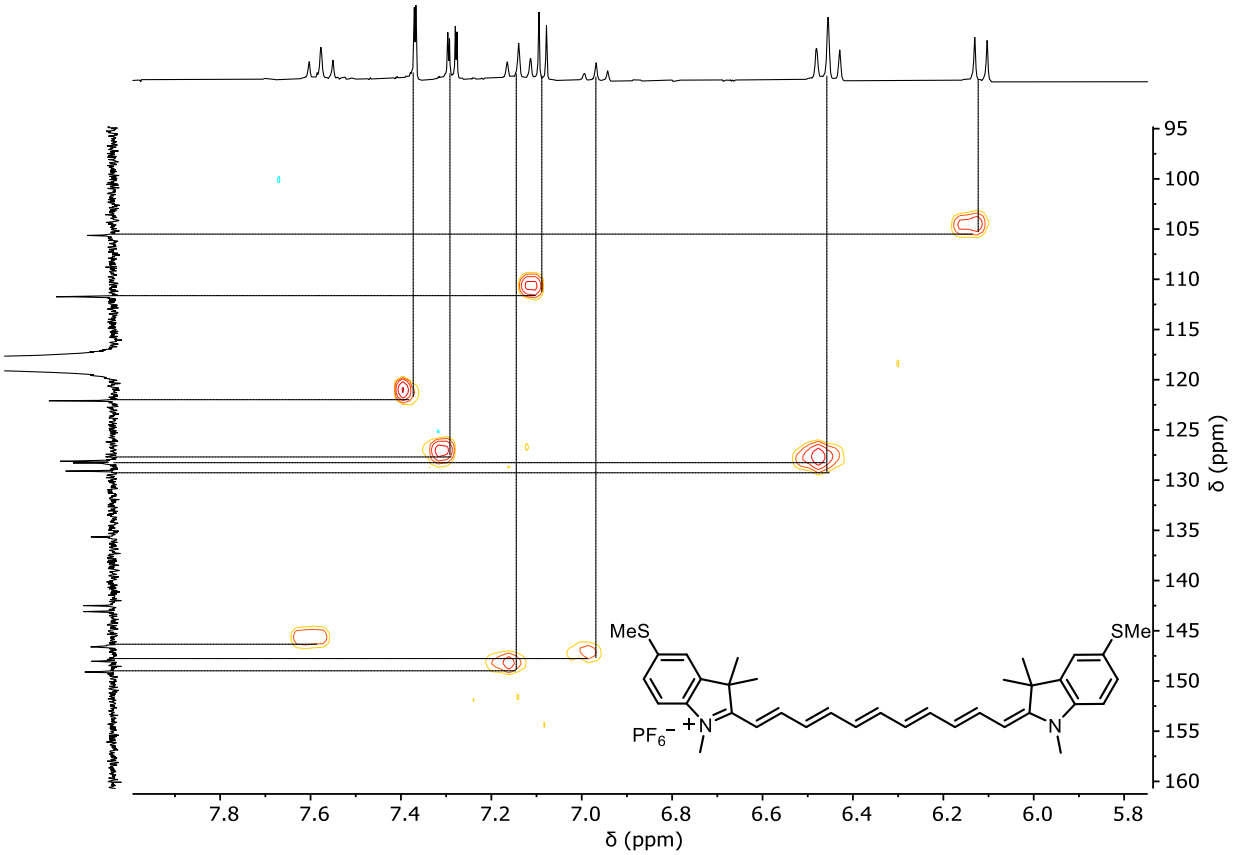

Figure S81. ^{13}C-^{1}H HSQC NMR spectrum of **Cy11·PF$_6$**, zoom-in (d_3-CH$_3$CN, 125 MHz, 298 K).

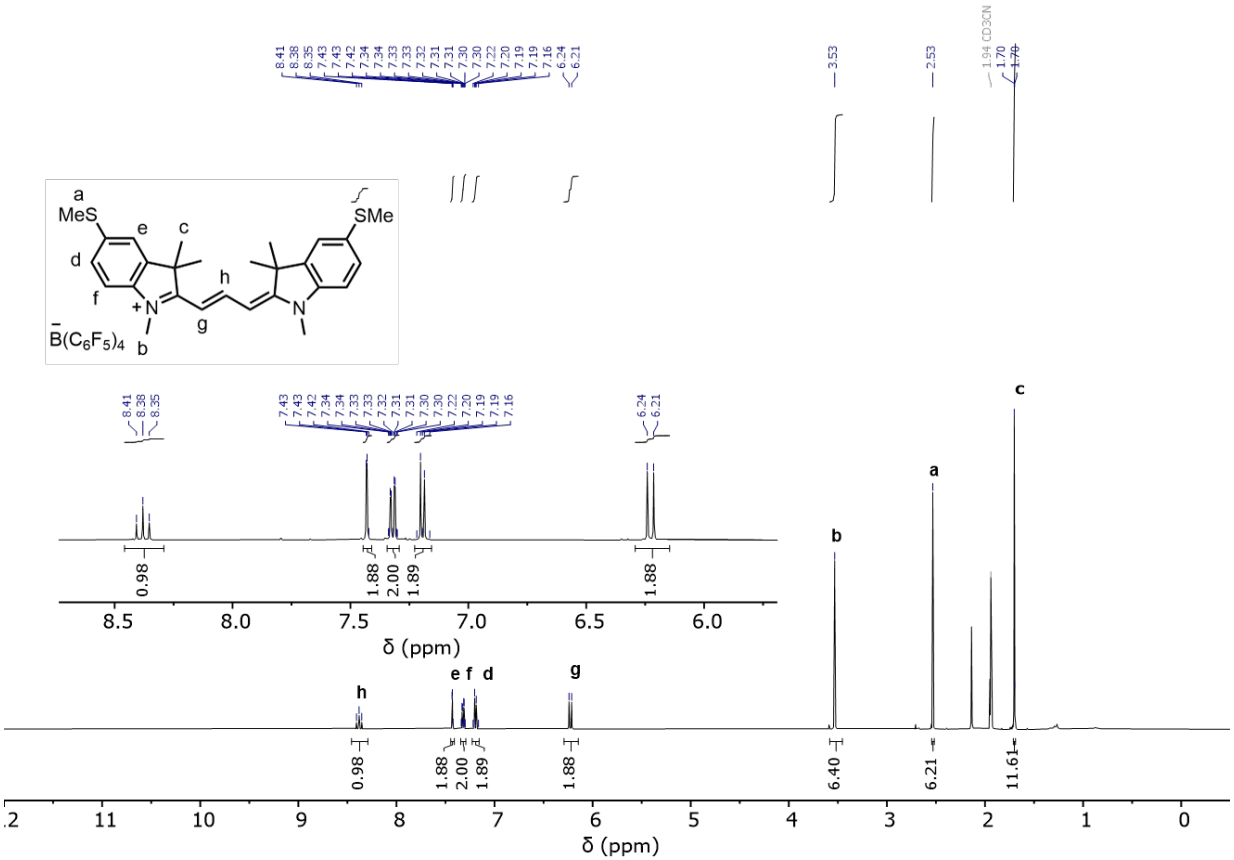

Figure S82. ^{1}H NMR spectrum of **Cy3·B(C$_6$F$_5$)$_4$** (d_3-CH$_3$CN, 500 MHz, 298 K).

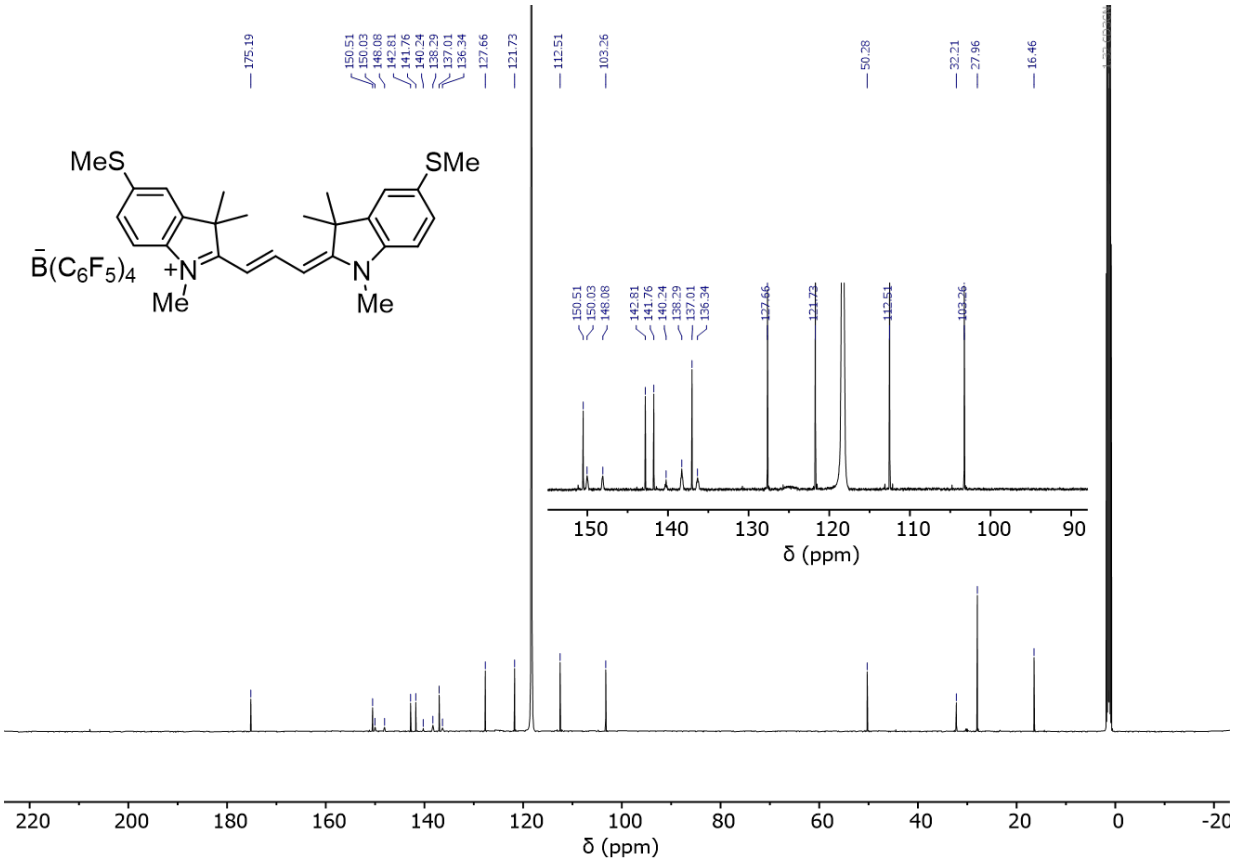

Figure S83. ^{13}C NMR spectrum of **Cy3·B(C$_6$F$_5$)$_4$** (d_3-CH$_3$CN, 125 MHz, 298 K).

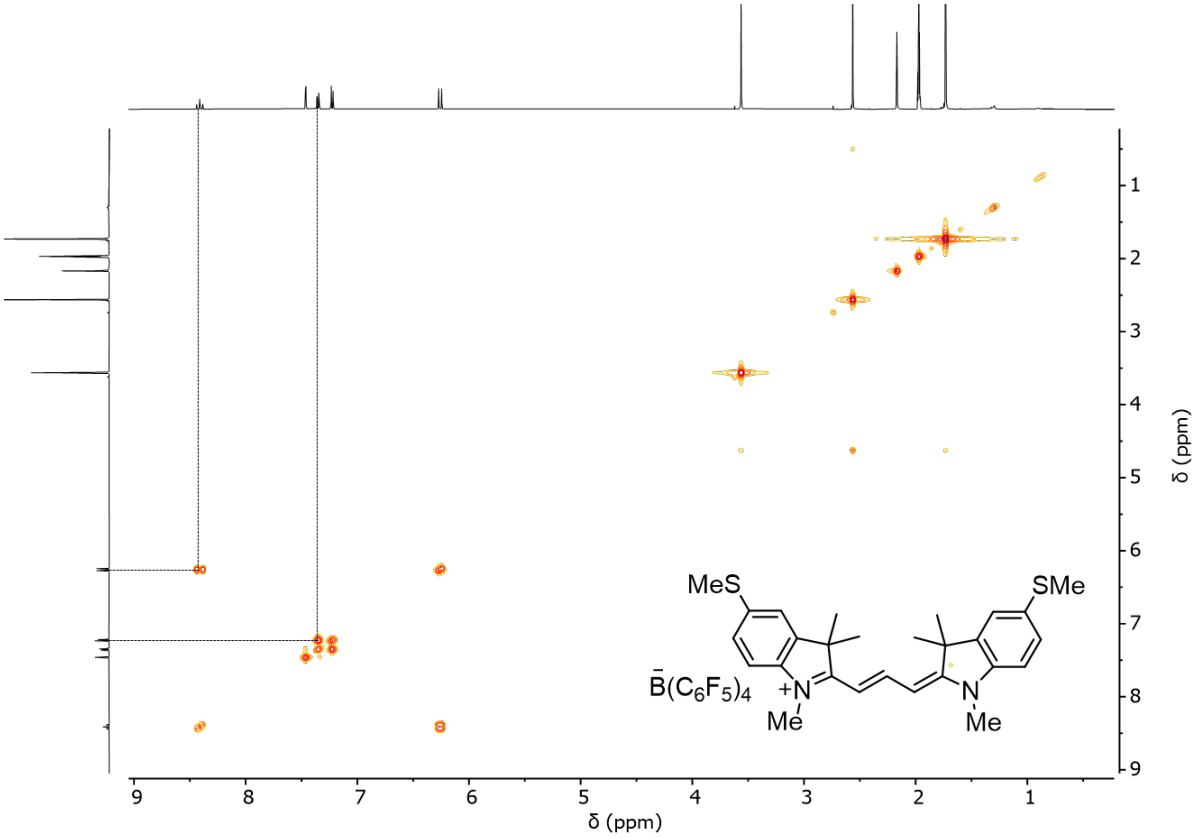

Figure S84. ^{1}H-^{1}H COSY NMR spectrum of **Cy3·B(C$_6$F$_5$)$_4$** (d_3-CH$_3$CN, 500 MHz, 298 K).

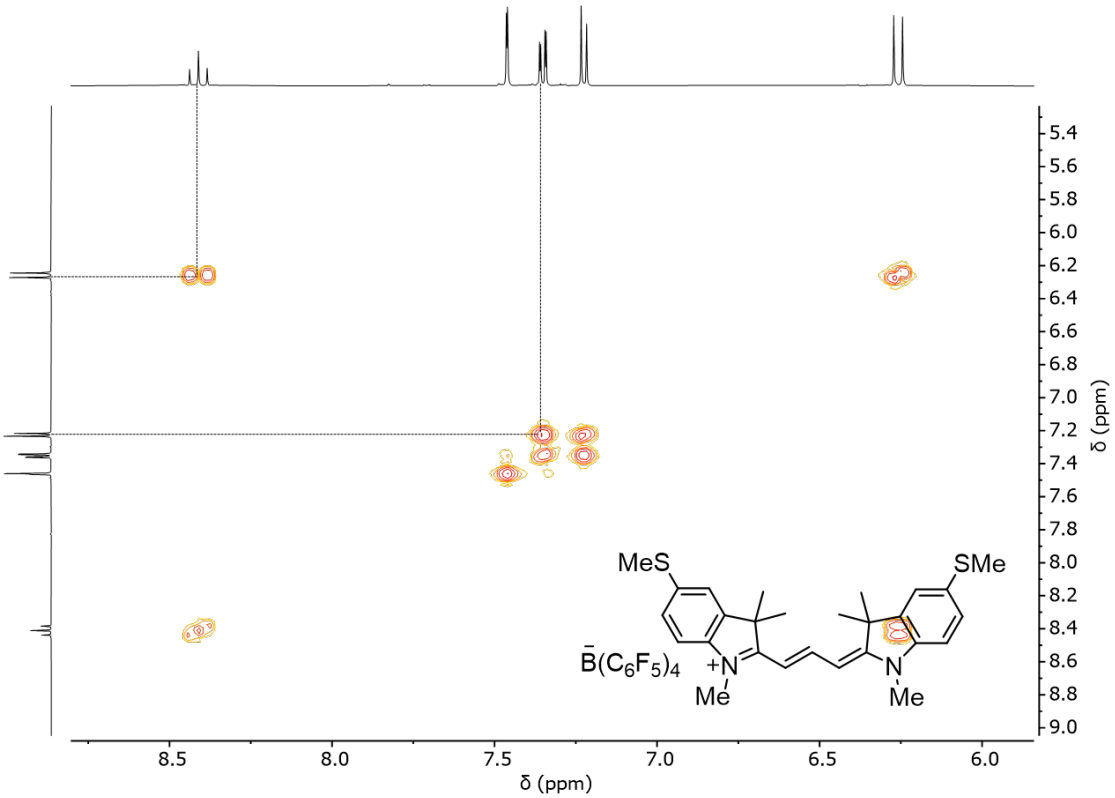

Figure S85. ^{1}H-^{1}H COSY NMR spectrum of **Cy3·B(C$_6$F$_5$)$_4$**, zoom (d_3-CH$_3$CN, 500 MHz, 298 K).

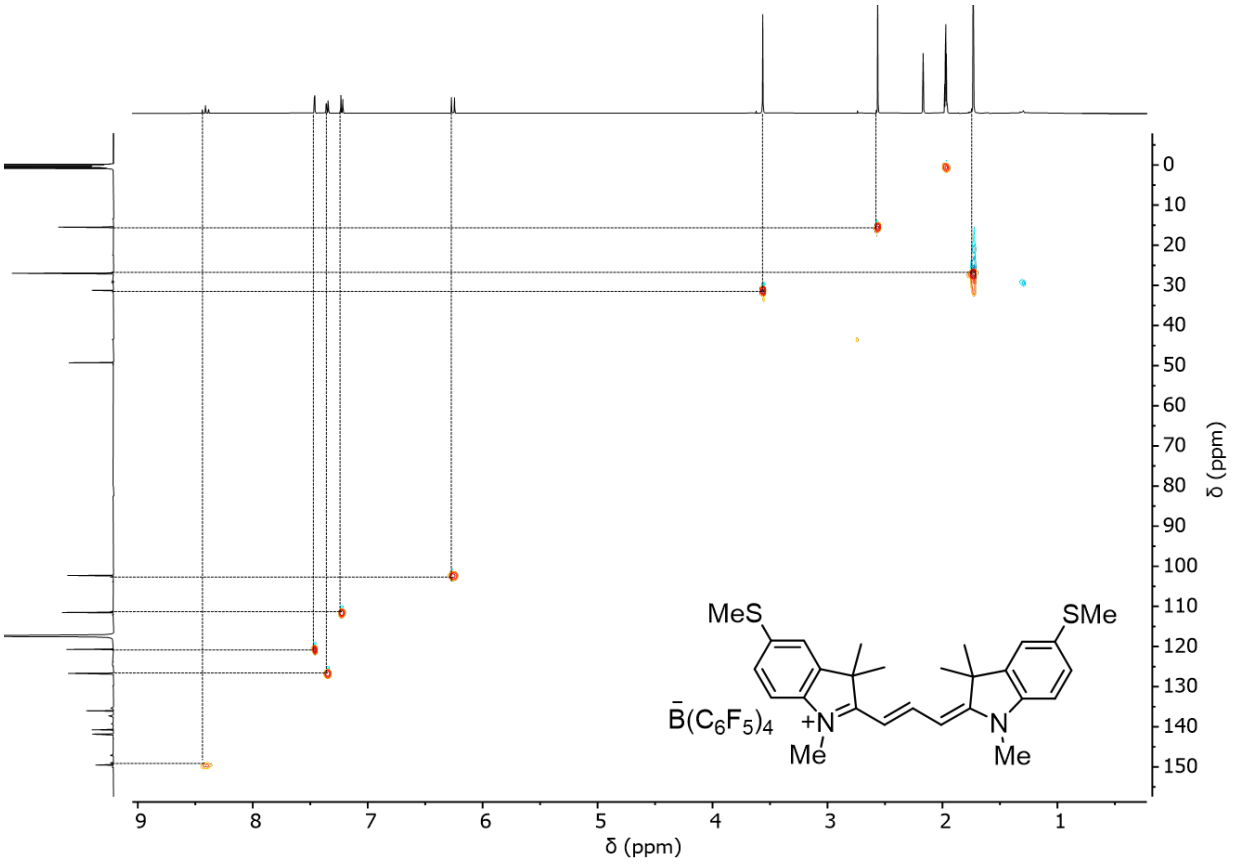

Figure S86. ^{13}C-^{1}H HSQC NMR spectrum of **Cy3·B(C$_6$F$_5$)$_4$** (d_3-CH$_3$CN, 125 MHz, 298 K).

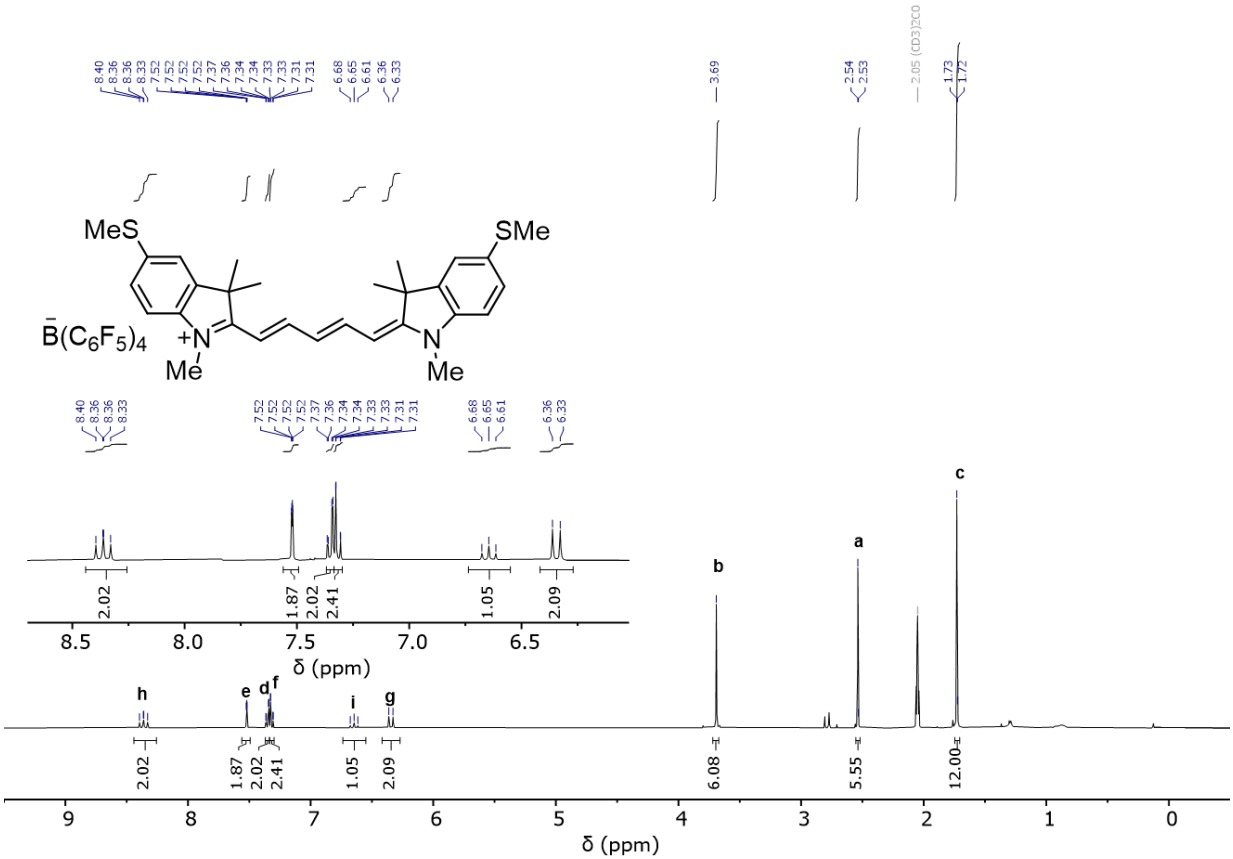

Figure S87. ^{1}H NMR spectrum of **Cy5·B(C$_6$F$_5$)$_4$** (d_6-acetone, 400 MHz, 298 K).

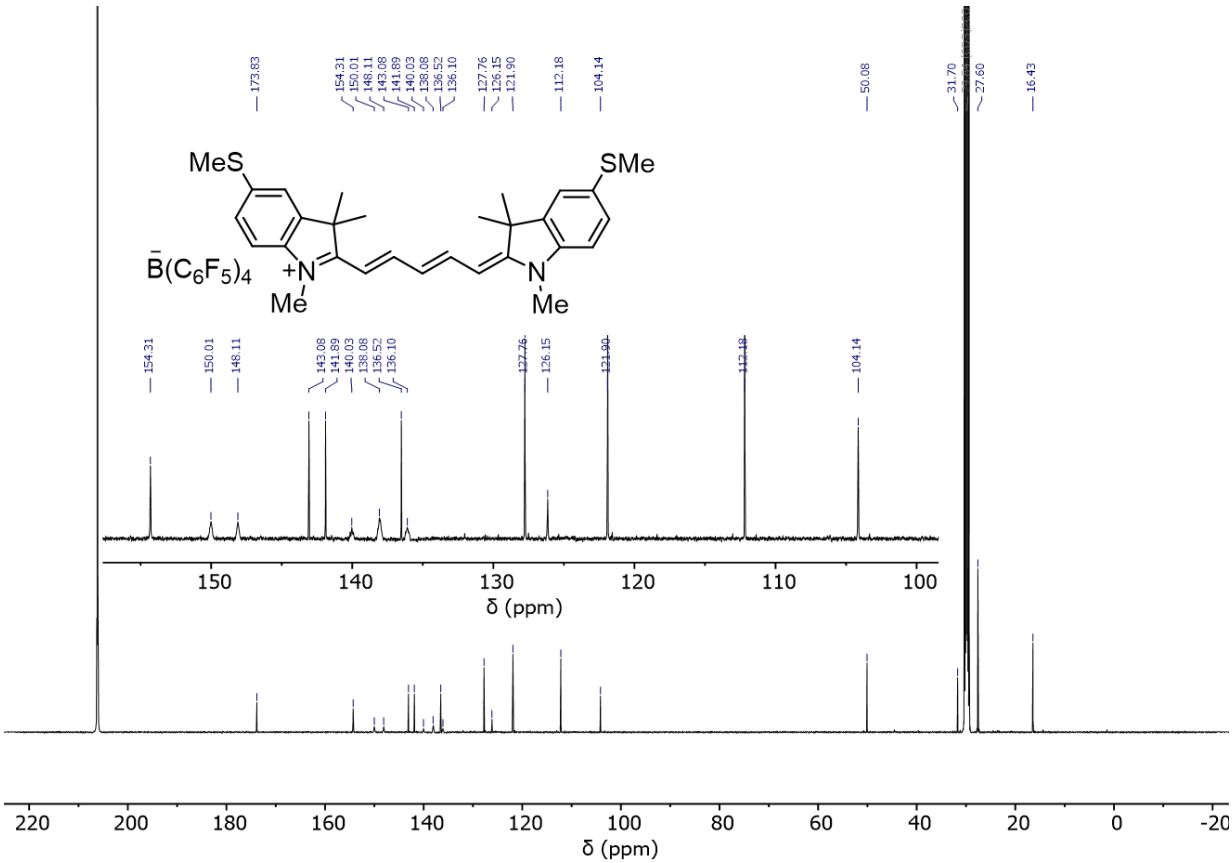

Figure S88. ^{13}C NMR spectrum of **Cy5·B(C$_6$F$_5$)$_4$** (d_6-acetone, 125 MHz, 298 K).

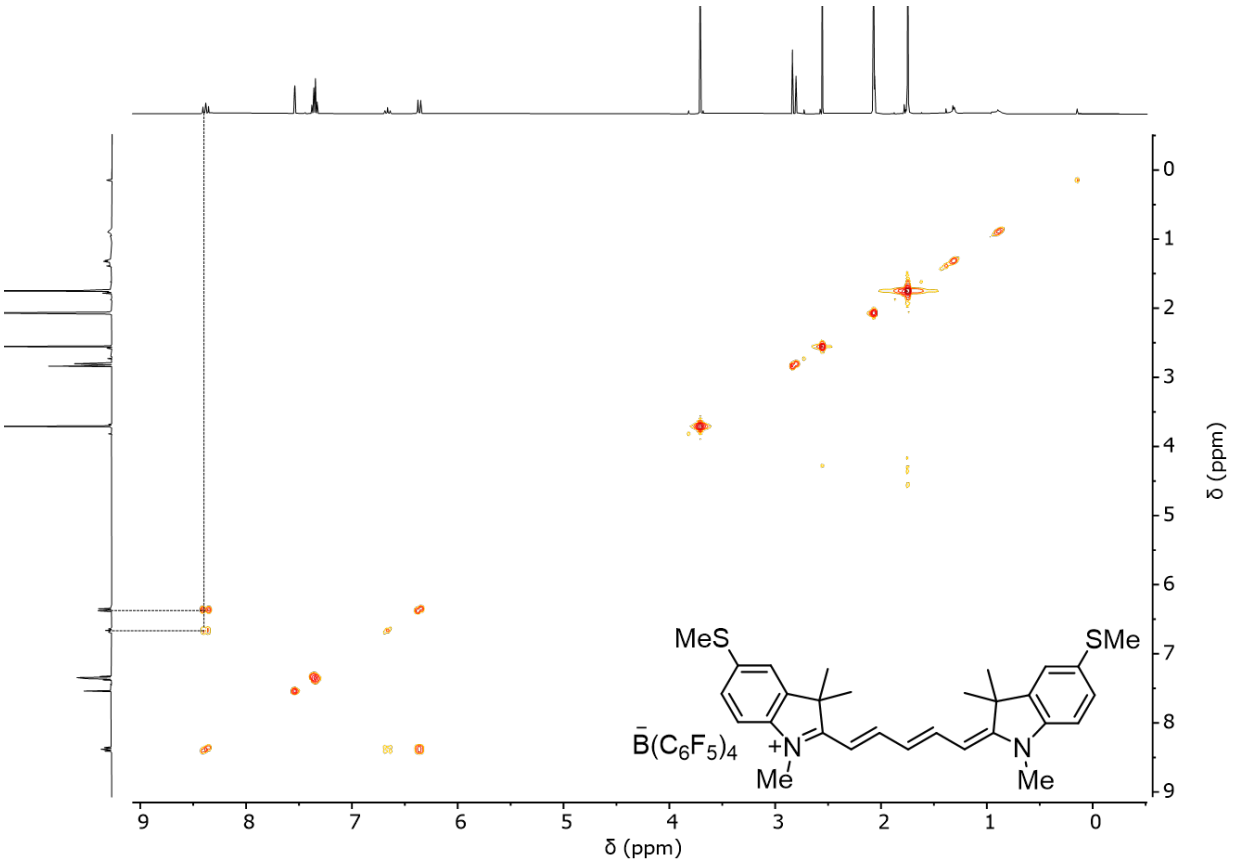

Figure S89. ^{1}H-^{1}H COSY NMR spectrum of **Cy5·B(C$_6$F$_5$)$_4$** (d_6-acetone, 500 MHz, 298 K).

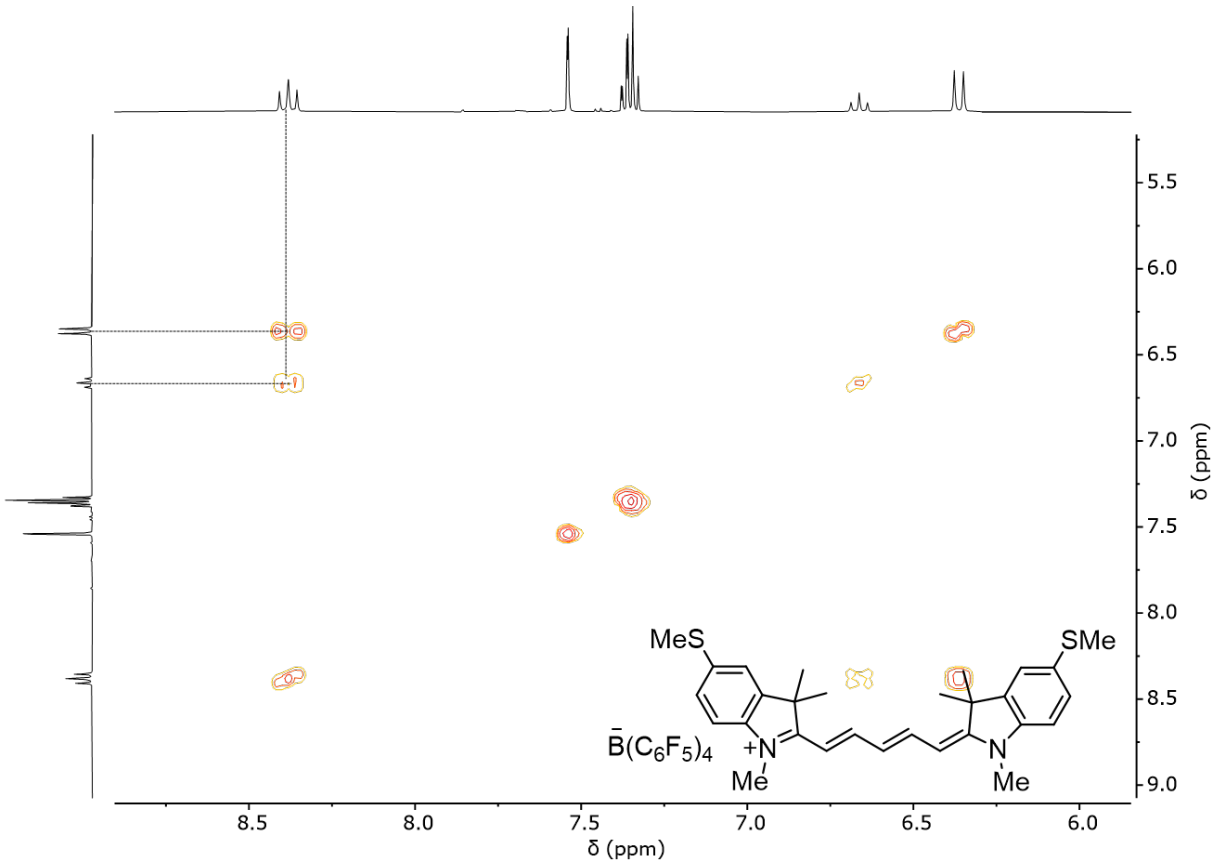

Figure S90. ^{1}H-^{1}H COSY NMR spectrum of **Cy5·B(C$_6$F$_5$)$_4$**, zoom (d_6-acetone, 500 MHz, 298 K).

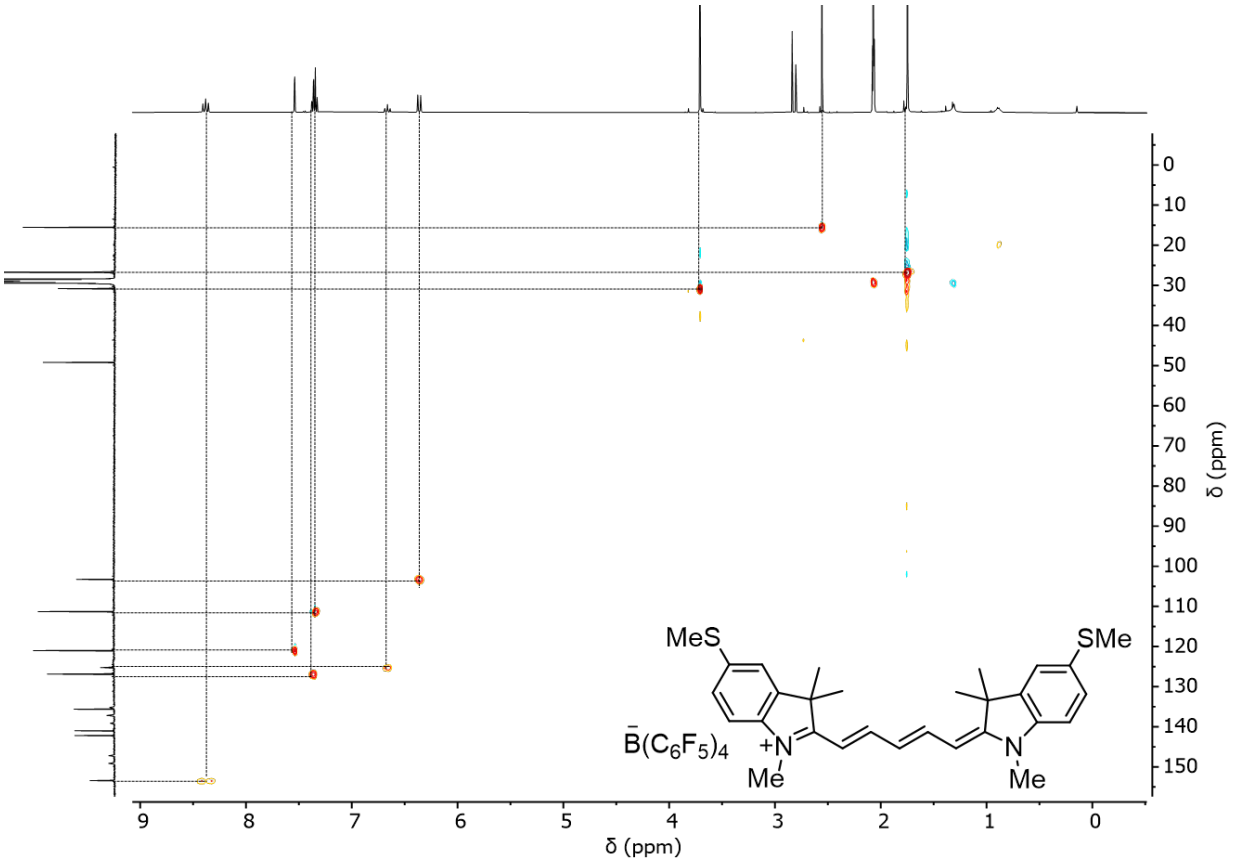

Figure S91. ^{13}C-^{1}H HSQC NMR spectrum of **Cy5·B(C$_6$F$_5$)$_4$** (d_6-acetone, 125 MHz, 298 K).

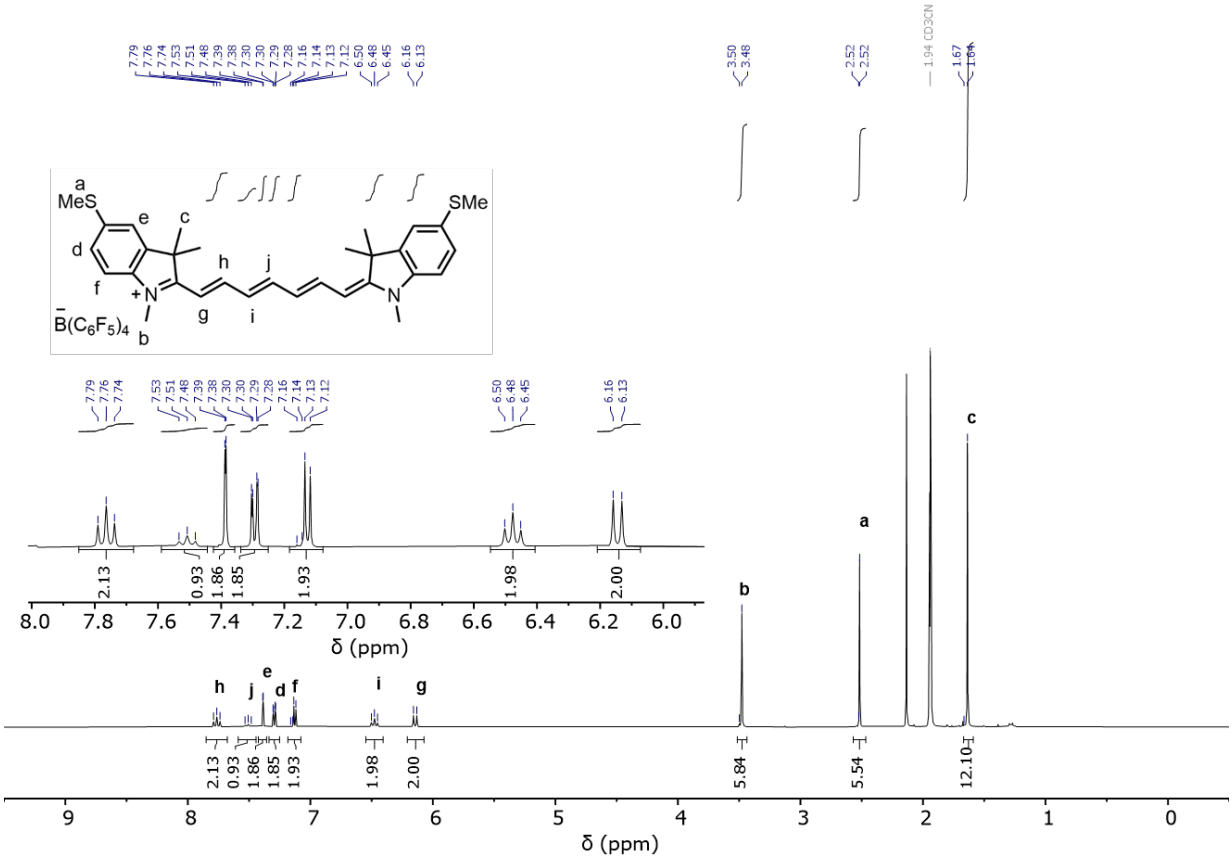

Figure S92. ^{1}H NMR spectrum of **Cy7·B(C$_6$F$_5$)$_4$** (d_3-CH_3CN, 400 MHz, 298 K).

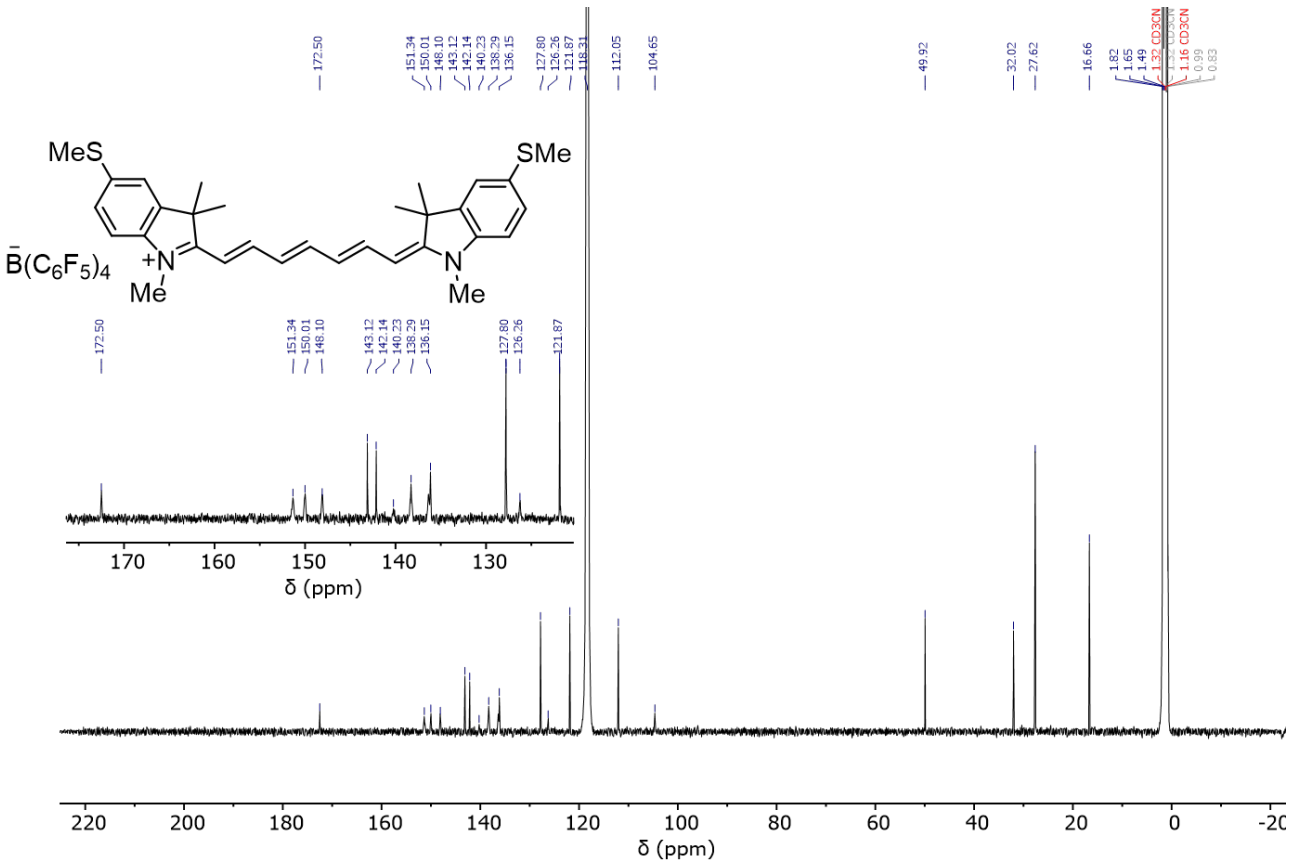

Figure S93. ^{13}C NMR spectrum of **Cy7·B(C$_6$F$_5$)$_4$** (d_3-CH$_3$CN, 125 MHz, 298 K).

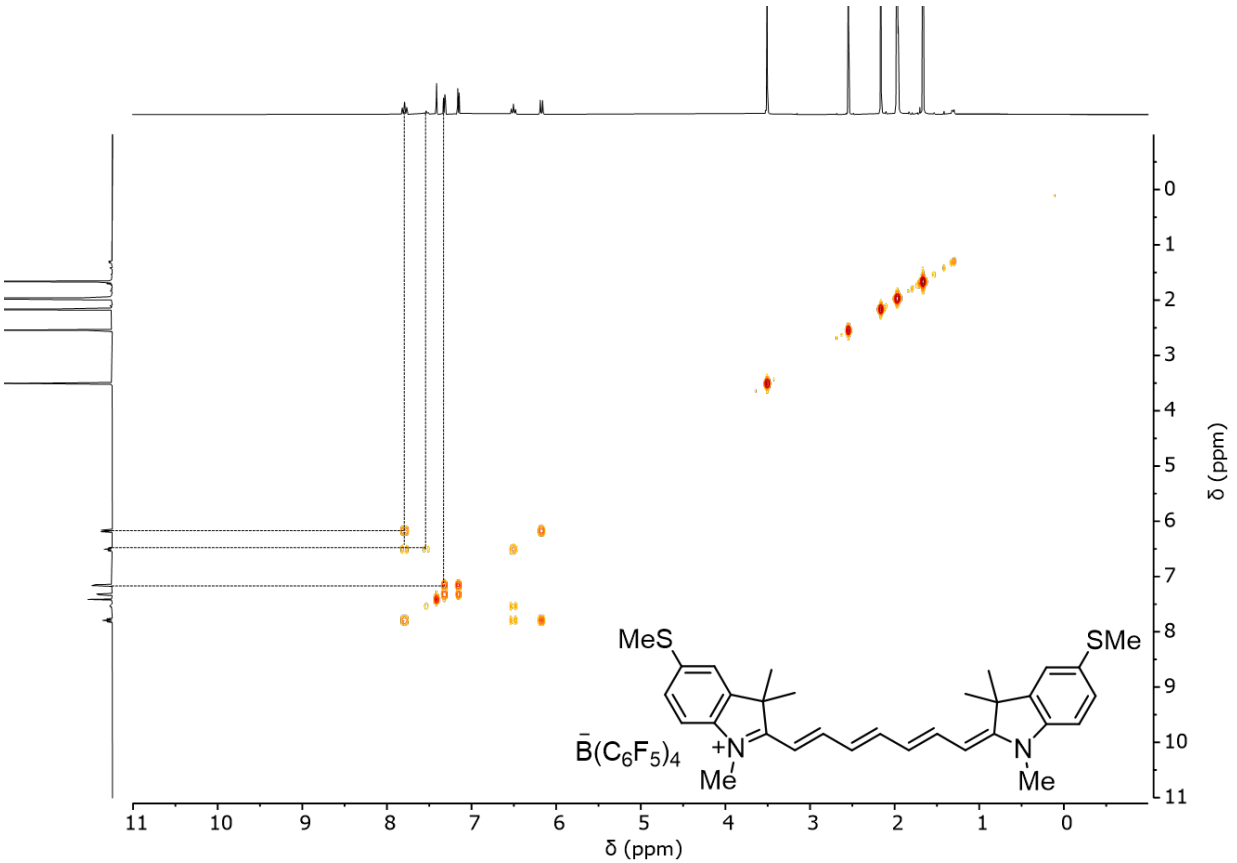

Figure S94. ^{1}H-^{1}H COSY NMR spectrum of **Cy7·B(C$_6$F$_5$)$_4$** (d_3-CH$_3$CN, 500 MHz, 298 K).

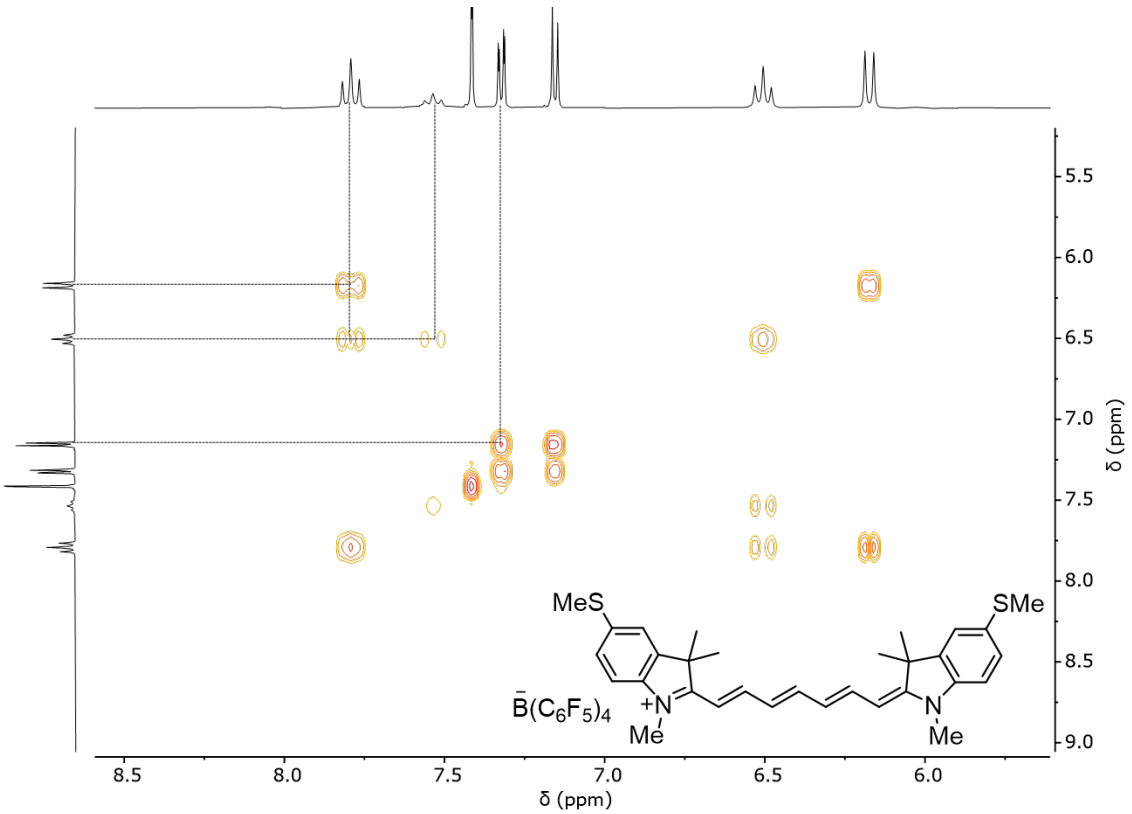

Figure S95. ^{1}H-^{1}H COSY NMR spectrum of **Cy7·B(C$_6$F$_5$)$_4$**, zoom (d_3-CH$_3$CN, 500 MHz, 298 K).

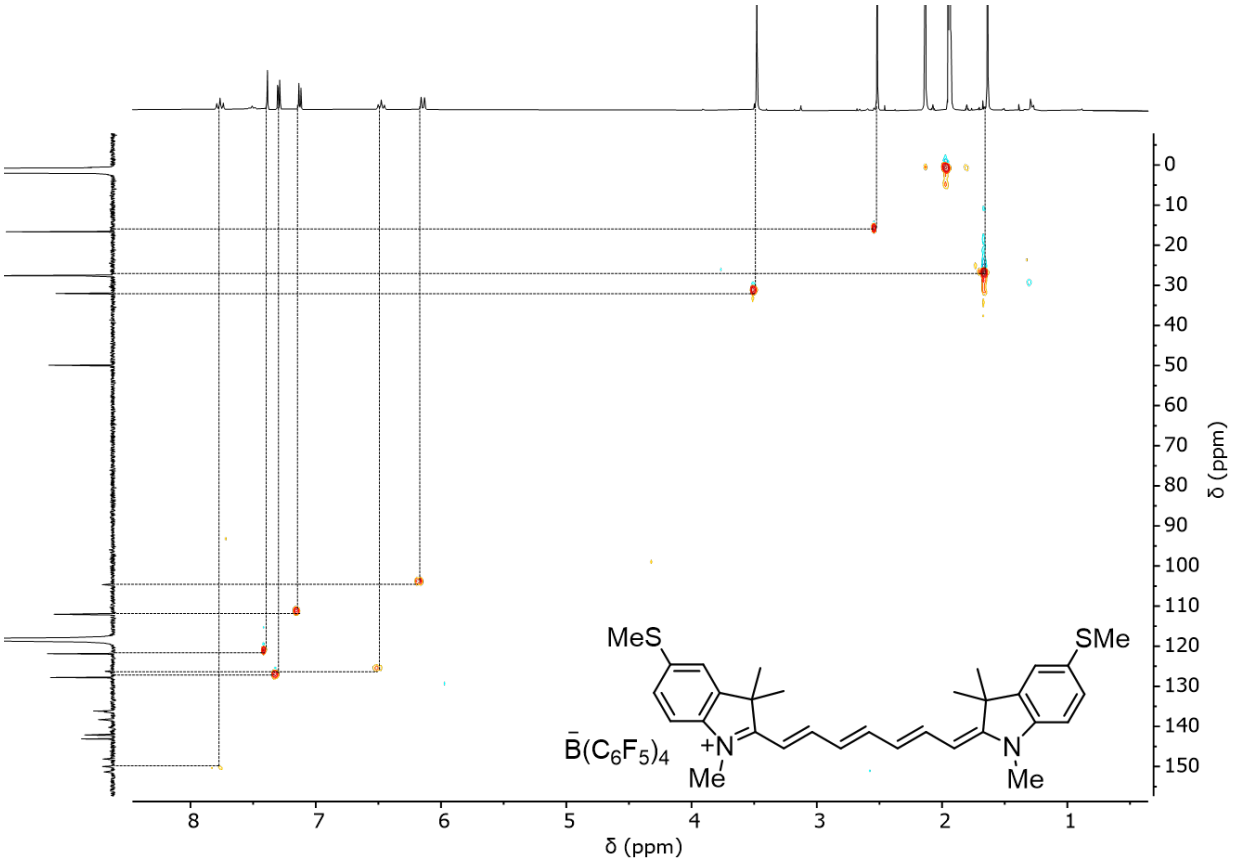

Figure S96. ^{13}C-^{1}H HSQC NMR spectrum of **Cy7·B(C$_6$F$_5$)$_4$** (d_3-CH$_3$CN, 125 MHz, 298 K).

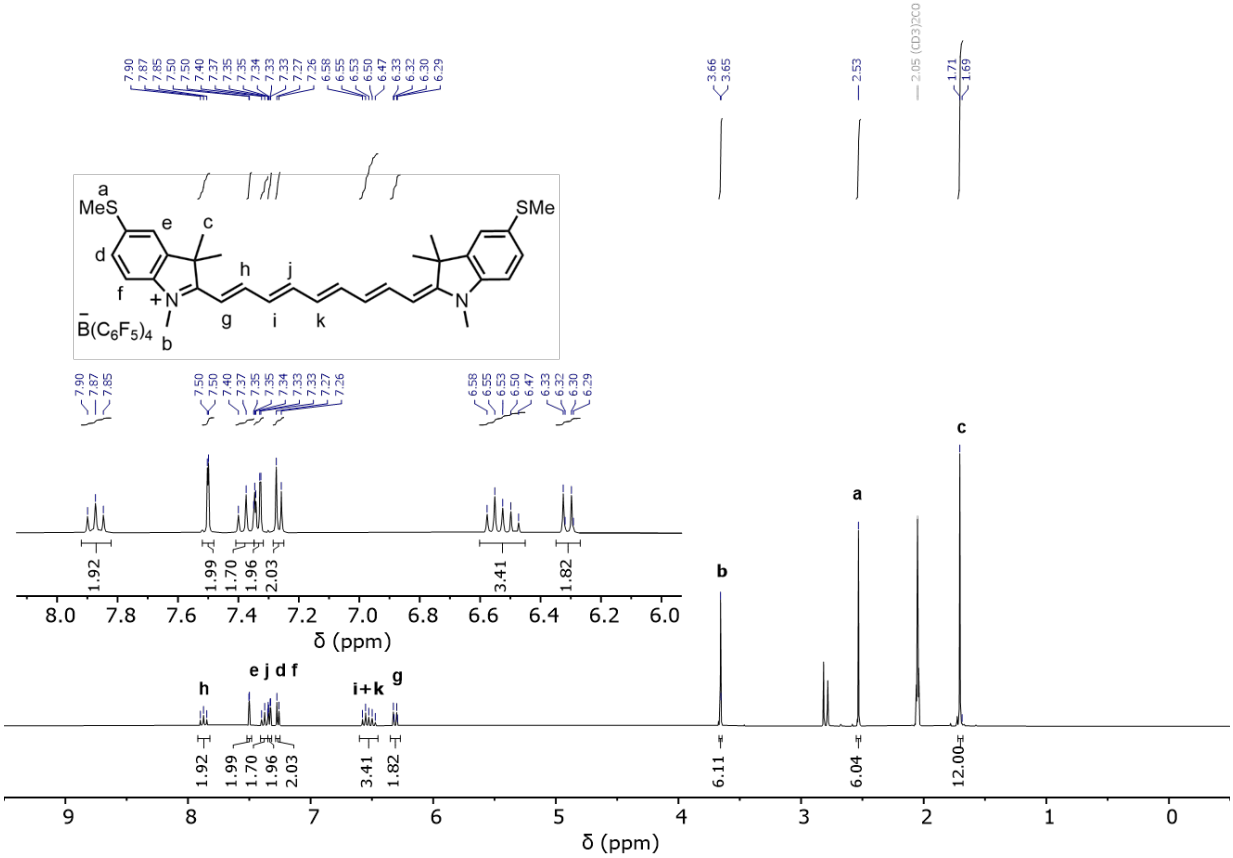

Figure S97. [1]H NMR spectrum of **Cy9·B(C$_6$F$_5$)$_4$** (d_6-acetone, 500 MHz, 298 K).

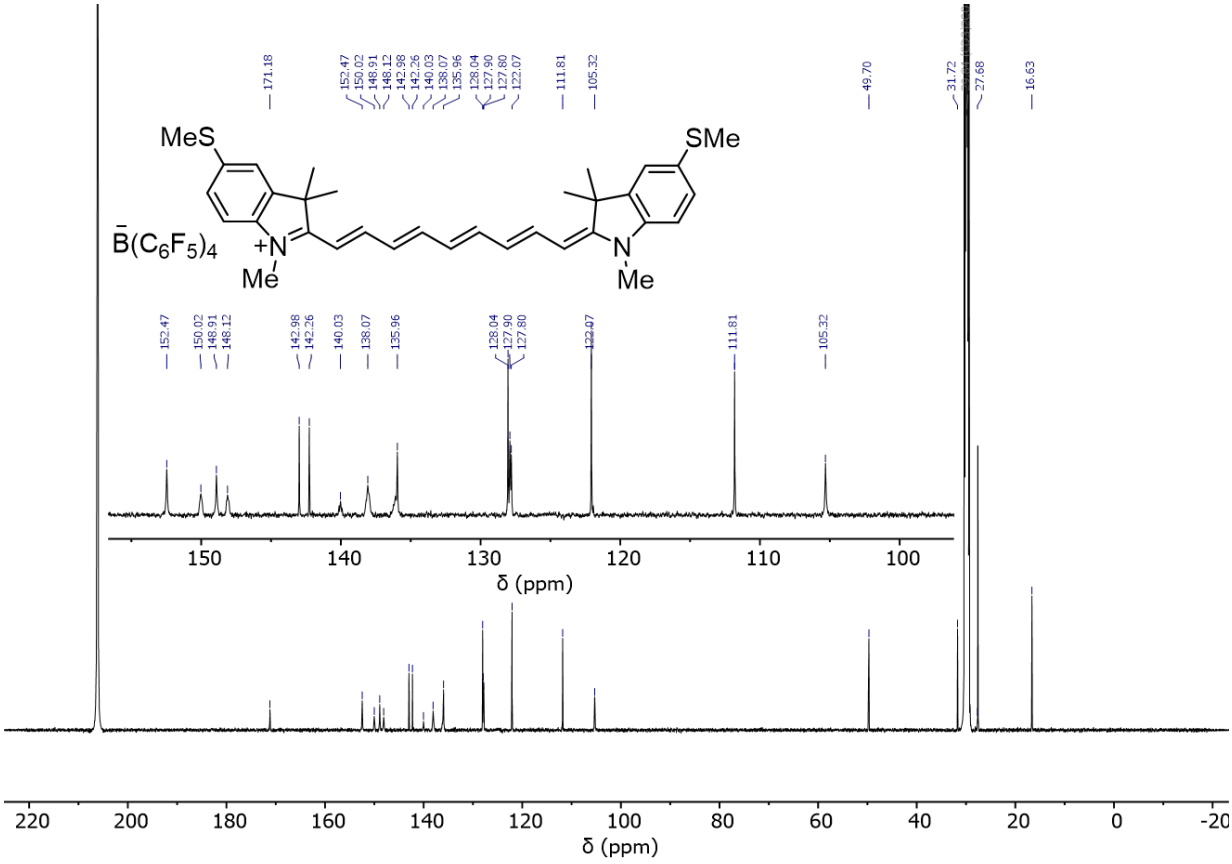

Figure S98. [13]C NMR spectrum of **Cy9·B(C$_6$F$_5$)$_4$** (d_6-acetone, 125 MHz, 298 K).

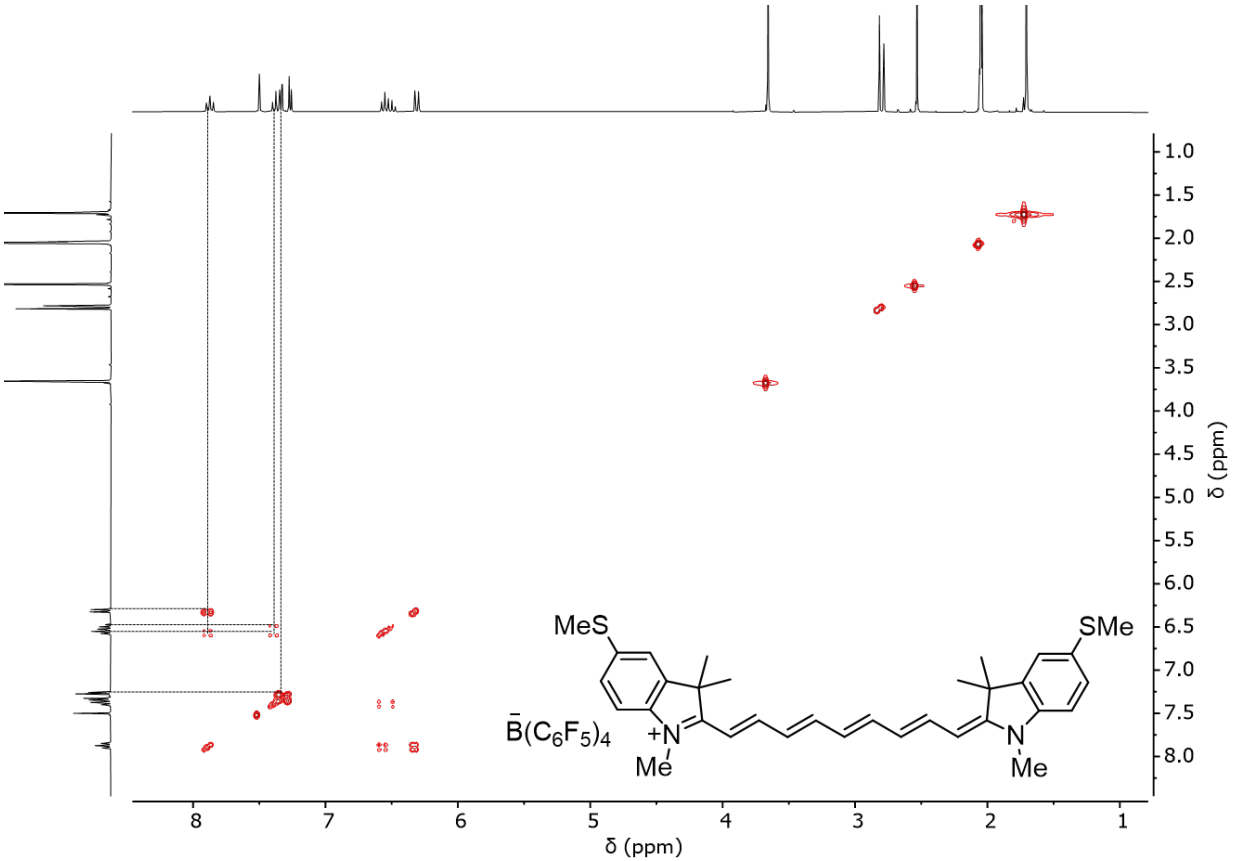

Figure S99. ^{1}H-^{1}H COSY NMR spectrum of **Cy9·B(C$_6$F$_5$)$_4$** (d_6-acetone, 500 MHz, 298 K).

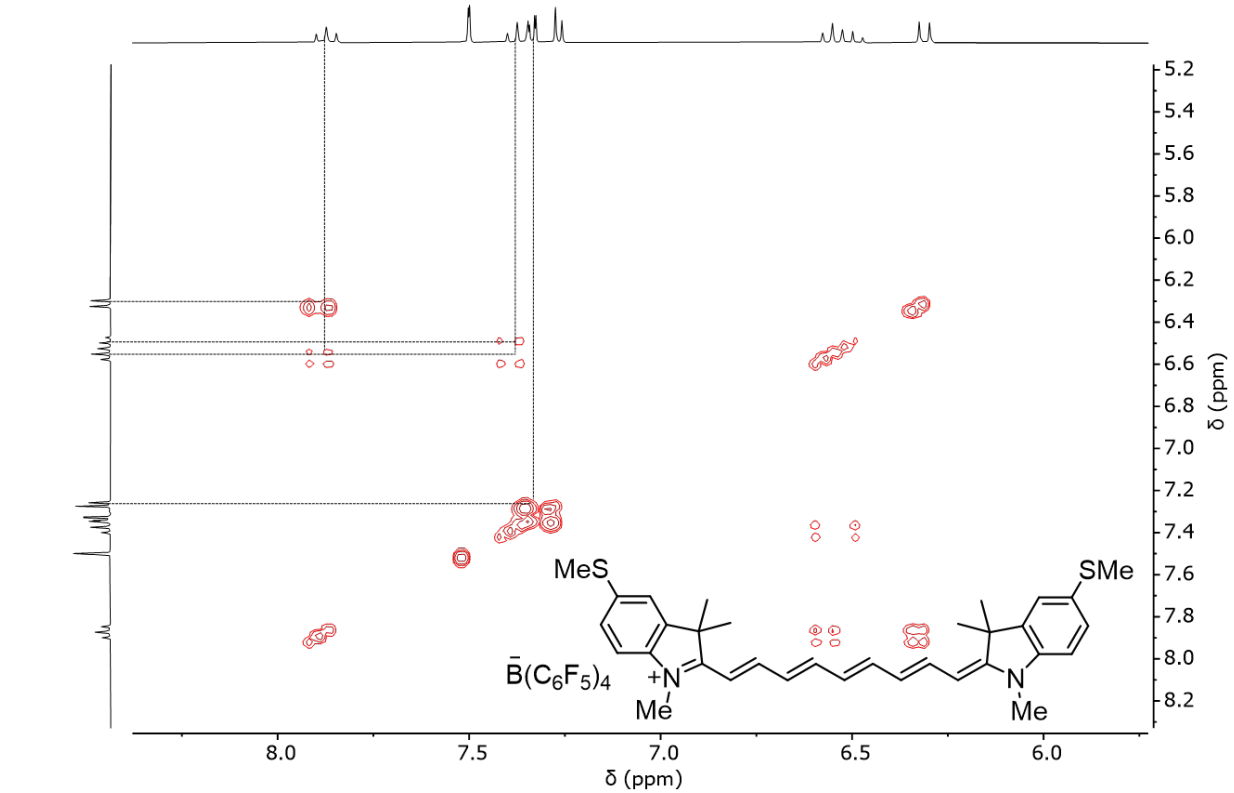

Figure S100. ^{1}H-^{1}H COSY NMR spectrum of **Cy9·B(C$_6$F$_5$)$_4$**, zoom (d_6-acetone, 500 MHz, 298 K).

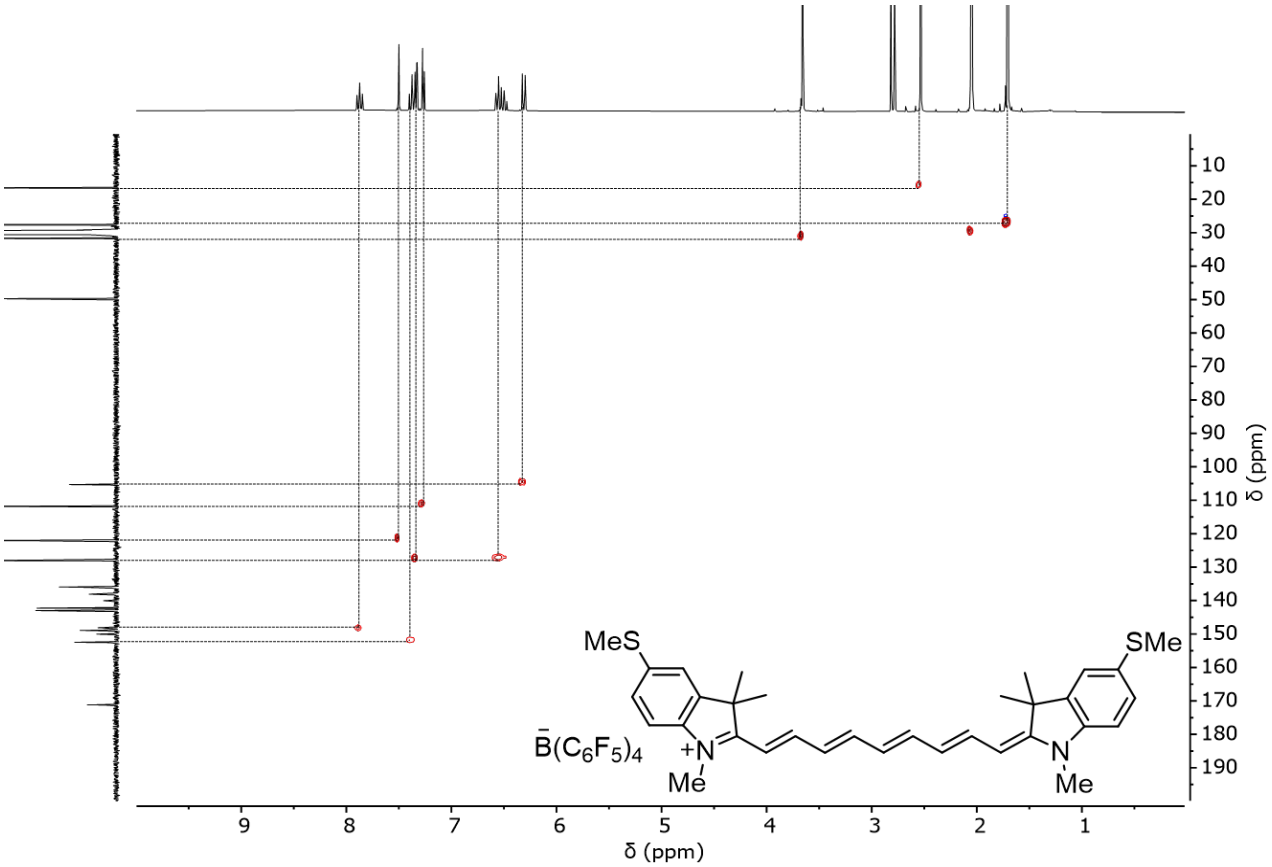

Figure S101. ^{13}C-^{1}H HSQC NMR spectrum of **Cy9·B(C$_6$F$_5$)$_4$** (d_6-acetone, 125 MHz, 298 K).

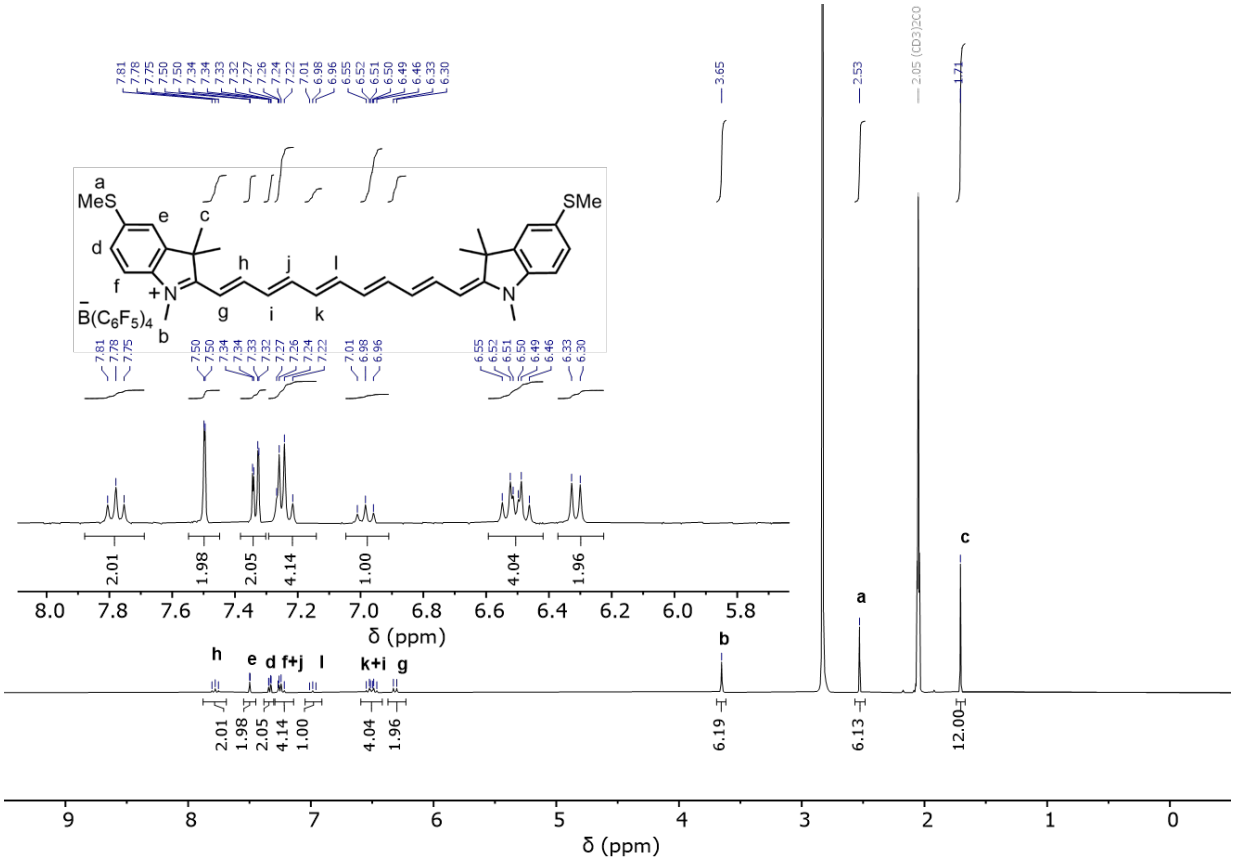

Figure S102. ^{1}H NMR spectrum of **Cy11·B(C$_6$F$_5$)$_4$** (d_6-acetone, 500 MHz, 298 K).

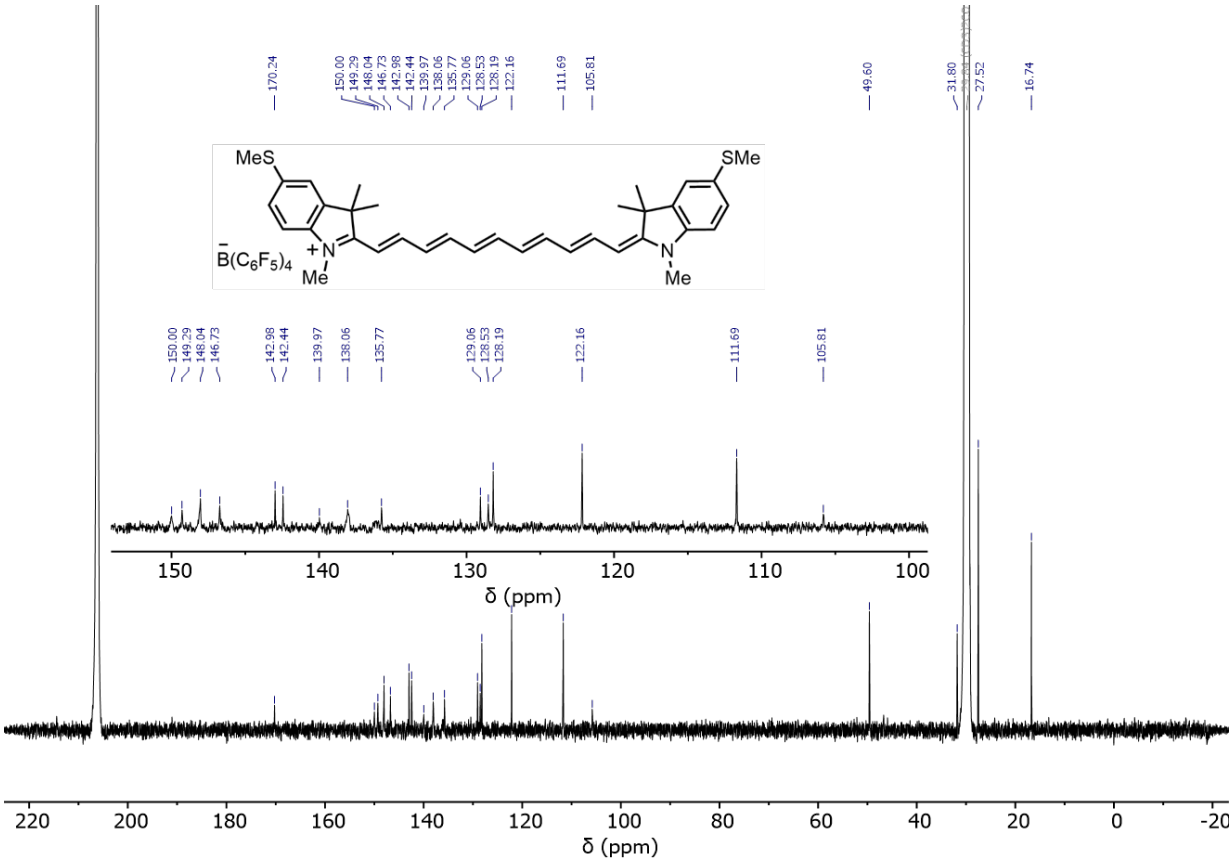

Figure S103. ^{13}C NMR spectrum of **Cy11·B(C$_6$F$_5$)$_4$** (d_6-acetone, 125 MHz, 298 K).

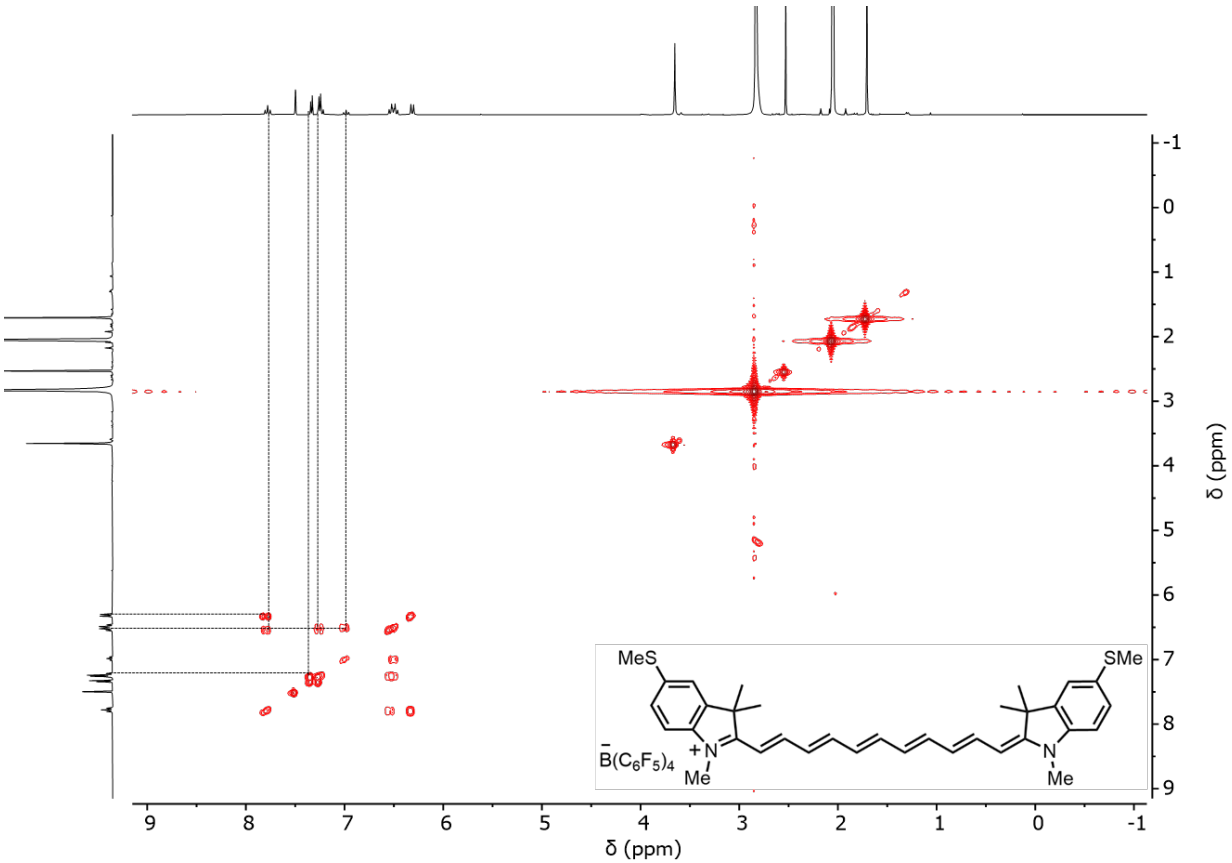

Figure S104. ^{1}H-^{1}H COSY NMR spectrum of **Cy11·B(C$_6$F$_5$)$_4$** (d_6-acetone, 500 MHz, 298 K).

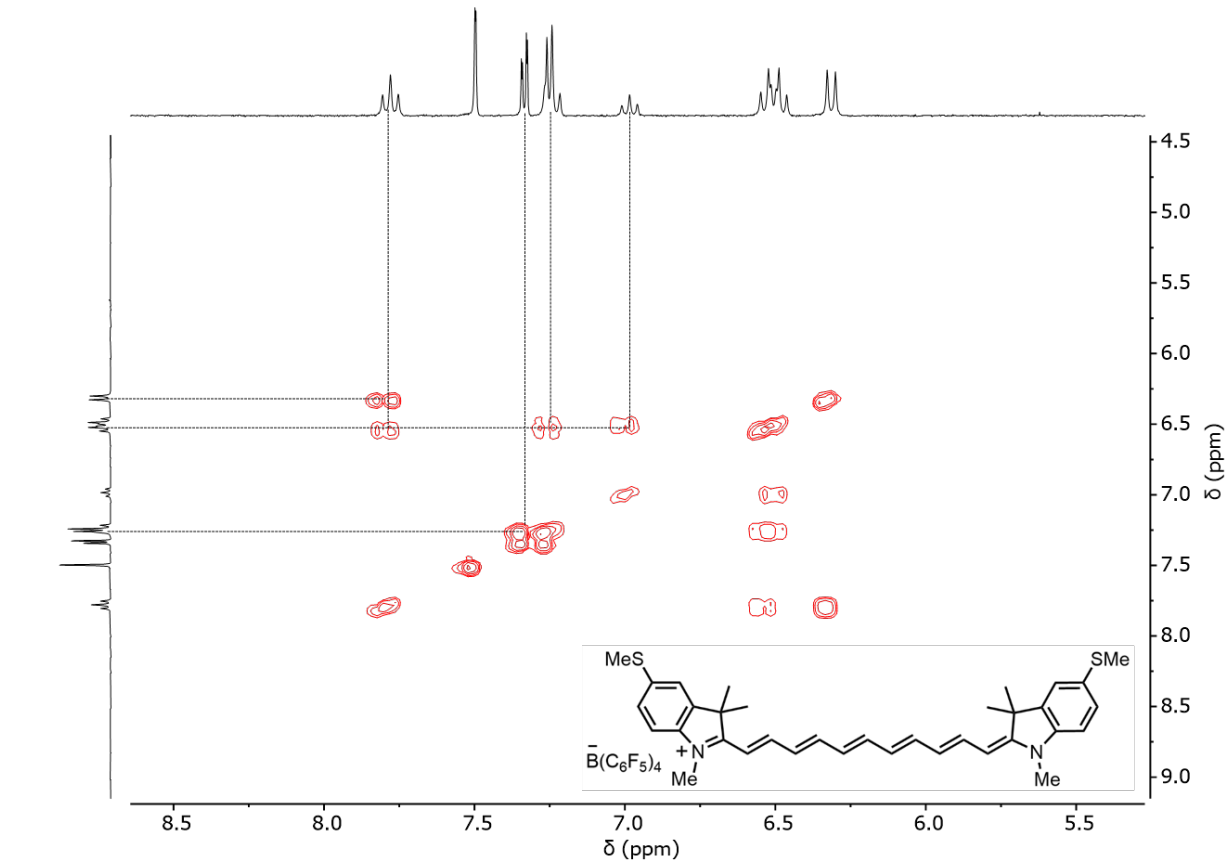

Figure S105. ^{1}H-^{1}H COSY NMR spectrum of **Cy11·B(C$_6$F$_5$)$_4$** with zoom-in (d_6-acetone, 500 MHz, 298 K).

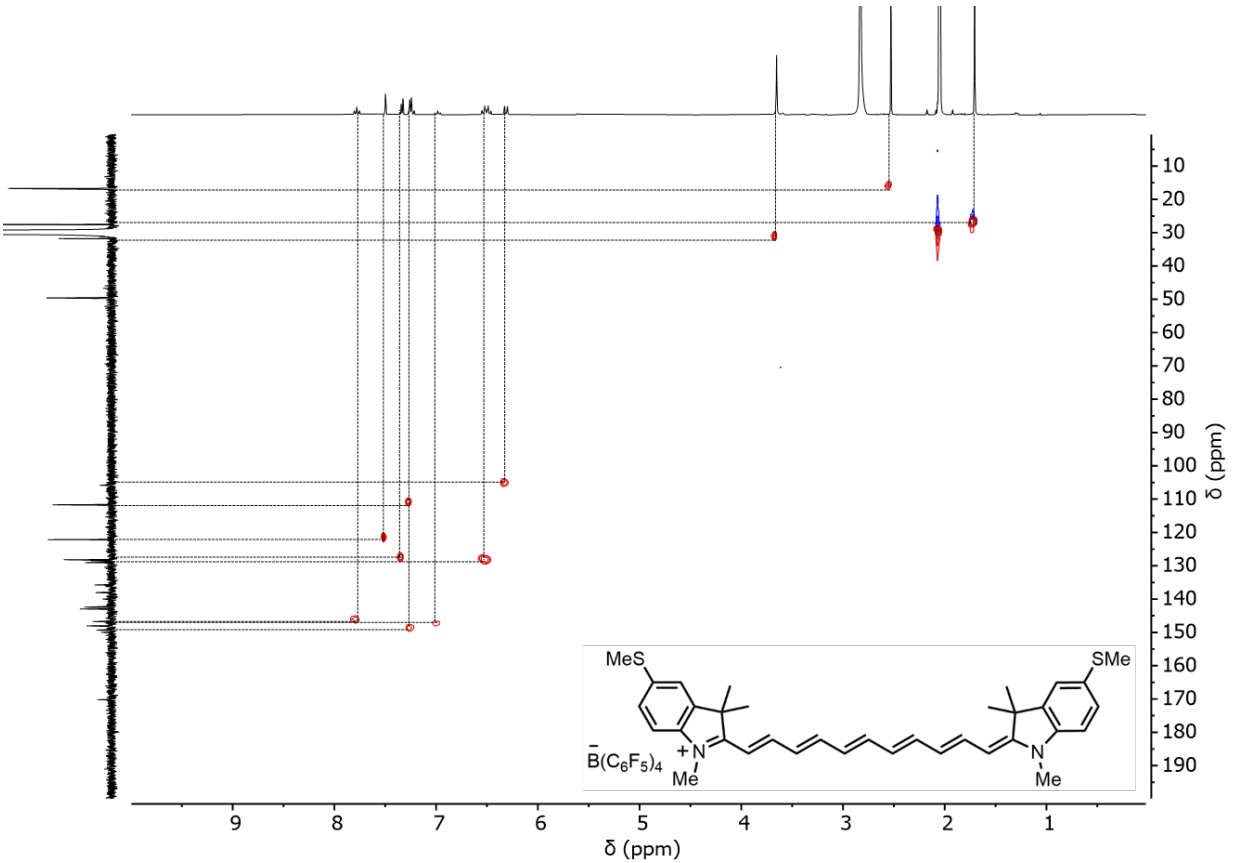

Figure S106. ^{13}C-^{1}H HSQC NMR spectrum of **Cy11·B(C$_6$F$_5$)$_4$** (d_6-acetone, 125 MHz, 298 K).

Section 7. References

1. Ley, S. V.; Smith, S. C.; Woodward, P. R. Further reactions of *t*-butyl 3-oxobutanthioate and *t*-butyl 4-diethyl-phosphono-3-oxobutanthioate: Carbonyl coupling reactions, amination, use in the preparation of 3-acyltetramic acids and application to the total synthesis of fuligorubin A. *Tetrahedron* **1992**, *48*, 1145–1174.
2. Ahlström, M. M.; Ridderström, M.; Zamora, I.; Luthman, K. CYP2C9 Structure-metabolism relationships: Optimizing the metabolic stability of COX-2 inhibitors. *J. Med. Chem.* **2007**, *50*, 4444–4452.
3. Fung, E.-D.; Gelbwaser, D.; Taylor, J.,; Low, J.; Xia, J., Davydenko, I.; Campos, L. M.; Marder, S.; Peskin, U.; Venkataraman, L. Breaking down resonance: nonlinear transport and the breakdown of coherent tunneling models in single molecule junctions. *Nano Lett.* **2019**, *19*, 2555−2561.
4. Gunasekaran, S.; Hernangoḿez-Peŕez, D.; Davydenko, I.; Marder, S.; Evers, F.; Venkataraman, L. Near length-independent conductance in polymethine molecular wires. *Nano Lett.* **2018**, *18*, 6387−6391.
5. Makin, S. M.; Monich, N. V.; Shavrygina, O. A.; Berezhnaya, M. I.; Kheifets, S. A. A novel method of the synthesis of higher polymethinium salts. *Tetrahedron* **1969**, *25*, 4939–4948.
6. Rurack, K.; Spieles, M. Fluorescence quantum yields of a series of red and near-infrared dyes emitting at 600−1000 nm. *Anal. Chem.* **2011**, *83*, 1232–1242.
7. Casalboni, M.; De Matteis, F.; Prosposito, P.; Quatela, A.; Sarcinelli, F. Fluorescence efficiency of four infrared polymethine dyes. *Chem. Phys. Lett.* **2003**, *373*, 372–378.
8. Allan, D. R.; Nowell, H.; Barnett, S. A.; Warren, M. R.; Wilcox, A.; Christensen, J.; Saunders, L. K.; Peach, A.; Hooper, M. T.; Zaja, L.; Patel, S.; Cahill, L.; Marshall, R.; Trimnell, S.; Foster, A. J.; Bates, T.; Lay, S.; Williams, M. A.; Hathaway, P.V.; Winter, G.; Gerstel, M.; Wooley R. W. A novel dual air-bearing fixed-χ diffractometer for small-molecule single-crystal X-ray diffraction on beamline I19 at Diamond Light Source. *Crystals* **2017**, *7*, 336.
9. Reck, G.; Dähne, L. CCDC 619814: *Experimental Crystal Structure Determination*, **2006**, DOI: 10.5517/ccnsz0d
10. Reck, G.; Dähne, L. CCDC 619809: *Experimental Crystal Structure Determination*, **2006**, DOI: 10.5517/ccnsyv6
11. Dähne, L.; Reck, G. One-dimensional J-aggregates in crystals of l,7-bis-(dimethylamino)-heptamethinium perchlorate. *Z. Krist. – Cryst. Mater.* **1995**, *210*, 40–43.
12. Potenza, J. A.; Zyontz, L.; Borowski, W. Crystal and molecular structure of 3,3'-diethylthiatricarbocyanine iodide, an infrared photographic sensitizing dye. *Acta Cryst.* **1978**, *B34*, 193–199.
13. Starkholm, A.; Kloo, L.; Svensson, P. H. Implicit tandem organic−inorganic hybrid perovskite solar cells based on internal dye sensitization: Robotized screening, synthesis, device implementation, and theoretical insights. *J. Am. Chem. Soc.* **2020**, *142*, 18437–18448.
14. Yau, C. M. S.; Pascu, S. I.; Odom, S. A.; Warren, J. E.; Klotz, E. J. F.; Frampton, M. J.; Williams, C. C.; Coropceanu, V.; Kuimova, M. K.; Phillips, D.; Barlow, S.; Brédas, J.-L; Marder, S. R.; Millar, V.; Anderson, H. L. Stabilisation of a heptamethine cyanine dye by rotaxane encapsulation. *Chem. Commun.* **2008**, 2897–2899.

15. Guieu, V.; Payrastre, C.; Madaule, Y.; Garcia-Alonso, S.; Lacroix, P. G.; Nakatani, K. Large quadratic nonlinear optical efficiencies in pseudosymmetric streptocyanine dyes. *Chem. Mater.* **2006**, *18*, 3674–3681.
16. Izquierdo, A.; Guieu, V.; Gornitzka, H.; Madaule, Y.; Payrastre, C. Synthesis and reactivity of a new nonacarbon chain carboxonium salt − access to a new class of streptocyanine dyes. *Eur. J. Org. Chem.* **2004**, 2317–2320.
17. Bouit, P.-A.; Aronica, C.; Guy, L.; Martinez, A.; Andraud, C.; Maury, O. Diastereoselective supramolecular ion-pairing between the TRISPHAT anion and *pro*-chiral heptamethine cyanine dyes. *Org. Biomol. Chem.* **2009**, *7*, 3086–3090.
18. Bouit, P.-A.; Aronica, C.; Toupet, L.; Le Guennic, B.; Andraud, C.; Maury, O. Continuous symmetry breaking induced by ion pairing effect in heptamethine cyanine dyes: Beyond the cyanine limit. *J. Am. Chem. Soc.* **2010**, *132*, 4328–433.
19. Véron, A. C.; Zhang, H.; Linden, A.; Nüesch, F.; Heier, J.; Hany, R.; Geiger, T. NIR-absorbing heptamethine dyes with tailor-made counterions for application in light to energy conversion. *Org. Lett.* **2014**, *16*, 1044–1047.
20. Eskandari, M.; Roldao, J. C.; Cerezo, J.; Milián-Medina, B.; Gierschner, J. Counterion-mediated crossing of the cyanine limit in crystals and fluid solution: Bond length alternation and spectral broadening unveiled by quantum chemistry. *J. Am. Chem. Soc.* **2020**, *142*, 2835–2843.
21. Champagne, B.; Guillaume, M.; Zutterman, F. TDDFT investigation of the optical properties of cyanine dyes. *Chem. Phys. Lett.* **2006**, *425*, 105−109.
22. Guennic B. L.; Jacquemin, D. Taking up the cyanine challenge with quantum tools. *Acc. Chem. Res.* **2015**, *48*, 530–537.
23. Soler, J. M.; Artacho, E.; Gale, J. D.; García, A.; Junquera, J.; Ordejón, P.; Sánchez-Portal, D. The SIESTA method for *ab initio* order-*N* materials simulation. *J. Phys.: Condens. Matter.* **2002**, *14*, 2745–2779.
24. Ferrer, J.; Lambert, C. J.; García-Suárez, V. M.; Manrique, D. Z.; Visontai, D.; Oroszlany, L.; Rodríguez-Ferradás, R.; Grace, I.; Bailey, S. W. D.; Gillemot, K.; Sadeghi, H.; Algharagholy, L. A. GOLLUM: a next-generation simulation tool for electron, thermal and spin transport. *New J. Phys.* **2014**, *16*, 093029.
25. Garner, M. H.; Bro-Jørgensen, W.; Pedersen, P. D.; Solomon, G. C. Reverse bond-length alternation in cumulenes: Candidates for increasing electronic transmission with length. *J. Phys. Chem. C* **2018**, *122*, 26777–26789.
26. Tsuji, Y.; Movassagh, R.; Datta, S.; Hoffmann, R. Exponential attenuation of through-bond transmission in a polyene: Theory and potential realizations. *ACS Nano* **2015**, *9*, 11109–11120.
27. See equation (10.71) from *"Quantum Transport in Nanostructures and Molecules"*, Lambert, C. J., IOP Publishing (2021), page 10–17.
28. Zotti, L. A.; Bednarz, B.; Hurtado-Gallego, J.; Cabosart, D.; Rubio-Bollinger, G.; Agrait, N.; van der Zant, H. S. J. Can one define the conductance of amino acids? *Biomolecules* **2019**, *9*, 580.
29. Rincón-García, L.; K. Ismael, A.; Evangeli, C.; Grace, I.; Rubio-Bollinger, G.; Porfyrakis, K., Agraït, N.; Lambert, C. J. Molecular design and control of fullerene-based bi-thermoelectric materials. *Nature Mater*. **2016**, *15*, 289–293.